Badanie stosunku produkcji protonów do pionów w zależności od pędu poprzecznego w zderzeniach jądro-jądro przy energii $\sqrt{s_{NN}} = 62.4$ GeV oraz 200 GeV w eksperymencie BRAHMS

Natalia Katryńska

Praca doktorska

pod kierunkiem

Prof. dr. hab. Zbigniewa Majki

oraz

Dr. Pawła Staszla

Wydział Fizyki, Astronomii i Informatyki Stosowanej

Uniwersytetu Jagiellońskiego

grudzień 2009

The BRAHMS results on the proton-to-pion ratio p_T-dependence in nucleus-nucleus collisions at $\sqrt{s_{NN}} = 62.4$ GeV and 200 GeV

Dissertation

by

Natalia Katryńska

Supervisors:

Prof. Zbigniew Majka

and

Ph. D. Paweł Staszel

Faculty of Physics, Astronomy and Applied Computer Science

Jagiellonian University

December 2009

Abstract

High performance of measurements at RHIC by four experiments: BRAHMS, PHENIX, PHOBOS and STAR allows to provide comprehensive research, the deepest insight on mesons and baryons production in heavy ions reactions at ultra-relativistic energies among others. This thesis presents proton-to-pion ratio measurements in Au+Au and p+p interactions at $\sqrt{s_{NN}} = 62.4$ GeV and 200 GeV as a function of transverse momentum and collision centrality within the pseudorapidity range $0 \leq \eta \leq 3.65$. The data were measured over a broad rapidity and p_T coverage by BRAHMS Collaboration using two unique spectrometers. For the indicated heavy ion collisions the baryo-chemical potential, μ_B, spans from $\mu_B \approx 25$ MeV ($\sqrt{s_{NN}} = 200$ GeV, $\eta = 0$) to $\mu_B \approx 260$ MeV ($\sqrt{s_{NN}} = 62.4$ GeV, $\eta \approx 3$). The top value of $p/\pi^+(p_T)$ ratio for Au+Au collisions at $\sqrt{s_{NN}} = 200$ GeV does not go beyond 3 at intermediate transverse momentum at $\eta \approx 3$. The p/π^+ ratio increases with centrality in the covered p_T range. The ratio of $\bar{p}/\pi^-$ reaches the maximum of 0.5 at $\eta \approx 2.3$ for Au+Au system at the top RHIC energy and decreases for more forward pseudorapidities. For Au+Au reactions at $\sqrt{s_{NN}} = 62.4$ GeV p/π^+ ratio reaches large value of 8-10 at $p_T = 1.5$ GeV/c. Weak centrality dependence of p/π^+ ratio in heavy ions reactions for $\eta > 2.5$ at lower colliding energy is observed. Moreover, a striking agreement between $p/\pi^+(p_T)$ ratio measured for Au+Au collisions at $\sqrt{s_{NN}} = 200$ GeV ($\eta \approx 2.2$) and at $\sqrt{s_{NN}} = 62.4$ GeV ($\eta \approx 0$) is noted, where the properties of the bulk medium can be described with the common value of $\mu_B = 62$ MeV. The description of hadronization of the strongly interacting matter formed in heavy ion collision at ultra-relativistic energies by parton coalescence and expanding fireball with collective flow is presented and compared with measured p/π^+ and $\bar{p}/\pi^-$ ratios at different beam energies and rapidities. The coalescence model utilizes the dynamics of transforming partons into hadronic bound states in the presence of partonic medium. The non-boost-invariant single-freezeout approach captures the basic features of hadron abundances imposed on the Hubble-type flow expansion.

Acknowledgements

I would like to express my gratitude to all those who gave me the possibility to complete this thesis.

I express my deep sense of gratitude to **Prof. Zbigniew Majka** and **Dr. Paweł Staszel**, for their invaluable help and guidance during the course of the project.

I am grateful to Prof. Zbigniew Majka for having given me the support and confidence. He is a person, who gave and confirmed this permission and encouraged me to go ahead with my thesis.

I am highly indebted to Paweł Staszel for constantly encouraging me by giving his critics on my work. His help, stimulating suggestions and encouragement helped me in all the time of research for and writing of this thesis. I am deeply thankful for his heartiness and understanding.

This thesis would not be possible without the essential and gracious support of BRAHMS Collaborators and BRAHMS Collaboration spokesperson Flemming Videbæk. My sincere thanks for their generous and varied contributions to this work.

I would like to express my thanks to all participants of Division of Hot Matter Physics at Jagiellonian University. I appreciate their willingness and warmth.

I would like to thank Aleksandra Guńkiewicz for a patience and capacity to correct my "mistakes" during all my studies.

W szczególności chciałabym podziękować...

...Agnieszce - za Jej ciepło, oddanie oraz zrozumienie.

...Bartkowi - za pokazanie mi nowej drogi i wiarę w zmienianie najtrudniejszego.

Dziękuję Wam, że zawsze jesteście blisko.

Dziękuję Rodzinie za wszelką pomoc w przeciągu tych lat.

Contents

List of Figures

Chapter 1

Introduction

1.1 New era of relativistic heavy ion collision physics

In 2000, the Relativistic Heavy Ion Collider (RHIC), located in Brookhaven National Laboratory, started delivering beams of protons and ions to the four experiments: BRAHMS, PHENIX, PHOBOS and STAR. The main goal of the research was to deliver evidences for creation of new state of matter, called Quark Gluon Plasma (QGP) [1, 2] in heavy ion collisions at ultra-relativistic energies. During recent nine years at RHIC, p+p, p$^{\uparrow}$+p, d+Au, Cu+Cu and Au+Au interactions were investigate at $\sqrt{s_{NN}}$ = 22, 62.4, 130 and 200 GeV and a lot of new issues have been brought up [3, 4, 5, 6]. The unique BRAHMS experimental setup allows to measure produced hadrons in the wide range of rapidity what gives the possibility to investigate properties of created matter versus the longitudinal direction.

Although discovery of QGP at RHIC might be questioned, new equilibrated partonic state of matter with typical perfect fluid properties has undoubtedly been found [7]. The data of elliptic flow [8] and $p/\pi^{+}(p_T)$ ratio around midrapidity [9] have shown that the final hadronic state remembers the partonic fluid features. This is reflected in constituent quark scaling of elliptic flow coefficient, v_2, and an enhancement of baryon-to-meson ratios that scales with the size of the created systems.

The elliptic flow coefficient is defined by Fourier coefficient as follows:

$$\nu_n \equiv \langle \exp\left(in\left(\phi - \Phi_R\right)\right)\rangle = \langle \cos\left(n\left(\phi - \Phi_R\right)\right)\rangle \tag{1.1}$$

where:
ϕ - azimuthal angle of an emitted particle, Φ_R - azimuth of the reaction plane [10].

The results of the elliptic flow ν_2 measurements [8] strongly suggest that at RHIC in nucleus-nucleus collisions at top energy the new state of strongly interacting matter is observed. These observations correspond with the perfect fluid hydrodynamical model calculations [11, 12]. The PHENIX [8], PHOBOS [14], STAR [13] data show that the elliptic flow coefficient ν_2 scales almost perfectly with eccentrity (see the definition in [11]), system size and transverse energy.

The evidences of new state of matter are:

1. The elliptic flow coefficient scales with the number of valence quarks for mesons and baryons $(\pi, \mathrm{K}, \mathrm{p}, \mathrm{d}, \phi, \Lambda, \Xi, \Omega)$.

2. The scaling of the flow of particles which contain heavy quarks - especially D meson with charm quark as the component.

3. Studies of the pre-hadronic phase on the basis of the elliptic flow measurements.

4. The observed jet quenching as the evidence of parton energy loss (*inter alia* hadron formation time, momentum dependence of hadron suppression, centrality dependence of hadron suppression, jet-like hadron correlation, high p_T azimuthal anisotropy, data at lower colliding energy) [15].

The observations of elliptic flow behaviour are also supported by the BRAHMS results [16] which data span to the value of pseudorapidity $\eta = 3.4$. The theoretical hydrodynamical description [12] together with forward elliptic flow results suggest that the expansion of the produced medium along longitudinal direction is even greater than previously has been thought [17]. The constituent quark scaling is observed.

At RHIC the significant jet quenching is exposed for central nucleus-nucleus collisions. The results of suppression high-p_T single inclusive hadron spectra and suppression of back-side jet-like correlations tell about the finale state interactions with the medium. As highlighted in [15] these measurements strongly indicate that it is an effect of partons loosing their energy in the dense, colour medium and definitely is not related to hadron absorption.

The experimental data of proton-to-pion ratio vs. transverse momentum in the wide range of pseudorapidity for heavy ion system constitute a testing ground of capturing the properties of bulk medium. Unquestionably, the features of particle production are driven with the value of baryo chemical potential, μ_B. The studies of η dependence of $p/\pi(p_T)$ deliver information how hadronization process goes through in the wide range of μ_B. With these results we want to find out which recombination or hydrodynamic scenario is followed in the final state of strongly interacting matter.

1.2 Basic issues studied using the BRAHMS Experiment's setup

1.2.1 Net-baryon density distribution

Wide rapidity acceptance of the BRAHMS spectrometers provides unique opportunity to study nuclear stopping in the ultra-relativistic nucleus-nucleus reactions. The average rapidity loss, $<\delta y> = y_b$ - $<y>$, quantifies stopping in heavy ions collisions:

$$< \delta y >= y_b - \frac{2}{N_{part}} \int_0^{y_b} y \frac{dN_{B-\bar{B}}}{dy} dy \tag{1.2}$$

where:

y_b - rapidity of incoming beam ($y_{beam} = 4.2$ for Au+Au at $\sqrt{s_{NN}} = 62.4$ GeV, $y_{beam} = 5.4$ for Au+Au at $\sqrt{s_{NN}} = 200$ GeV), N_{part} - number of nucleons participating in the collisions, $\frac{dN_{B-\bar{B}}}{dy}$ - net-baryon rapidity density. If initial baryon participants lose all the kinetic energy ($<\delta y> = y_b$) we observe full stopping, for $<\delta y> = 0$ the system is completely transparent. Before RHIC era, at Schwerionen Synchrotron (SIS18) in Darmstadt, Alternating Gradient Synchrotron (AGS) in Brookhaven National Laboratory and Super Proton Synchrotron (SPS) in CERN, it was noticed that $<\delta y>$ is linearly proportional to the beam rapidity. The BRAHMS results [19] show that this linear scaling is broken above top SPS energies - Fig. 1.1. Assuming that underlying physics is the same at highest attainable energies, the extrapolation of $<\delta y>$ to the beam rapidity for Large Hadron Collider ($y_b \approx 8.7$) is depicted as the solid black line in Fig. 1.1.

While the nuclei are colliding, the nucleons lose their kinetic energy. The energy loss per participant baryon can be expressed:

$$< \delta E >= E_b - \frac{2}{N_{part}} \int_0^{y_b} \langle m_T \rangle \cosh y \frac{dN_{B-\bar{B}}}{dy} dy \tag{1.3}$$

where:

E_b - initial energy of beam.

It is estimated that $< \delta E > = 21 \pm 2$ GeV for Au+Au at $\sqrt{s_{NN}} = 62.4$ GeV [19] and $<\delta E> = 73 \pm 6$ GeV for Au+Au at $\sqrt{s_{NN}} = 200$ GeV for the most (0-10 %) central collisions [20]. For two colliding nucleons the calculated energy loss is $2<\delta E>$, which is 70% of the initial energy of beam. This energy loss is transformed mainly into particle production and random (thermal) motion of produced partons and particles.

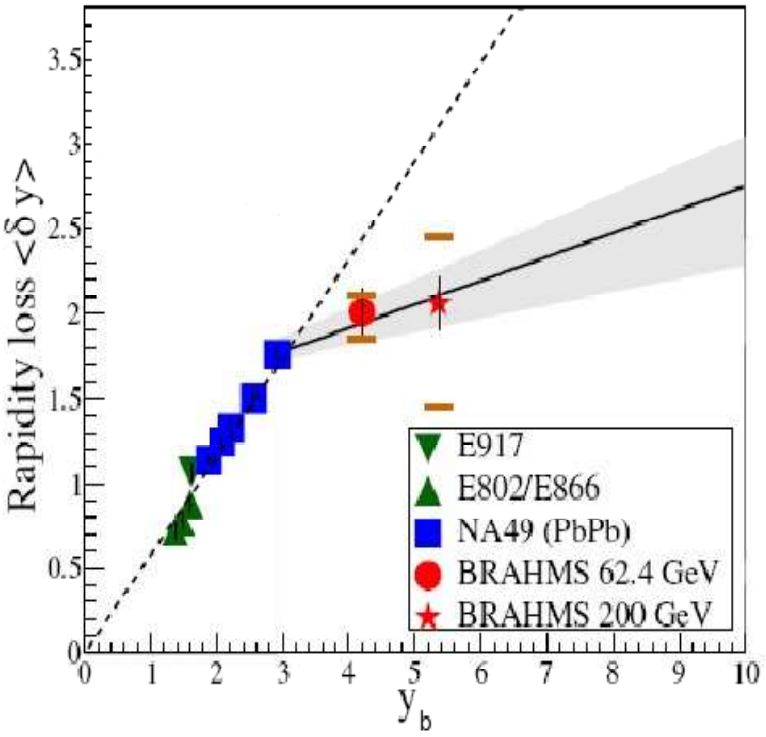

Figure 1.1: The rapidity loss as a function of beam rapidity for heavy ions collisions at AGS, SPS and RHIC. The solid line represents the fit to the SPS and RHIC data. The grey band is the statistical uncertainty. The dashed line is linear fit to the AGS and SPS results [21]. The plot is published in [19].

From BRAHMS measurements at top RHIC energy one can conclude that the midrapidity region of the collision is almost net-baryon-free. It corresponds to picture of interacting matter proposed by Bjorken [22] with near free net-baryon content at midrapidity. At lower energy, $\sqrt{s_{NN}} = 62.4$ GeV, for Au+Au reactions at $y \approx 0$ the net-proton $\frac{dN}{dy}$ indicates that the medium is also quite transparent compared with data at SPS and AGS energy [21].

1.2.2 Nuclear Modification Factor

At extremely high energy density, which is supposed to be obtained during heavy ions collisions at ultra-relativistic energies, one can expect that in the colour charged medium the suppression of the produced particles might be significant. Due to energy loss of high-p_T partons caused by the gluon radiation, particle production in Au+Au collisions at RHIC energies is regarded to be suppressed with reference to the p+p reactions yield. The measure used to explore the medium effects is called nuclear modification factor, R_{AA}. The R_{AA} is defined as the ratio of the particle yield produced in the nucleus-nucleus collision, scaled with the number

of binary collisions, and the particle yield produced in nucleon-nucleon reaction:

$$R_{AA} = \frac{1}{\langle N_{coll} \rangle} \frac{d^2N^{A+A}/dp_T dy}{d^2N^{p+p}/dp_T dy} \tag{1.4}$$

where:

N_{coll} - the number of binary collisions at given centrality cut.

At low p_T, where the production scales with the number of participants, N_{part}, R_{AA} should converge to N_{part}/N_{coll} which is 1/3 for heavy ions systems. Particles with high p_T are primarily produced in hard scattering, early in the collision. In nucleus-nucleus reactions hard scattered partons might travel in the medium. Assuming that the partons traverse through QGP, they loose a large fraction of their energy by induced gluon radiation, suppressing the jet production. Experimentally, knowing as the jet quenching [15], it can be observed as a depletion of the high p_T region in hadron spectra. For Au+Au reactions at $\sqrt{s_{NN}} = 200$ GeV it is observed [24] that, in fact, mesons and baryons are suppressed for nucleus-nucleus collisions in reference to the elementary (p+p) reactions in the whole rapidity range at $p_T < 1.5$ GeV/c. At larger transverse momentum the nuclear modification factor at mid- and forward rapidity for pions is $R_{AA} < 0.6$ and $R_{AA} < 0.4$, respectively. Though, for protons the value of R_{AA} successively increases with rising p_T. These outcomes might indicate that the dense state of quarks and gluons produced at midrapidity remains right up to the forward region. The increase of R_{AA} for protons may be related to radial flow of medium created in Au+Au reactions that boost produced protons to larger p_T. This phenomenon can be also explained by quark coalescence models [51, 25]. Considering the above presented scrutiny it is also additional motivation to study the pion and proton production ratio in conjunction with rapidity dependence.

1.2.3 Color Glass Condensate

The observations for d+Au collisions at $\sqrt{s_{NN}} = 200$ GeV, which might indicate the existence of Color Glass Condensate state, were one of the most exciting results obtained by BRAHMS experiment at RHIC. It is discussed widely in [18, 27].

From equation 1.4 one can conclude, in the absence of nuclear effects, the nucleus-nucleus collisions can be interpreted as a superposition of hard nucleon-nucleon interactions at high p_T ($R_{AA} \approx 1$). At RHIC energies, for d+Au collisions we do not expect to produce an extended hot and dense medium. The nuclear modification factor for hadrons measured for d+Au collisions exhibits at $y \approx 0$ typ-

ical Cronin enhancement [26]. This enhancement is known from SPS measurements as the Cronin effect and is associated with partonic multiple scattering - an initial state broadening of the distribution of quark momenta. When we go to more forward rapidities BRAHMS has observed [18] a significant suppression at high p_T starting already at $\eta = 1$ and increasing with increasing pseudorapidity. The existence of the Color Glass Condensate might be an explanation of this effect in forward regime [28]. The ground state nuclei has a large number of low-x gluons - where x is the fraction of the longitudinal nucleon momentum carried by parton. As a result of interacting gluons with each other an augmenting of gluons takes place with decreasing x. It happens until the characteristic momentum scale, known as the saturation scale Q_s, is reached. Precisely, not the whole amount of gluons stop increasing, but only that one with gluon size larger than $1/Q_s$. This state is seen in d+Au interactions where the low-x components (mostly gluons) of the wave function of the gold nuclei are probed by deuteron parton rescattered at forward region.

Comparing the nuclear modification factor for pions, kaons and protons for central and peripheral centrality at the same rapidity for d+Au reactions at $\sqrt{s_{NN}} = 200$ GeV there is noticeable difference [18]. In the case of $y = 0$ we can observe a significant enhancement, especially for protons near $p_T \approx 2$ GeV/c. For central collisions at forward rapidity the suppression of R_{AA} is evident for all kinds of hadrons. For peripheral reactions the effect is not so appreciable.

On the other hand, in Dual Parton Model the addition of dynamical shadowing correction has been incorporated to describe the R_{dAu} behaviour [29].

1.2.4 Elementary collisions

The p+p collisions at $\sqrt{s} = 200$ GeV and 62.4 GeV are often treated as the reference to the heavy ions interactions to extract the nuclear effects. At RHIC it has been shown that particle production in p+p reactions at ultra-relativistic energies conveys new tasks to accomplish, especially in the context of rapidity dependence. The single-transverse-spin asymmetries A_N or net-baryon distribution issues are worth pointing out [31, 35].

The BRAHMS measurements at forward rapidity are exceptionally interesting. At forward rapidities in p+p reactions the produced particles are from the kinematic region where large-x valence quarks ($0.3 < x < 0.7$) from the beam side rescatter on small-x gluons ($0.001 < x < 0.1$). In 2007, BRAHMS Collaboration published data for $\pi^-, \mathrm{K}^+, \mathrm{p}, \bar{\mathrm{p}}$ for p+p collisions at $\sqrt{s} = 200$ GeV for $y \approx 3$ and compared them with the Next-to-Leading-Order perturbative Quantum Chromodynamics (NLO pQCD) calculations [32, 33]. The calculations utilized set of frag-

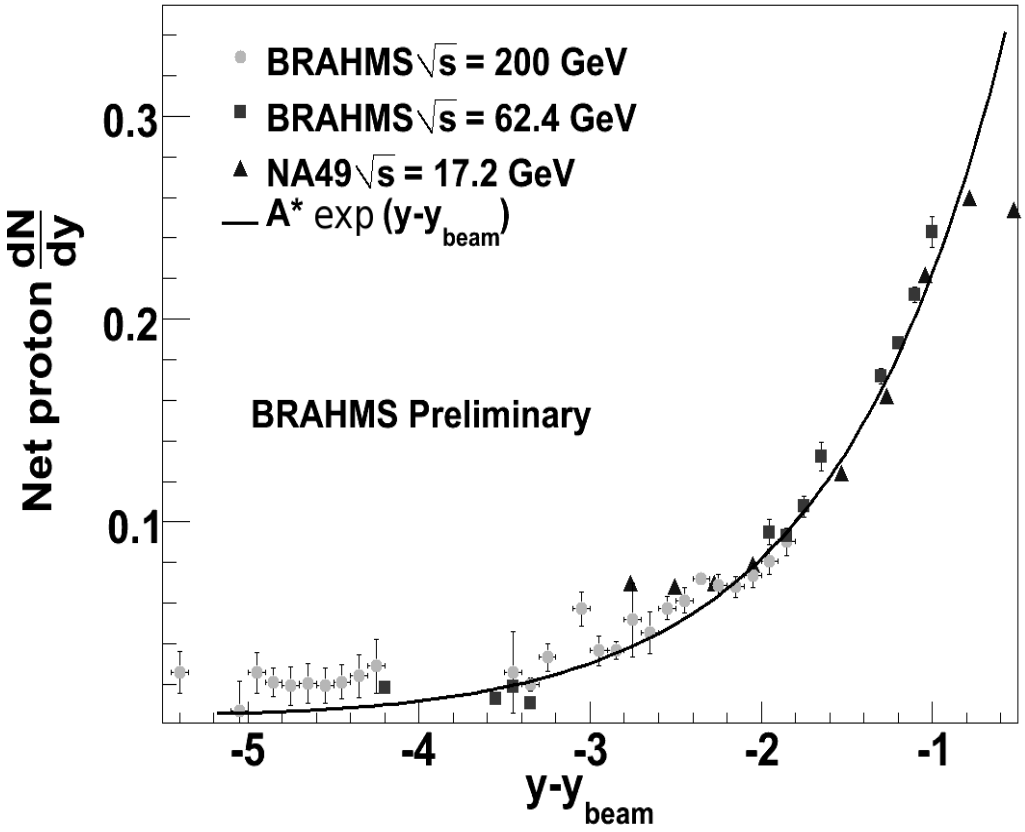

Figure 1.2: The net-proton distribution in p+p collisions as a function of rapidity shifted by y_{beam}, $y - y_{beam}$, compared with data from NA49 at $\sqrt{s_{NN}} = 17.2$ GeV. The picture has been published in [35].

mentation functions (FFs), namely the modified 'Kniehl-Kramer-Potter' (mKKP) fragmentation functions (FFs), a 'Kretzer' (K) and 'Albino-Kniehl-Krame' (AKK) functions. For pions and kaons the agreement is remarkable for mKKP FFs and it is interpreted as an evidence of the domination of gluon-gluon and gluon-quark processes at $y \approx 0$. This observation at forward regime is supported by the comparison with neutral pion and direct photon spectra obtained by STAR experiment [30]. At high rapidity a good description of baryon yield is provided by AKK functions revealing that the contribution of gluons fragmenting into protons (antiprotons) is dominant (80% for $p_T < 5$ GeV/c). One can say that NLO pQCD calculations describes the BRAHMS results very well and it is a milestone in understanding elementary interactions.

In elementary collisions, at midrapidity regime Bjorken scenario [22] predicts the antiparticle-to-particle ratio to be close to 1. In turn, at forward rapidity

the leading particles and projectile fragments dominate in the cross section [34]. The net-proton distribution in proton-proton collisions at both energies: $\sqrt{s} = 62.4$ GeV ($y_{beam} = 4.2$) and $\sqrt{s} = 200$ GeV ($y_{beam} = 5.3$) as a function of rapidity shifted by y_{beam} is presented in Fig. 1.2. The results of NA49 experiment [36] are also shown. As it has been observed the increasing difference between antiproton and proton yield with increasing rapidity, viewing from the rest frame of one of the protons, does not depend on the incident beam energy. The remarkable overlap of experimental data strongly suggests that we should not expect any new mechanisms in proton-proton reactions in the covered colliding energy interval.

1.3 Organization of the thesis

1. Chapter 2 includes the theoretical interpretation of p/π ratio p_T-dependence in the RHIC range of baryo chemical potential.

2. Chapter 3 presents the BRAHMS experimental setup used to measure data presented in this thesis.

3. Chapter 4 describes the details of the data analysis.

4. Chapter 5 displays the obtained results on p/π ratios and compares them with different hadronization scenarios.

5. Chapter 6 presents the summary of analysis.

6. Appendix 1 introduces the main kinematical variables.

7. Appendix 2 lists the numbers of runs for particular settings for each colliding system and energy. The specification of working triggers during measurements is displayed.

Chapter 2

Motivations

2.1 Nucleus-nucleus collisions at RHIC energies

At RHIC, where the gold and copper nuclei are collided, the heavy ions reactions give the great opportunity not only to search for evidences of QGP creation, but also to explore properties of hot and dense medium.

Heavy ions collision at relativistic energies is often displayed as two flatten "pancakes" passing through one another [43]. That flattening appears due to Lorentz contraction. In the wake of nuclei is left melting coloured glass, which finally materializes as partons (quarks and gluons) [27]. These partons would naturally emerge in their rest frame, characteristic for saturated colour glass, microscopic time scale which at RHIC is $\frac{1}{Q_s} \approx 0.2 \frac{\text{fm}}{c}$ (where Q_s - saturation momentum [44]). With rapidity along beam axis and because of the Lorentz time scale dilation particles with small rapidity (low momentum) are produced in the center of collisions and with large y - away from centre, close to the beam fragmentation regime. That view is close to the Bjorken scenario [22] which is a description of hydrodynamical expansion on which, nowadays, a lot of hydrodynamics calculations are based [12]. The hydrodynamics approaches delineate the space time evolution of perfect fluid system with viscosity close to 0. The very good agreement of the computations with experimental data [8] - the momentum distribution and collective flow - indicate that at the very beginning of the interaction the strongly coupled Quark Gluon Plasma is formed [7].

The expansion of the interacting matter during collision is schematically sketched in Fig. 2.1. Just after the moment of collision the hot and dense system starts to expand and cool down. It is supposed that in the moment of interaction the energy density of matter is $\epsilon \sim 5$ GeV/fm^3 [6]. At the pre-equilibrium state the quasi quarks and gluons occur and afterwards it might lead to the local thermal

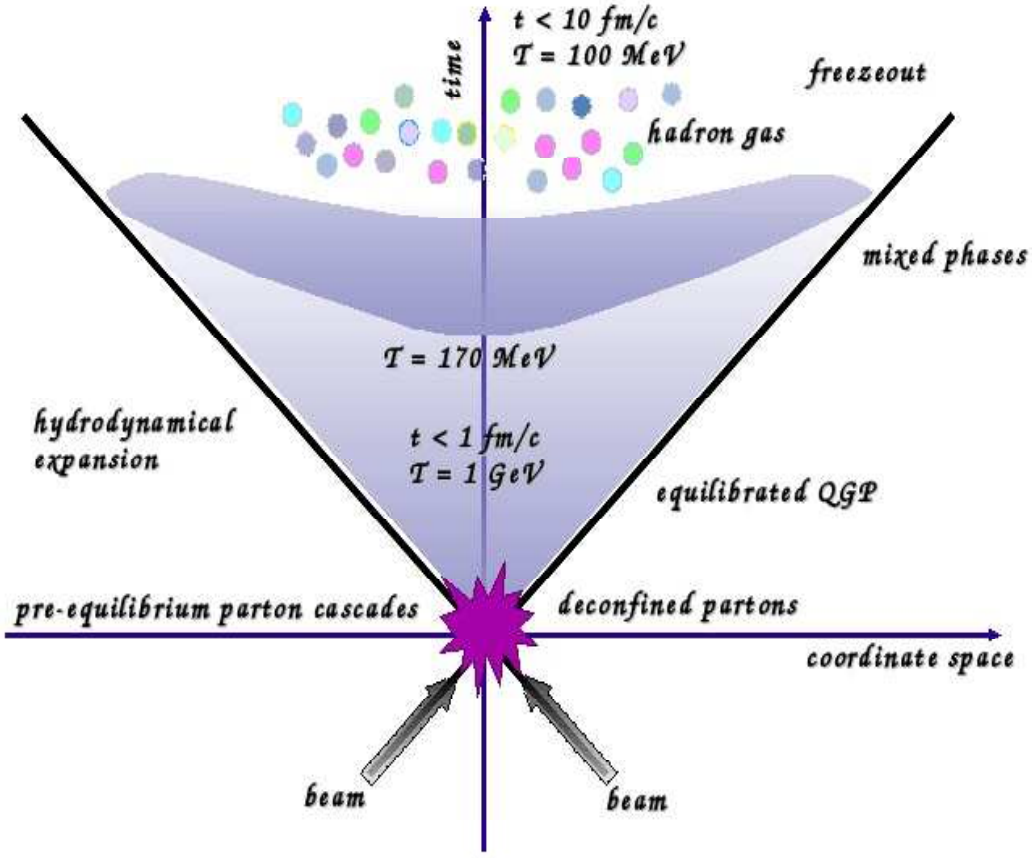

Figure 2.1: Schematic space-time picture of nucleus-nucleus collision.

equilibrium with well-defined space-time expansion. The partons may thermalize after 0.2 $\frac{\text{fm}}{c}$. If the local equilibrium is reached in the system before 1 $\frac{\text{fm}}{c}$, the collective flow of QGP can be characterized by the hydrodynamic evolution. With increasing time, decreasing energy density and temperature the Quark Gluon Plasma state turns into the mixed phase of quarks, gluons and hadrons - QGP starts to hadronize. The produced hadrons might decay into stable particles and interact with each other. Eventually, the produced particles are being detected in the experimental counters.

2.2 QCD phase diagram

Phase transitions are common phenomena related not only to water or widespread substances, but also to nuclear matter. Almost everybody knows the transitions between ice → water → steam while adding heat to the system. A similar processes are expected to occur when we add heat to the system of nuclear matter (or going in reverse) [43]. In the heavy ion collisions where the strong interactions play the most important role we can monitor the process of "emerging" of the particles

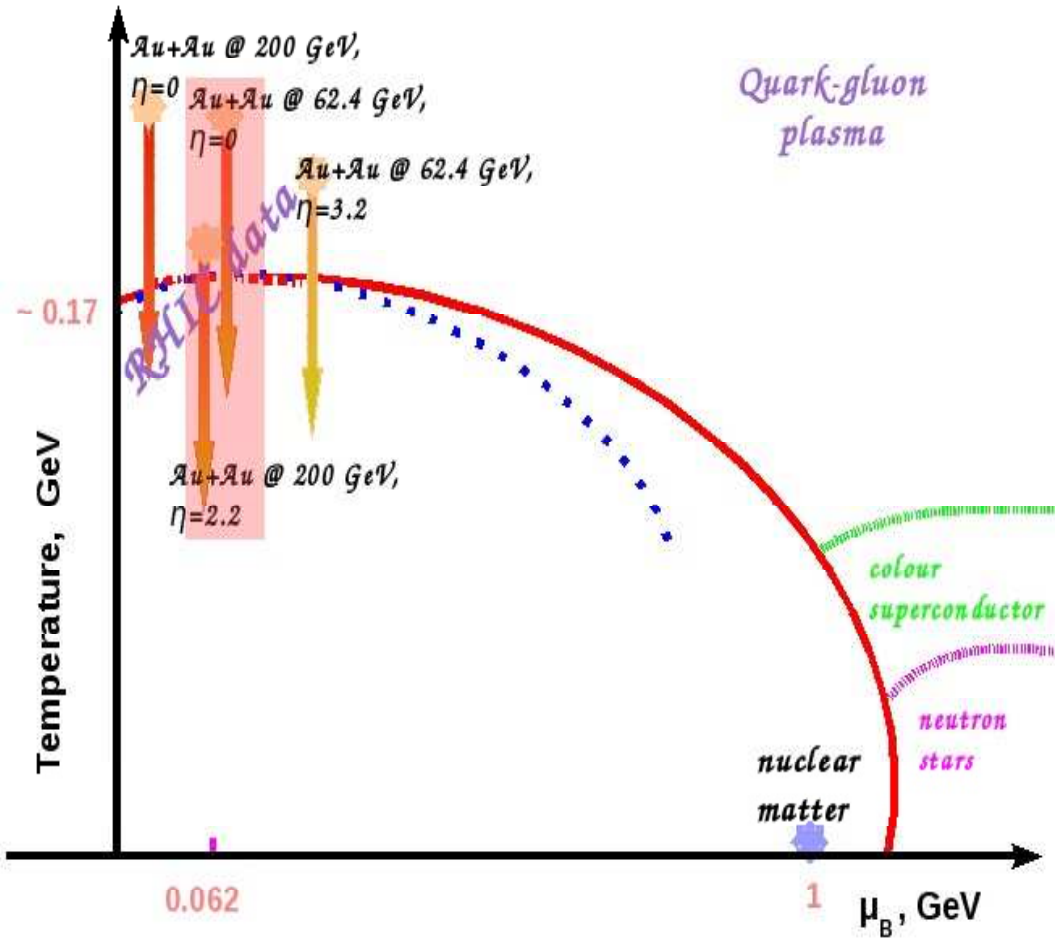

Figure 2.2: The scheme of QCD phase diagram: the dashed-dotted red line emblematizes the crossover between Quark Gluon Plasma and hadronic phase. The red solid line symbolises the 1st order phase transition. The dotted blue curve represents the chemical freezeout. The arrows denote the value of baryo chemical potential for definite colliding systems.

from the hot and dense nuclear matter.

In general, in thermodynamical framework one component system can be described using three variables which only two of them are independent. The QCD phase diagram is a plot of two independent thermodynamic variables, temperature τ and baryo chemical potential μ_B. The points (τ, μ), where a phase transition occurs, trace a line in the phase diagram thus a phase transition plot becomes a specific map of the different phases of interacting matter.

In the last decades, the intense theoretical and experimental investigations of the QCD phase diagram in the regime of partonic and hadronic gas phases led us to the picture depicted in Fig. 2.2 [46, 47, 48]. The dashed-dotted red line represents the crossover from Quark Gluon Plasma to the hadronic state procured from the lattice QCD calculations [37]. The computations show that the smooth crossover between the quark-gluon state and hadronic state should occur below $\mu_B \approx 400$ MeV (although, for infinitely large strange quark mass the models predict $\mu_B \leq 700$ MeV [38]) and above that value the first order transition of partonic and hadronic matter is predicted. Moreover, the theory predicts the critical point at the end of first order phase transition line. The critical point occurs for the second order phase transition and the value of critical temperature τ_c varies from 160-170 MeV [12, 37, 48]. The experimental measurements of hadronic species abundances allow us to outline the dotted blue line as the chemical freezeout of the hadronic gas. It is remarkable that at low baryo chemical potential the crossover and chemical freezeout curves overlap, albeit at large μ_B a significant gap between the temperature of the transition from the partonic to the hadronic phase, τ_c, and the temperature of chemical freezeout is predicted. At very high baryon density and low temperatures the colour superconductivity domain is predicted. It is also expected that the core of neutron stars can be characterized by high value of μ_B and low τ.

In this thesis I study the $p/\pi(p_T)$ ratio in nucleon-nucleon and nucleus-nucleus collisions at different colliding energy in the wide range of pseudorapidity. This research gives the possibility to answer the question how the properties of bulk medium carry out in the system with the increasing value of baryo chemical potential. As it has been show at low value of μ_B the recombination of partons is maintained [9]. To determine the essence of final state interactions the new exploration is desired. For studied experimental data the baryo chemical potential varies in the range: 26 MeV $< \mu_B <$ 260 MeV (see Fig. 9 in [6]).

2.3 Theoretical Developments

The intention of the next two sections is to present selected theoretical models that can be confronted with experimental approach of baryon and meson production.

2.3.1 Thermodynamical description

In order to apply thermodynamical approach to the nuclear matter produced in relativistic heavy ion collisions the following conditions must be fulfilled:

1. the system must be composed of many particles and its dimensions must be larger than the typical strong interaction scale ($\sim$ 1 fm)
2. the interacting matter is in the thermodynamical (thermal and chemical) equilibrium
3. the lifetime of system, t, is longer than the typical relaxation time ($t \gg 1$ fm/c).

In statistical physics there are three possible grasps of the characterization of the system: microcanonical, canonical and grand canonical ensemble [39]. Assuming the requirement of the variable number of particles during the collision, the grand canonical ensemble is the most appropriate. It includes opportunity to exchange the particles and energy for the local subsystem with the reservoir i.e. the whole system. In this case, we fix the temperature τ, volume V and chemical potential μ as a local condition. Consequently, if the system is described by a Hamiltonian H with a set of conserved number operators $\hat{N}_i$, the statistical density of matrix might be presented as:

$$\hat{\rho} = \exp[-\frac{1}{\tau}(H - \mu_i \hat{N}_i)] \tag{2.1}$$

which results in the grand canonical partition function as follows:

$$Z = \mathrm{Tr}\hat{\rho} \rightarrow Z = \sum_n < n|\mathrm{e}^{-(H-\mu\hat{N})/\tau}|n > . \tag{2.2}$$

Other thermodynamic properties can be derived from $Z = Z(V, \tau, \mu_1, \mu_2, ...)$:

$$P = \tau\frac{\partial \ln Z}{\partial V} \quad \rightarrow \quad P = \frac{\tau}{V}\ln Z \quad (V \rightarrow \infty)$$

$$N_i = \tau \frac{\partial \ln Z}{\partial \mu_i}$$
$$s = \frac{\partial(\tau \ln Z)}{\partial \tau}$$
$$\epsilon = -PV + \tau s + \mu_i N_i$$

where:
P - pressure, N_i - number of particles, s - entropy, ϵ - energy. According to that, we can get statistical multiplicity distribution, assuming that neither bosons nor fermions interact with each other when they are put in a box with sides of L [39]. On the other hand we should not forget that the thermal equilibrium is required which implies that the interactions of particles must exist. In this case the grand partition function takes form:

$$\ln Z = V \int \frac{d^3p}{(2\pi)^3} \ln(1 \pm e^{-(\epsilon-\mu)/\tau})^{\pm 1} \tag{2.3}$$

refering the (+) to fermions and (-) to bosons. Eventually, the number of particles can be described as:

$$N = V \int \frac{d^3p}{(2\pi)^3} \frac{1}{\exp[-(\epsilon-\mu)/\tau] \pm 1} \tag{2.4}$$

from which the differential multiplicity is easy to obtain:

$$\frac{d^3N}{dp^3} = \frac{V}{(2\pi)^3} \frac{1}{\exp[-(\epsilon-\mu)/\tau] \pm 1}. \tag{2.5}$$

At RHIC the chemical potential ($\mu \sim$ MeV) is incomparably smaller than the energies ($\epsilon \sim$ GeV), so $\rightarrow \exp[(\epsilon-\mu)/\tau] \gg 1$. Thus in Boltzmann limit it leads to:

$$\frac{d^3N}{dp^3} = \frac{V}{(2\pi)^3} \exp[(\mu-\epsilon)/\tau] \rightarrow exp[-\epsilon/\tau]. \tag{2.6}$$

The last expression is used with the assumption of the fixed value of the chemical potential. This equation is just the Boltzmann distribution of the many body system, being in principle the root for the hadronic spectra deliberations.

Through the exploration of the proton-to-pion production it might be studied the main difference between production of baryon - as a particle containing three valence quarks - and meson building up from quark and antiquark. From that point of view it is important to introduce variables such as strange and baryo chemical potential. In thermodynamics the chemical potential can be expressed as:

$$\mu_i = -\tau \left(\frac{\partial S}{\partial N_i} \right)_{U,V,N_{j\neq i}} \tag{2.7}$$

with the definition of entropy $S = S(U, V, N_1, ..., N_k) \rightarrow U$ - internal energy, $N_1, ..., N_k$ - the number of i particles. In high energy physics the chemical potential is assigned with the symmetries and charges and fulfills the condition of the quantity conservation. For every conserved quantum number we have a chemical potential i.e. baryon quantum number - baryo chemical potential, μ_B, strangness - strange chemical potential, μ_S, charge conservation - chemical potential connected with third component of isospin, μ_{I_3}. In the simplest way the baryo chemical potential, μ_B, can be interpreted as the energy indispensable to create the particle in the system.

In strong interactions the net-baryon density is conserved and in case of nucleus-nucleus collisions $\neq 0$. The total net-strangness is also conserved and equals 0.

With the assumption that chemical and thermal equilibrium has been obtained, the thermodynamical models describe the AGS and SPS experimental data quite well [41, 46]. The baryo chemical potential varies for that data from 200 to 600 MeV, for AGS and SPS, respectively. Studying particles yields and their ratios we can only conclude about the process of hadronization and the value of temperature and baryo chemical potential. With the thermodynamical approaches it is not possible to say if the Quark Gluon Plasma state has been created.

2.3.2 Quark recombination model

Below I give the brief introduction of the quark recombination model (complete description can be found in [49], [51], [52], [53], [54], [55], [56], [57]).

In Rudolph C. Hwa's grasp, the ongoing process of hadronization is divided into two parts depending on how the partons recombine. One touches on the midrapidity regime (here primarily considered at intermediate p_T because BRAHMS setup does not identify particles beyond $p_T > 8$ GeV/c) where the partons at high p_T are the source of thermal and shower partons which undergo coalescence. The whole calculations are done in the 1D-momentum space where the momentum $\mathbf{p}$ of measured hadron is defined in appointed direction. The R. Hwa's deliberations start with the distribution of quarks and antiquarks just before the process of recombination that indicates that initial processes which come out from dynamical origins are not taken into account. The specific recombination can only yield quarks and antiquarks, however gluons hadronize by conversion to $q\bar{q}$ pairs. The quark(q)-antiquark(q') (quark-quark-quark), in case of meson (baryon), can recombine in the

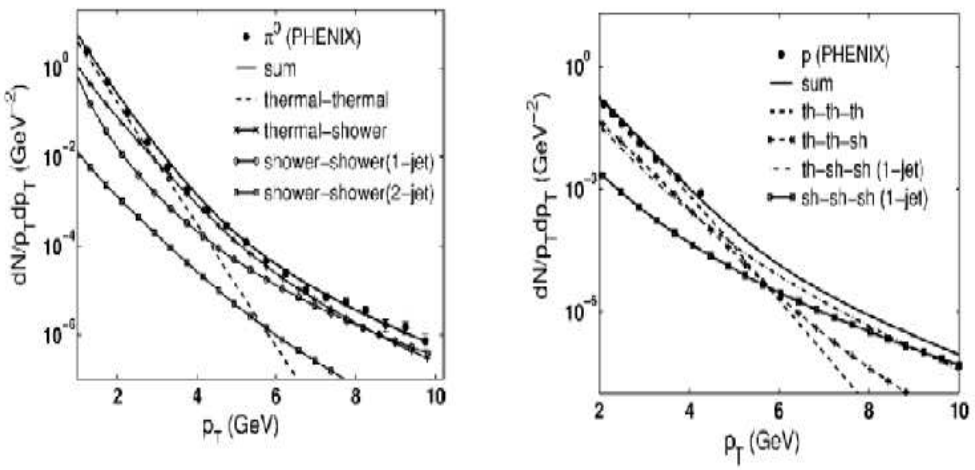

Figure 2.3: Transverse momentum distribution of pions π^0 (left-hand side) and protons (right-hand side) for Au+Au collisions at $\sqrt{s_{NN}} = 200$ GeV at the midrapidity region. Different contributions to the recombination of partons are depicted. The plots are taken from [53].

medium only if these partons are collinear (e.g. for mesons - quarks momentum: $p_q = p_{q'} = p$; azimuthal angle of emitted quarks from the collision: $\phi_q = \phi_{q'} = \phi$). Moreover, the hard scattering proves the increase of the number of partons with high p_T, but in presence of matter created after the collision, that number decreases due to the interactions with the colour charged medium inducing the energy loss. This effect is implemented phenomenologically by use of effective parameter ξ.

For $y = 0$ the inclusive distribution for a produced pion with momentum p can be written:

$$p\frac{dN_\pi}{dp} = \int \frac{dp_1}{p_1}\frac{d(p-p_1)}{p-p_1} F_{q\bar{q}'}(p_1, p-p_1) R_\pi(p_1, p-p_1, p) \tag{2.8}$$

where:

$F_{q\bar{q}'}$ is the joint distribution of a quark q at p_1 and antiquark $\bar{q}'$ at $p - p_1$ which recombine and $R_\pi(p_1, p-p_1, p)$ designates the recombination function for $q\bar{q}' \to \pi$ defined as follows:

$$R_\pi(p_1, p-p_1, p) = \frac{p_1(p-p_1)}{p^2}\delta\left(\frac{p_1}{p} + \frac{(p-p_1)}{p} - 1\right). \tag{2.9}$$

In the recombination function it is introduced almost 'by-hand' the Kronecker δ function to guarantee the conservation of momentum in the recombination process. That is the major weakness of all of the recombination (other name: coalescence) models where the conservation of momentum and energy does not ensue in natural way. In addition, as it is highlighted in [53], it is the reason why the pion wave

function in the momentum space is very broad.

For mesons the joint distribution function might be expressed schematically:

$$F_{q\bar{q}'} = TT + TS + (SS)_1 + (SS)_2 \tag{2.10}$$

where:

TT - represents contribution where two thermal (soft) partons eventually produce the thermal hadron

TS - stands for the thermal-shower pairs of quarks (considered in the $3 < p_T < 8$ GeV range)

$(SS)_1$ - represents the contribution of two shower partons having originated from one hard parton

$(SS)_2$ - contribution of two shower partons but coming from separate hard partons (at RHIC energies this contribution is negligible).

Each of these fractions contribute to the invariant inclusive pion distribution shown in Fig. 2.3 (left hand). Even at the highest RHIC's energy the shower-shower (2-jet)-$(SS)_2$ component contributes at least one order of magnitude less than the other components. Each contribution which includes the shower part is suppressed by the ξ factor characterizing fraction of existing partons which can hadronize going outside the reaction. In other words, it is defined as the fraction of the energy loss. At low p_T the most significant contribution in the joint distribution seems to be the thermal-thermal TT fraction usually connected with the soft component of pion spectra. For larger p_T the thermal-shower TS part plays an important role.

For baryons the invariant inclusive distribution goes as follows:

$$p\frac{dN_p}{dp} = \int \frac{dp_1}{p_1}\frac{dp_2}{p_2}\frac{dp_3}{p_3} F_{qq'q''}(p_1, p_2, p_3) R_p(p_1, p_2, p_3, p) \tag{2.11}$$

where:

$R_p(p_1, p_2, p_3, p)$ - the recombination function of proton,

$F_{qq'q''}$ is the joint distribution of three relevant quarks which form a proton.

For baryon the joint distribution function may be depicted in the schematic way: $F_{qq'q''} = TTT + TTS + T(SS)_1 + T(SS)_2 + (S(SS)_1)_2 + (SSS)_3$ where at RHIC range of energy only the first four contributions there are meaningful where, at most, the shower originate one hard parton.

All the fractional contributions to the proton spectrum are presented on

the right panel of Fig. 2.3. When $p_T < 2$ GeV/c the mass effect becomes important. The dominance of thermal-shower-shower (1-jet)-$T(SS)_1$ is observed especially at high p_T, but at lower value of transverse momentum the thermal-thermal-thermal TTT component is also valid. The recombination of the thermal and shower partons dominates at the intermediate p_T. The pion and proton spectra, obtained from the model calculations, have been used in attempt to get the proton-to-pion ratio vs. transverse momentum. This results are consistent with the p/π^+ ratio obtained experimentally and they are presented in section **5.1**.

The revision of the forward hadron production in the framework of the quark recombination model has been done recently [49]. It was inspired by the presented experimental data of p/π^+ ratio for Au+Au collisions at $\sqrt{s_{NN}} = 62.4$ GeV [58].

In forward production of hadrons one can distinguish two mechanisms which contribute to the recombination. One of them is related to the valence quark distribution, taking into account the three (for baryons, two - for mesons) collinear nucleons, coming from the projectile introduced as the tube with the same impact parameter $|\vec{s}-\vec{b}|$ in the target ($\vec{s}$ - configuration of nucleons in the target, $\vec{b}$ - impact parameter; notations the same as used in the Glauber model [59]). Of course, those three (two) nucleons, from which the contributing constituent quarks come, pass through the reacting zone and undergo collisions with the target which is implied in the sense of the degradation parameter κ. Moreover, the effect of successive collisions is in an indissoluble manner connected with the second contribution to meson and baryon production - regeneration. After ν collisions (notations like in [56]), the net momentum fraction lost defined as $1 - \kappa^\nu$ is gone in for conversion to soft partons (quarks+gluons) assisting the regeneration of the sea quark distribution. Similarly, as in the midrapidity regime, gluons can not recombine directly into hadrons, but firstly they are converted to $q\bar{q}$ pairs.

The way how both processes contribute to the hadron production depends on the species of particle. For protons, the valence quark fraction dominates over sea quarks at Feynman's variable x. Due to that impact the enhancement of proton over pion yield in the fragmentation region can be generated.

2.3.3 Hydrodynamical models

The hydrodynamical approaches [12, 65] are based on the following assumptions:

1. the system includes a large number of particles, as in the typical statistical

description

2. the interacting matter is treated as the continuous system where the dimensions are much larger than the distance between particles (in the sense of the scale of strong interactions $\gg 1$ fm)

3. as the dynamics of the medium we understand the dynamics of units of the continuous system-fluid

4. macroscopic variables are used to describe the thermodynamics of the system (i.e. entropy, initial energy); the collective motions of the units of the fluid are characterized by typical kinematical variables (i.e. $\vec{p}$)

5. the evolution of the fluid is described by the following equations:

   (a) energy and momentum tensor of ideal fluid

   $$T^{\mu\nu} = (\epsilon + P)u^{\mu}u^{\nu} - Pg^{\mu\nu} \tag{2.12}$$

   where:
   u^{μ} - four-velocity of the unit of the medium, $g^{\mu\nu}$ - metric tensor

   (b) energy and momentum conservation

   $$\partial_{\mu}T^{\mu\nu} = 0 \tag{2.13}$$

   (c) the thermodynamical variable can be expressed as the function of the proper time: $\epsilon = \epsilon(t)$, $p = p(t)$, $\tau = \tau(t)$ with the thermodynamical relations

   $$\epsilon + P = \tau s; \quad dP = sd\tau; \quad d\epsilon = \tau ds \tag{2.14}$$

   where:
   ϵ - energy density, P - pressure, τ - temperature, s - entropy

   (d) for boost-invariant expansion in the longitudinal direction the equation of motion takes form:

   $$\frac{\partial\epsilon}{\partial t} + \frac{\epsilon + P}{t} = 0 \quad \rightarrow \quad \epsilon t^{4/3} = \text{constant.} \tag{2.15}$$

6. initial conditions of evolving system

   - local thermodynamic equilibrium

- entropy and baryon density are proportional to the participating nucleon distribution

$$s(x,y,\tau_0) = \frac{C_s}{\tau_0}\frac{dN_p}{\tau_0 dxdy}; \quad n_B(x,y,\tau_0) = \frac{C_{n_B}}{\tau_0}\frac{dN_p}{dxdy} \tag{2.16}$$

- equation of state - [12, 61, 62]

  The equation of state is associated with the state variables such as temperature, pressure, baryon density, energy density. In general the state of nuclear matter might be deliberated with different assumptions: 1) the matter is treated as ideal relativistic gas with massless particles or 2) the phase transition between partonic and hadronic state occurs and finally particles with mass are produced or 3) going from high energy density state described by bag model to low energy density matter where the gas of hadronic resonances is concerned.

- while the fireball of fluid is evolving, the temperature and density decrease unless the system accomplishes freezeout stage; the invariant single-particle distribution from freezeout surface is calculated according to the Cooper-Fry's formula [63, 64]:

$$E\frac{dN}{d^3p} = \int f(x,\mathbf{p})p^\nu \cdot d\sigma_\nu = \frac{d}{(2\pi)^3}\int \frac{p^\nu \cdot d\sigma_\nu}{\exp[(p_\nu \cdot u^\nu - \mu(x))/T(x)] \pm 1} \tag{2.17}$$

  where:
  E - energy of the particle, $\mathbf{p}$ - momentum of the particle, $f(x,\mathbf{p})$ - Lorentz-invariant distribution function, u - four-velocity, $\mathrm{d}\sigma_\nu = (d^3x, \vec{0})$ - freezeout (hyper)surface, μ - chemical potential, d - degeneration component (e.g. d=3 for pions), T - freezeout temperature.

2.3.3.1 The non-boost-invariant single-freezeout model

The description of the non-boost-invariant single-freezeout approach is presented in [50, 65]. The model utilizes only the space-time hadron distribution after the simultaneously kinematical and thermal freezeout, hence it is so-called single-freezeout model. The produced hadrons evaporate from hypersurface, Σ, at the successive stage of the expansion of the fireball. It does not include the jet production, so it concerns only the "after-freezeout" component of produced

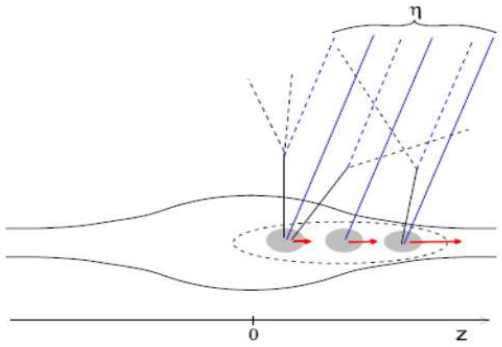

Figure 2.4: The evolution of the fireball along longitudinal axis (red arrows) with depicted tracks of produced hadrons for particular value of pseudorapidity η (dashed lines). The picture is taken from [50].

particles in relativistic heavy ion collisions. The non-boost-invariant dynamics of the system are particularly interesting with taking into account its simplicity. With all typical hydrodynamical initial conditions, the evolution of the interacting matter is shown as the evolving fireball (as presented in Fig. 2.4) with the well-defined 3+1-dimensional hypersurface Σ from which the collective emission of hadrons takes place. In every step of iteration of particles "evaporation", the produced hadrons occupy states described by Fermi-Dirac or Bose-Einstein distribution (with regard to particle specie). The determined thermodynamic parameters are temperature τ and chemical potentials: μ_B (baryon), μ_S (strange), μ_{I_3} (connected with third component of isospin) depending on the position of freezeout hypersurface Σ. The Hubble-type flow of produced particles has two - longitudinal and transverse - components:

$$\text{longitudinal flow:} \quad v_z = \tanh\alpha_{\parallel} = \frac{z}{t} \tag{2.18}$$

$$\text{transverse flow:} \quad v_\rho = \tanh\alpha_{\perp}. \tag{2.19}$$

Hence, the spatial rapidity can be defined as follows:

$$\alpha_{\parallel} = \text{arc tanh}\frac{z}{t}. \tag{2.20}$$

In the model the parametrization of freezeout hypersurface is included with the transverse radius expressed as follows:

$$\rho = \sqrt{x^2 + y^2} = \tau_1 \mathrm{sinh}\alpha_\perp. \tag{2.21}$$

Moreover, three parameters: τ_1, $\rho_{max}^{(0)}$, Δ are introduced to deliberate the spatial evolution of the fireball where the first one characterizes the proper time, second one - the transverse size at midrapidity and the third parameter is used to control the spatial rapidity $\alpha_\perp$.

If the fireball expands in the longitudinal direction (z-axis on the Fig. 2.4) $\alpha_\parallel$ increases. The maximum spatial rapidity can be expressed as:

$$0 \leq \alpha_\perp \leq \alpha_\perp^{max}(\alpha_\parallel) \equiv \alpha_\perp^{max}(0)\exp\left(-\frac{\alpha_\parallel^2}{2\Delta^2}\right). \tag{2.22}$$

In this equation the Δ parameter describes decrease of hypersurface Σ in transverse dimension with $\alpha_\parallel$. It is also introduced the dependence of chemical potential on spatial rapidity $\alpha_\parallel$:

$$\mu(\alpha_\parallel) = B\mu_B(\alpha_\parallel) + S\mu_S(\alpha_\parallel) + I_3\mu_{I_3}(\alpha_\parallel). \tag{2.23}$$

It entails some consequences. The standard performance in the thermal model adopts the chemical and thermal values of temperature ($\tau_{chem} \geq \tau_{kin}$) consistent with chemical and kinematical freezeout [41, 67, 68]. In the single-freezeout model the constant value of the temperature is set for both chemical and kinematical freezeout - $\tau = 165$ MeV (for $0 < \mu_B < 250$ MeV). Moreover, the hadrons resonances are applied in the calculations. It is estimated that at relativistic energies 75% of pions origins from the decays of resonances. Additionally, it is an effective way to contribute to decrease the temperature of spectra $\sim$ 35-40 MeV and influences the slope of the particles spectra.

The model includes ten parameters which should be fit to the experimental data (the details of fitting procedure is presented in [66]). The simulations are done using the THERMal heavy IoN generATOR (THERMINATOR) to get the Monte Carlo events. As the result of the calculations one can get the net-strangness of the system equals 0 for gold-gold collisions that is a success of the model.

The main attainment of the single-freezeout model is good agreement with the BRAHMS spectra of mesons and baryons for Au+Au collisions at $\sqrt{s_{NN}}$ = 200 GeV in the wide range of rapidity [50]. The results of single-freezeout model obtained for Au+Au collisions at $\sqrt{s_{NN}}$ = 200 GeV and 62.4 GeV [66] can be found in the chapter **5** section: **5.1** and **5.2**.

Chapter 3

Broad RAnge Hadron Magnetic Spectrometers at RHIC

3.1 Relativistic Heavy Ion Collider

The Relativistic Heavy Ion Collider is located in Brookhaven National Laboratory on Long Island in the USA [43]. It is dedicated to conduct research of heavy ion reactions at the ultra-relativistic highest available energies. At the main acceleration rings there are situated four experiments which engage various aspects of the strong interacting matter. STAR and PHENIX experiments have the ability to detect the wide spectrum of the particles at midrapidity with high momentum coverage. The PHOBOS experiment is designed to explore the low p_T regime of the interactions with the overall look of the collisions. The BRAHMS experiment, in turn, can identify particle over the widest range of rapidity, y, and transverse momentum, p_T.

The RHIC facility - depicted in Fig. 3.1 - is composed of the apparatures which are used in the successive steps of nuclei accelaration. The first step is to prepare the bunches of the ions in the Tandem Van der Graaff. The Tandem "peels off" the electrons from the atoms (gold or copper) and boost positive charged ions to the of 385 MeV. Afterwards, bunches are transferred by the Tandem-to-Booster line to the Booster synchrotron. The Booster synchrotron and then the Alternating Gradient Synchrotron are capable to propel the ions to the energy of 1 GeV/nucleon and 10 GeV/nucleon, respectively. The special design of the magnetic field gradient of the accelerator's magnets allows to be focused in the vertical and horizontal direction. It causes that the transfer of energy might be larger and the field makes possible to concentrate the beam in the little tight space. It is worth mentioning that proton beam with maximum energy of 200 MeV is delivered to the AGS from

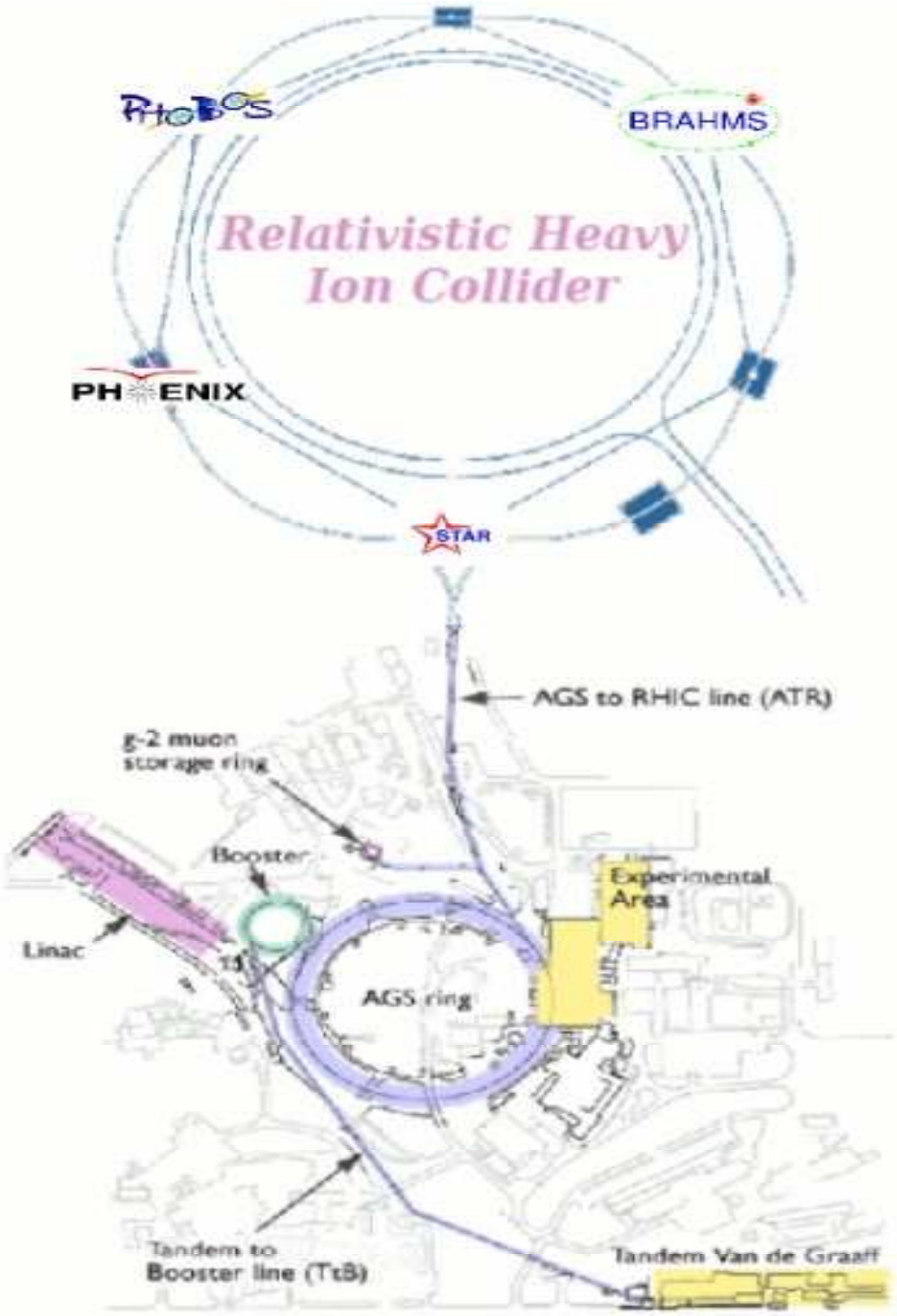

Figure 3.1: Overview of Relativistic Heavy Ion Collider in Brookhaven National Laboratory.

the LINAC (linear accelerator) where the protons are carried through the nine accelerator radiofrequency cavities. From the AGS the bunches of the nuclei migrate to the AGS-to-RHIC crossroads where some of the ions are directed to clockwise RHIC ring and the other part goes to the counter-clockwise RHIC ring (it is often described as blue and yellow beam). The beams are circulated and are rumped up to desired energy in the RHIC ring where the ions are collided in the four so-called beam intersection regions: BRAHMS, PHENIX, PHOBOS and STAR facilities.

I focus on the data for Au+Au collisions and p+p reactions at $\sqrt{s_{NN}}$ = 62.4 GeV and 200 GeV which were collected in 2004 (Au+Au) and 2005/2006 (p+p). The number of runs taken during three BRAHMS experiment campaigns together with information of colliding system, beam energy and spectrometer settings are listed in **Appendix 2**.

3.2 BRAHMS detector setup

The BRAHMS detector setup - Fig. 3.2 - consists of two movable spectrometer arms: the Midrapidity Spectrometer (MRS) which operates in the polar angle interval from $30^\circ \leq \Theta \leq 90^\circ$ (that corresponds with the pseudorapidity interval $1.3 \geq \eta \geq 0$) and the Forward Spectrometer (FS) that operates in the polar angle range from $2.3^\circ \leq \Theta \leq 15^\circ$ ($4 \geq \eta \geq 2$). Moreover, the overall particle multiplicity, collision vertex and centrality are determined using the global detectors. Although both of the spectrometers are very narrow, by the rotation of arms the spectrometer can cover a lot of phase space (see Fig. 5.1 in section **5.1**).

The Midrapidity Spectrometer is located perpendicular to beam axis, close to the nominal reaction vertex. In the MRS the particles are registered in the transverse direction to the beam axis. The single dipole magnet, D5 (notations like in the Fig. 3.2), placed between two Time Projection Chambers, TPM1 and TPM2, which compose the midrapidity arm, are used for tracking. Cherenkov detector (C4) and Time of Flight Wall (TOFW) measurements allow to identify particles with the separation of π/K and p/K up to 2 GeV/c and 3.5 GeV/c, respectively.

The front forward arm is composed of two Time Projection Chamber (TPCs), T1 and T2 (constituting track recognition in the high multiplicity environment), the back part - of three Drift Chambers (T3, T4, T5). All the chambers - T1, T2, T3, T4, T5 - operate in a high momentum mode. The forward going particles are swept by the two dipoles (D3, D4) toward the back end of the spectrometer where they are tracked in Drift Chambers - Fig. 3.3. The particle momenta are determined by these measurements and requirement of passing through another two

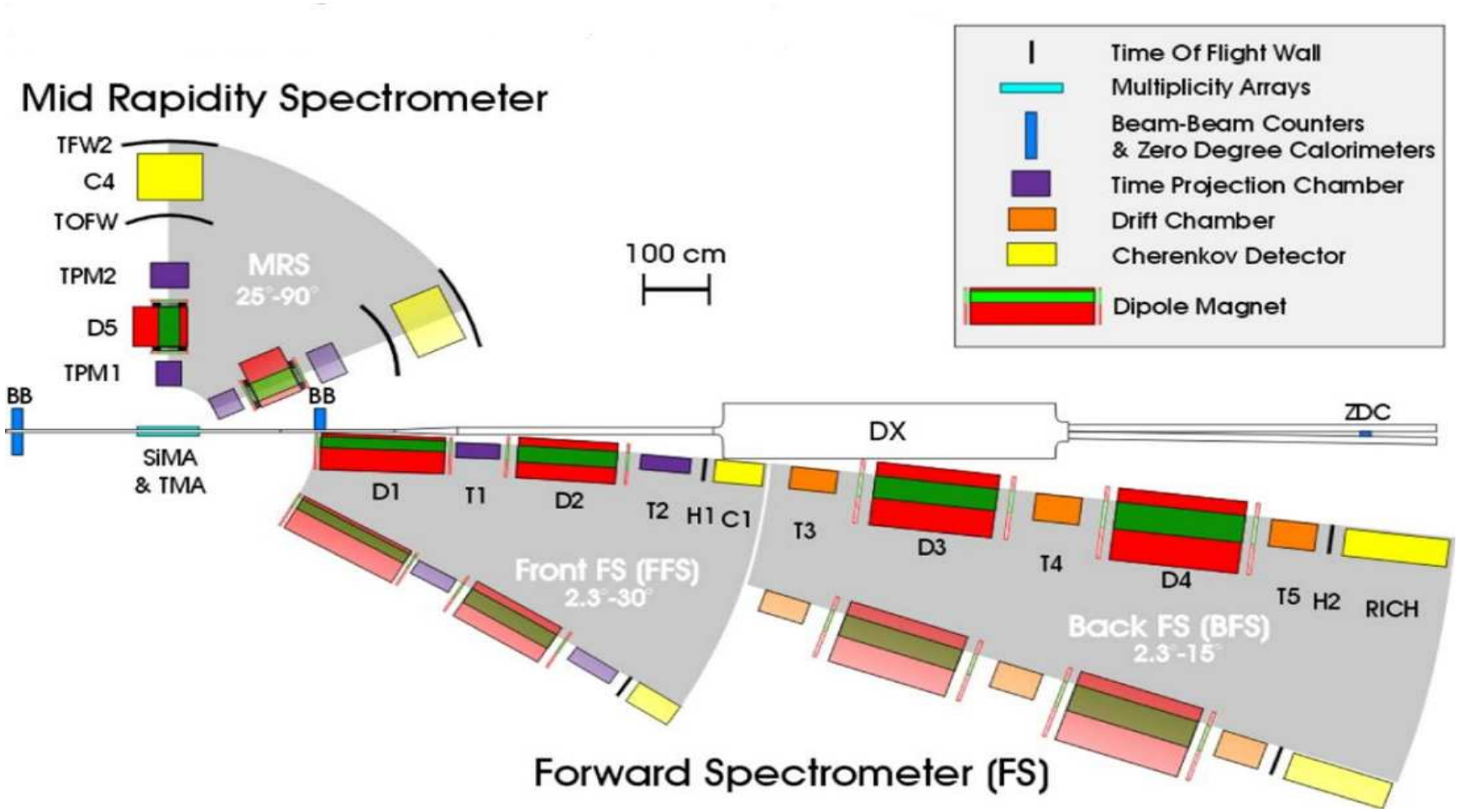

Figure 3.2: BRAHMS detectors layout.

dipoles (D1, D2). Particle identification (PID) is provided via the H2 hodoscope and Ring Imaging Cherenkov detector (RICH, situated behind H2 detector) for low and high momentum particles, respectively.

Let introduce a notation used to describe particular spectrometers settings, taking as an example "3A3450". The number before the capital letter, in this case "3", means the angle between the arm of the spectrometer relative to the beampipe. Further, the letter signifies the polarity of the magnetic field in the dipole magnets what simultaneously is linked with the measurement of the particle charge. With the polarity "A" the negatively charged particles can be measured (e.g $e^-, \pi^-, K^-, \bar{p}$), with "B" - the positive ones (e.g. e^+, μ^+, K^+, p). The last set of numbers is connected with the value of the magnetic field in the dipole magnet D5, in case of MRS, or in the first magnet of the forward layout of detectors, D1. It is presented in the units of current in that magnets [A].

Moreover, in the following sections we accept the ensuing coordinate system: z is the direction along the longitudinal axis of the spectrometer, y is the axis determined as perpendicular to the surface including the z direction and beam axis, x - perpendicular to y axis in the dispersive direction.

The details of the BRAHMS experimental setup can be found in the [69].

3.2.1 Time Projection Chambers

In the BRAHMS layout the Time Projection Chambers are the T1 and T2 detectors located just at the beginning of the forward arm and TPM1 and TPM2 in the MRS. Because of the location of the beginning of the spectrometers arms the intensity of tracks is extremely high.

The TPCs are used to trace the particle in 3-dimensions. All four chambers are segmented where in each part of the chamber the drift time is used to set the y position and determine the position of the induced signal in the $x - z$ plane. While the primary charged particle is passing through the active area of chamber, it causes the ionization of gas. The produced electrons drift in the homogenous electrical field incite the avalanche which is registered by the read-out electronics. In BRAHMS TPCs the minimum ionizing charged particle gives the 90 electrons per centimeter. The stroke of the voltage between the anode and cathode plane is near 5000 V. The drift length is equal 21.8 cm and the field - 229 V/cm.

The pad planes (see Fig. 9 and 10 in [69]) which constitutes the active zone of the chambers were planned in way that the three to five pads should collect the charge generated by the primary charged particle. Therefore, the signal is am-

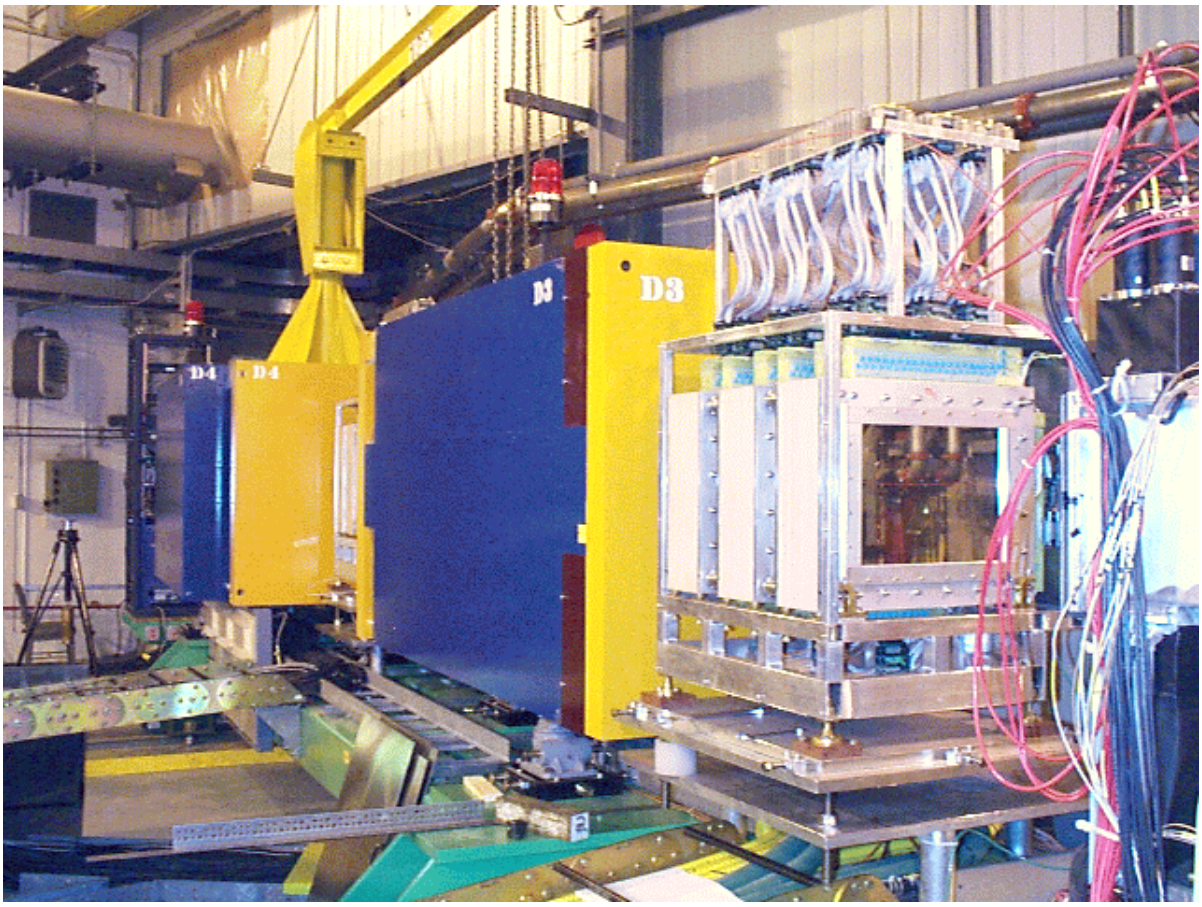

Figure 3.3: The photo of the back part of the Forward Spectrometer with the drift chamber T3 at the front right side of the picture. The D3 and D4 dipole magnets are also shown.

plified and integrated by low-noise, low-input impedance charge-sensitive amplifier followed by the shaping amplifier. The amplitude of the pad signal and its time history, covering the maximal drift time, are fed to a switched capacitor array analog memory clocked at 10 MHz.

The active volumes (x, y, z) of the T1 and TPM1 detectors are quite similar ($33 \times 22 \times 56$ cm^3 and $37.5 \times 21 \times 36$ cm^3, respectively), however the T2 active size is duplicated due to its specific localization in the spectrometer. In case of TPM2 the dimensions are: $50 \times 22 \times 67.5$ cm^3. The gas mixture, which was acknowledged as the most appropriate, is 90% Ar and 10% CO_2 due to its slow drift velocity, low transverse and longitudinal diffusion constants.

In general, the resolution of the TPCs in BRAHMS setup was obtained < 390 μm in x-position and between 390-490 μm in y direction. With that intrinsic precision one is able to differ two hadron tracks better than 15 mm.

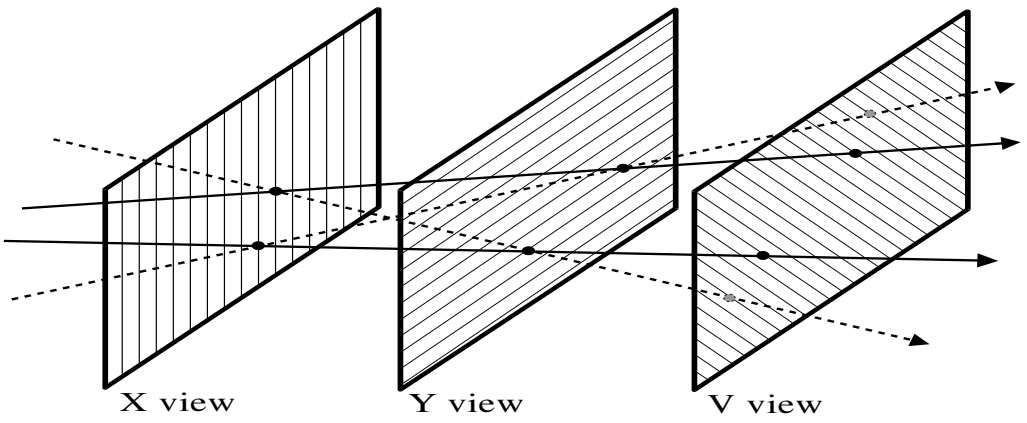

Figure 3.4: Two tracks (solid lines) identification using three different "views" of the detection planes. The third detection plane ("V view") allows to reject spurious tracks (dashed lines).

3.2.2 Drift Chambers

The Drift Chambers - T3, T4, T5 - used for tracking charged hadrons are situated in the back part of the Forward Spectrometer. Near the end of the FS, where detector T5 is located the expected multiplicities are quite low, with typical number of charged particles being smaller than 1 per event. It sets only modest requirements for tracking and particle identification at this position. On the other hand, the charged particle multiplicities in T3 are higher and reach values of up to 8/event. The very high background rate in T3 is due to the secondary emission in the beamline magnet DX. In order to meet the necessary tracking requirements, the detector T3 is constructed with a higher density of sense wires than the detectors T4 and T5. These latter share identical construction.

A single T3 prototype module as well as all three drift chambers with front end electronics were designed and built in the Division of Hot Matter Physics at Jagiellonian University. The Polish group was responsible for performance and maintenance of those detectors during all data taking campaigns of BRAHMS experiment.

The drift chambers are constructed as a set of drift cells which form a detection plane. Each detection plane is built from three frames made of epoxy-fiberglass. One frame contains the alternately ordered anode and cathode wires. Two frames with the field shaping wires are placed on both sides of the anode/cathode wires frame. The outer dimension of T3 detectors frames are 49 cm $\times$ 59 cm while

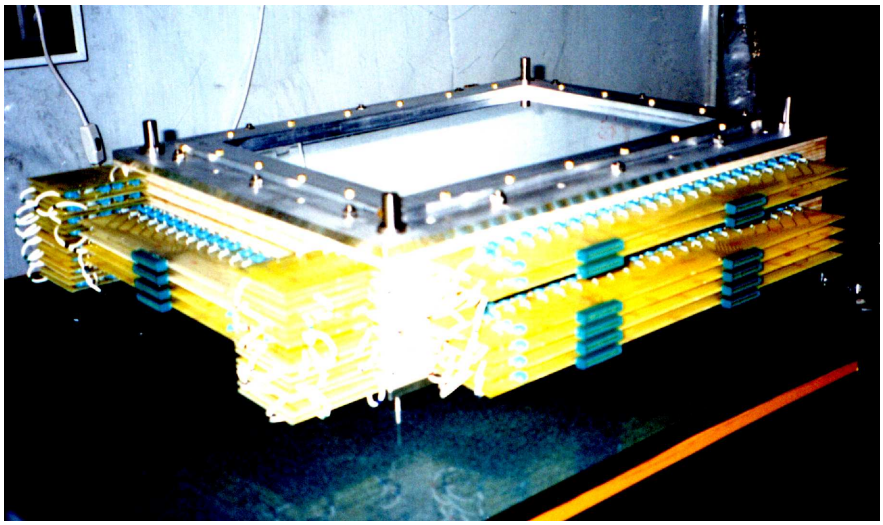

Figure 3.5: Single module of the T3 detector.

the inner dimensions (active area) are 31 cm × 41 cm. The T4 and T5 detectors are larger and their outer frame dimensions are 54 cm × 69 cm and the inner dimensions are 36 cm × 51 cm.

The drift cell measures the time-of-flight of ionization electrons from the position of the detected particle track to the nearest anode wire. The drift chamber which consists only of one detection plane of drift cells measures hit positions along one coordinate (e.g. the x-plane, whose wires are vertical, measures distance along the horizontal x-axis between a hit and some reference point). In order to determine hit positions in two dimensions, at least three detection planes with different anode wire angles (different "views") must be used which is illustrated in Fig. 3.4.

The minimal thickness of the drift cell is limited by the possible hit losses caused by the statistical fluctuations in the electron collection process. The chosen cell thickness of 10 mm provides an average of 20 primary ionizations for minimum ionizing particles. The distance between the field shaping wires of 2 mm was chosen for this cell thickness.

The gas mixture used in all three drift chambers is 75% Ar, 25% C_4H_{10} and 2% ethyl alcohol. The track position determination accuracy of about 100 μm is achieved for T3, T4 and T5 chambers. Fig. 3.5 and 3.6 show photographs of single module of T4 detector and complete T3 detector assembled with front-end electronics in the BRAHMS experiment hall.

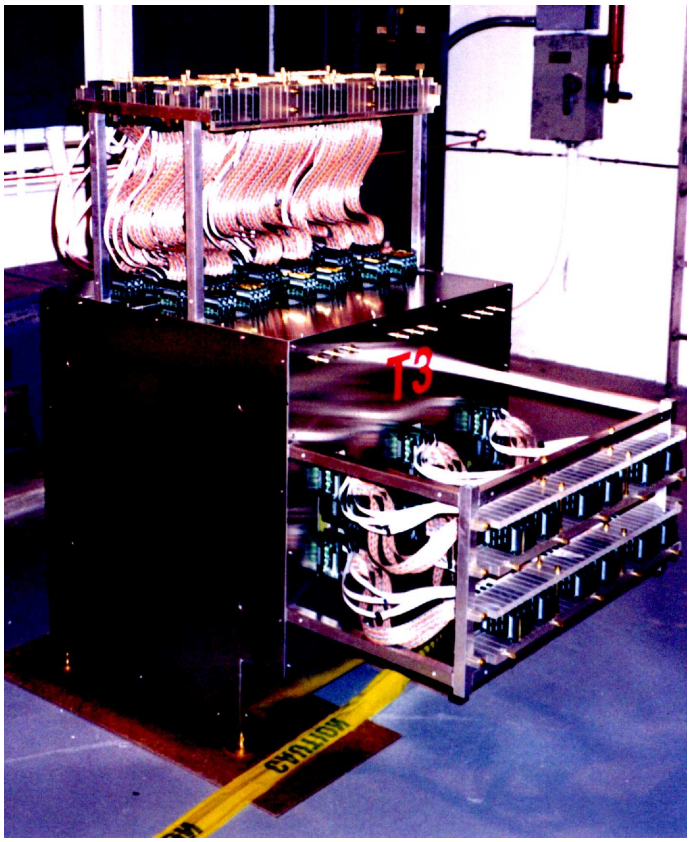

Figure 3.6: The photo of the drift chamber T3 with complete setup of front-end electronics read-out boards.

One of the important experimental issues is determination of the track reconstruction efficiency. The total reconstruction efficiency in Forward Spectrometer is based on the estimation of efficiencies of individual tracking detectors: T1, T2 in the front arm and T3, T4 and T5 in the back part. Because the forward arm is built from five tracking detectors one can construct the reference track for particular detector using the four left chambers which ensures that the reference track is not correlated with tracks in the probed chamber. The definition of reference track represents particle that passed through the tested detector. The efficiency of the detector can be expressed as follows:

$$T_i = \frac{N_{local}}{N_{reference}} \qquad\qquad i = 1, 2, 3, 4, 5. \tag{3.1}$$

where:

$N_{reference}$ - number of reference tracks, N_{local} - number of reference tracks that match, in the given event, to any of the local track. By definition $N_{local} \leq N_{reference} \rightarrow T_i \leq 1$.

The definitions of the reference track for studied tracking chamber is

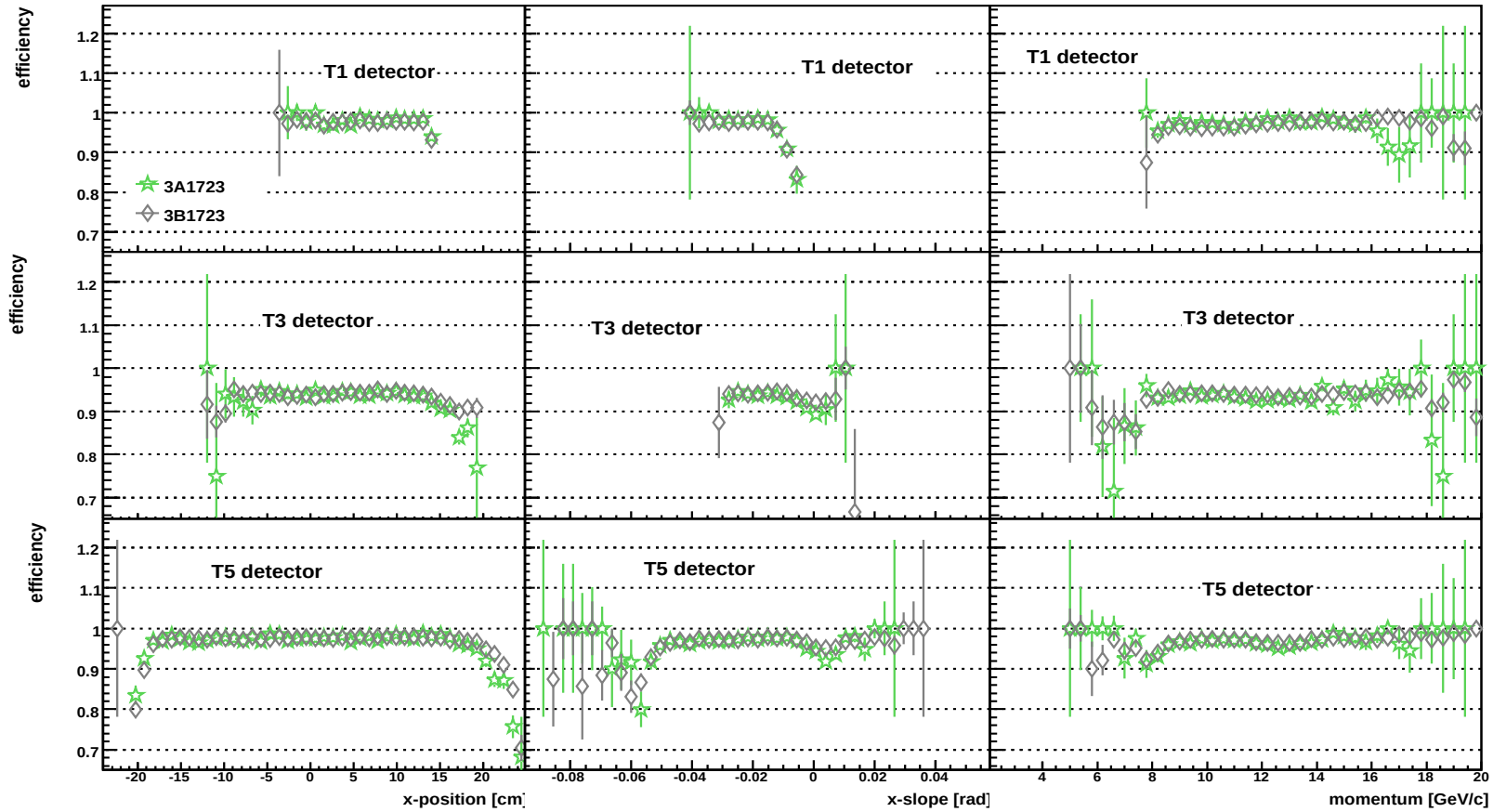

Figure 3.7: The efficiency of the tracking detectors: T1, T3, T5 as a function of x position (upper row), track x-slope (middle row) and momentum (bottom row). The results are shown for p+p collisions at $\sqrt{s}$ = 62.4 GeV, settings: 3A1723 (green stars) and 3B1723 (grey rhombuses).

given below:

1. *T1 and T2 detectors*: the reference track is determined by tracks in T3, T4 and T5 drift chambers; the extrapolated track has matched to the collision vertex

2. *T3 detector* (located between T2 and T4 chambers): the reference track is defined by the T1, T2, T4 and T5 detectors

3. *T4 detector*: the reference track is constructed from the local tracks in T1 and T2 swimmed forward to the back of spectrometer; in addition the extrapolated track should match to any of the local tracks in T5 detector

4. *T5 detector*: the reference track is defined by T1, T2, T3 and T4 detectors, although the transported track must be swimmed forward through the D3 and D4 dipole magnets and match to any of hits in H2 detector.

In Fig. 3.7 the derived efficiencies of T1, T3 and T5 detector are presented vs. x position in the detector, track slope in x direction and track momentum. The total track reconstruction efficiency in FS is taken as a product of all individual chambers efficiencies used in the reconstruction. The detailed description of procedure used to determine the efficiency can be found in [70, 71].

3.2.3 Time of Flight detectors

In BRAHMS experiment the Time of Flight detectors deliver particle identification in the low and intermediate momentum ranges.

The ToF devices are made up of the perpendicular plastic scintillator slats. The position of the TOFW is 4.3 m from the nominal vertex collision and it was built up from 125 slats. The H1 and H2 are placed 8.6 m and 18.9 m from the nominal vertex and contain 40 and 32 slats, respectively. Each scintillator slat is equipped with two photomultipliers (PMTs) as the read-out appliance. Therefore, the electrical signal, obtained from one photomutliplier, is provided through discriminators where in the meanwhile it is generated as the timing signal, delayed and guided to the CAMAC TDC. Concurrently, the signal from the second end of PMT is also delayed during routing to the FATSBUS ADC. The ToF measurements are triggered by the Beam-Beam counters (see section 3.2.5) which are also used to determine the collision vertex. The accuracy of the PID is based on the timing resolution of the separate slats, resolution of the BB counters used as start detectors

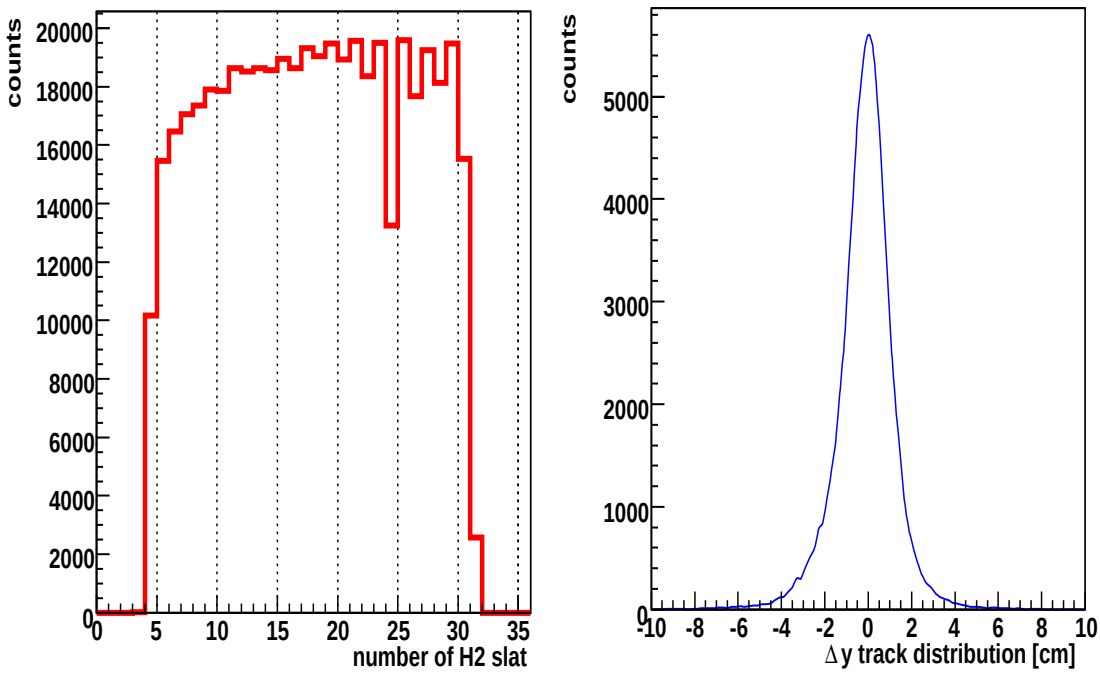

Figure 3.8: The number of counts of the hits registered in the particular slats in H2 Time of Flight detector is displayed (on the left side). On the right, the y resolution of the track position between y position of H2 hit and extrapolated FS track up to H2 detector plane is presented. The results are for p+p collisions at $\sqrt{s} = 62.4$ GeV.

as well as the accuracy of determination of the particle path length and collision vertex.

Calibration of the timming signal is done using the assumption that, after counting a large number of events, the largest peak in the time spectrum is related to pion flying with the speed of light, $\beta = 1$. The effective resolution of ToF detectors is estimated to be 100 ps within good separation of K/π at $p = 9$ GeV/c in FS spectrometer.

In the Fig. 3.8 the left-side plot illustrates which of the H2 slats worked properly during data taking in 2006. The right panel of Fig. 3.8 presents distribution of difference between y location of FS tracks projection in H2 detector plane and y location of H2 hit.

3.2.4 Cherenkov detector

The Ring Imaging Cherenkov detector is located at ≈ 20 m from the nominal vertex point at the end of the back part of the Forward Spectrometer.

RICH detector measurements deliver high momentum particle identifica-

tion. RICH gives the possibility to separate pions and kaons up to momentum of 25 GeV/c and kaons and protons up to 40 GeV/c.

The fundamental part of the Cherenkov detector is gas radiator that has length of 150 cm and in this case is filled with the mixture of C_4F_{10} and the C_5F_{12} at the pressure of the 1.25 atm (details can be found in [72]). The refraction index is n - 1 = 1700 $\times 10^{-6}$. Inside the gas mixture there is placed the spherical mirror with radius of 3 m. The photomultipliers compose an array of 80 devices on the focal plane of the mirror.

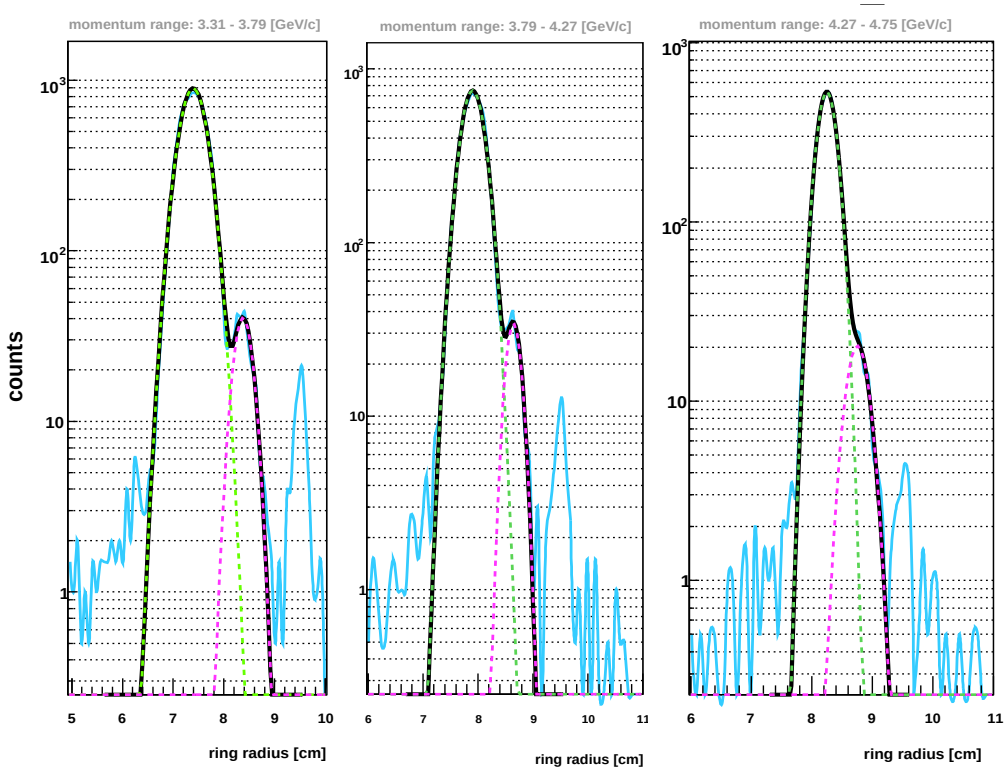

Figure 3.9: Particles distributions of RICH ring radius (blue solid line). The plotted lines represent the Gaussian fit to muons (magenta dashed line) and pions (green dashed line) distributions. The black solid line marks the sum of Gaussian functions used in the PID analysis. The data are displayed for Au+Au collisions at $\sqrt{s_{NN}}$ = 200 GeV, setting: 10B430.

The expected number of photon measured by PMTs and originating from the path length of the gas radiator was estimated in the following: $N_{detected} = N_0 L \sin^2\theta$ where N_0 is closely related to the parameters of the RICH detector and equals 137.5 cm^{-1}. In the photo-detector the ring is created with radius of each particle with velocity greater than the speed of light. For more than one track in detector we choose the track with the largest momentum and define the nominal center of the ring. Then, the length between the pixel center and the estimated ring center is

calculated for all signals and averaged.

The particle identification is based on the fitting the multi-Gaussian function to the particles distribution. The center of the single Gaussian fit should be equal the value of squared invariant mass for a given particle type. We determine the bounds of PID and we find that the $\pm$ 3 σ_{m^2} cut is the most appropriate. In that way we receive electron, muon, pion, kaon and proton bounds. In the region where the bounds overlap it is difficult to distinguish muons and pions, pions and kaons or kaons and protons (p $\approx$ 2.3 GeV/c, p $\approx$ 25 GeV/c and p $\approx$ 35 GeV/c, respectively). The PID is associated according to the probability distribution determined by the Gaussian fit. In Fig. 3.9 the example of the Gauss fit overlapping is shown - for muons and pions - in the momentum range: 3.31 GeV/c $< p <$ 4.75 GeV/c.

3.2.5 Global detectors

The global detectors: Beam-Beam counters (BBc's), Zero-Degree Calorimeters (ZDCs), Multiplicity Array (MA), are assigned to characterize the initial value of charged particle multiplicity and the global collision features like location of the collision vertex. Measurements by ZDCs deliver information about the number of spectators.

The Multiplicity Array is a typical barrel shape detector situated around the nominal vertex. It is made up of Si strips inside the cask and external scintillator elements. It allows to measure the particle multiplicity by registering the energy loss of charged particles which pass through the pads. The multiplicity is estimated from the deposited energy for individual particle that can be left in the single element divided by total energy recorded in that element (GEANT simulations).

The distance of the Si pads from the collision nominal vertex is 5.3 cm, for the scintillator tiles - 13.9 cm. Both silicon and scintillator planes are formed into hexagonal, coaxial to the beam axis, shape segmented into pads, hung on the aluminum construction. The inner and outer parts of the array are complementary, however the intrinsic detector is favoured because of the greater segmentation (42 slices) that allows to set the polar angle with better precision. The correction due to the secondary interactions equals 6-30% whereas the scintillator tiles are needed to be corrected by a factor of 20-40%. Nevertheless, the setup of the scintillator tiles is used as the first level trigger in BRAHMS experiment.

The coverage of pseudorapidity range of Multiplicity Array is $|\eta| < 2.2$.

The Beam-Beam counters are used to determine the time zero signal of the interaction that can be easily translated into calculation of the primary vertex collision. The left BB array has 44 modules (36 small and 8 big tubes) and the right one consists of the 30 small and 5 big tubes. In case of BBc's, the accuracy of the measurement is better than 1.6 cm. The BB arrays are used as zero level trigger and deliver start time signal for ToF detectors. The typical Cherenkov detectors are consisted of BB arrays which are situated on the opposite sides of the nominal interaction point at the distance of the 220 cm. Fulfilling the condition of the zero level trigger they are dedicated to register particles with $\beta \approx 1$, very close to the beam rapidity regime, so they were designed to "surround" the RHIC's beam pipe. Due to high multiplicity of the particles two kinds of modules differing only in geometrical solid angles are used. Both the small ones and large tube modules are built from a Cherenkov lucite radiator with the photomultiplier at the end. The choice of the radiator was driven by the possible selection between particles which enter the front surface at large angles and that ones which give the reduced signal from the side or back.

With the assumption that the velocity of the detected particles is $\beta = 1$, the position of the collision vertex can be calculated:

$$z_{vertex} = \frac{c}{2}(t_{left} - t_{right}) \tag{3.2}$$

where:

c - the speed of light, t_{left} (t_{right}) - the flight time to the left (right) detector.

The Beam-Beam counters can measure the particles in the pseudorapidity range: $3.1 < |\eta| < 3.6$.

The Zero-Degree Calorimeters are the same for all four experiments at RHIC [73]. One of the most important measurement is to estimate the luminosity as well as setting the time difference between two ZDCs to evaluate the impact parameter of the event. The preliminary selection based on the amplitude and difference in time of the signals from different modules allows to reject some of the background events.

During the reaction the high energetic neutrons, which do not participate in the collision, usually evaporate from the nuclei surface and can be easily registered in the area close to the beam fragmentation region. Putting the detectors in that regime enables to measure spectator neutrons and then takes the opportunity to set the minimum bias events, the luminosity or the centrality of the collision. The calorimeters are located on the both sides of the collision point 36 meters away

from each other. The calorimeter is made up from the tungsten as the absorber and uses quartz optical fibers to register particles which produce the Cherenkov light. One detector is composed of three modules. Such construction allows to determine whether the particle hits from the front or back side of the calorimeter. ZDcs provide supplementary information of collision vertex. The time resolution achieved in detector is 170 ps.

Chapter 4

Data Analysis

This thesis presents the comparison of pion and proton yields as a function of p_T for some η intervals. Nominally, the BRAHMS setup can measure produced particles up to $\eta = 4$. The analysis utilizes the feature of the same π and p acceptance in the η vs. p_T space. For a given $\eta - p_T$ bin the $p/\pi(p_T)$ ratio is calculated on setting by setting basis. The ratios are calculated separately for the ToF PID and RICH PID, so all factors such as geometrical acceptance corrections, tracking efficiencies, trigger normalization cancel out in the ratio. The only remaining corrections related to the specie of particle are PID efficiency and particles decays within interactions with the material budget correction.

The presented results are shown for large value of pseudorapidity which implies that the following analysis touches on the data registered using the Forward Spectrometer in the BRAHMS detector setup.

The scope of the studying numbers of runs for particular settings for each colliding system and energy is listed in **Appendix 2**.

4.1 Data reconstruction

The data reconstruction is based on C++ framework developed in BRAHMS Collaboration called BRahms Analysis Toolkit (BRAT). The reconstruction is processed in three steps:

1. local tracking (ltr) - reconstruction of track segments in individual detectors
2. global tracking (gtr) - global tracks are constructed from local tracks and track segments with putting the attention on proper description of tracking devices geometry

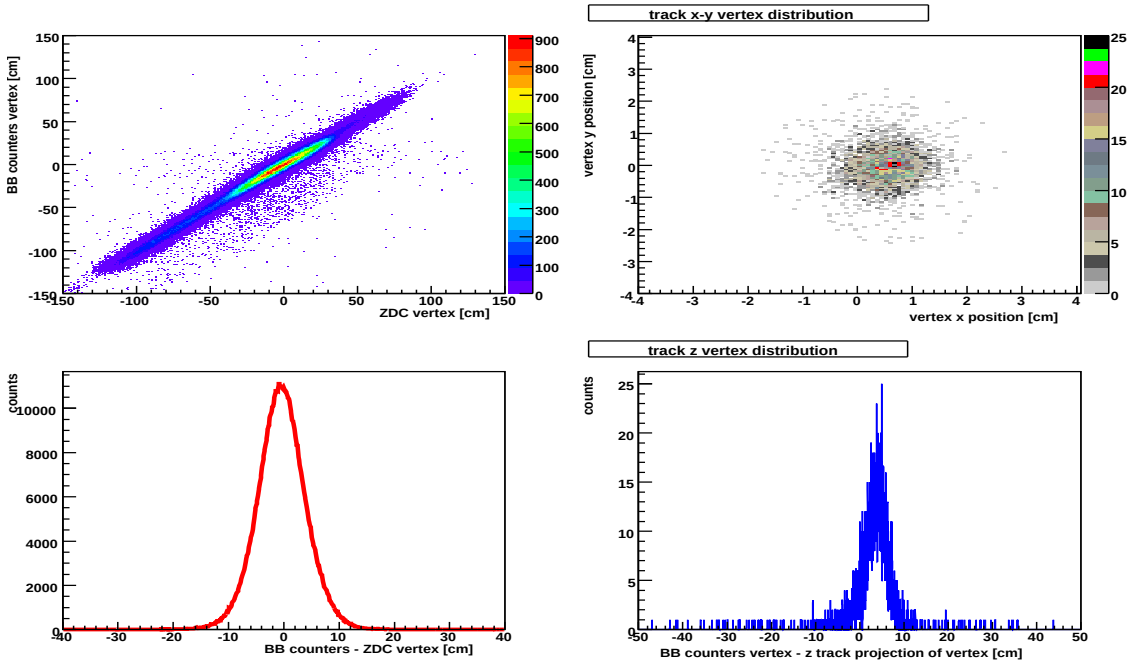

Figure 4.1: The ZDCs and BBc's layout (left column). On the right-top the $x-y$ map received from the Beam-Beam counters is displayed. The right-bottom plot shows the difference between the vertex determination from the BBc's and extrapolation of the reconstructed track in FS. The analysis refers to Au+Au collisions at $\sqrt{s_{NN}}$ = 62.4 GeV, setting: 8A1219.

3. Data Summary Tape (dst) - at the "ltr" and "gtr" level the information is stored for individual detectors separately; at dst level the association of global tracks with matched information from PID detectors is performed; pieces of information are organized in the form of global storage with detailed track by track information.

At each step the reconstructed data are recorded on disk and used as an input in the subsequent step.

The data reconstruction is performed up to dst level according to the official collaboration procedure and are the "foreword" to the specific physics analysis. The below paragraphs aim at description of global characterization of the collision as well as local and global particle tracking in BRAHMS Forward Spectrometer.

Global parameters of collision

The essential event characterization is, firstly, the determination of vertex position of the reaction, as well as the collision centrality. As it was depicted in the

previous chapter, ZDCs and BB counters allow to determine the interaction point. In Fig. 4.1 one can see the correlation between ZDCs and BBc's vertex position in z direction - left column. The efficiency of collision event detection of ZDCs is almost 100% and the ZDC devices are used to determine the vertex position for minimum bias events. Almost 100% efficiency of vertex position determination for the central interactions allows to use BB counters as the base. However it is not so effective for peripheral collisions, $\approx 40\%$, for which usually the ZDCs measurements are applied. The determination of the vertex is estimated in the same manner for ZDCs and BB counters using the difference in time of particles flight measured by left and right devices according to the (3.2) formula. If collision occurs the detectors measure the two flight times of which coincidence is estimated every time to check if the signals originate from the same collision. The vertex resolution is established on the basis of timing resolution measurements. It is important to precisely set the vertex location because the multiplicity distribution done by Multiplicity Array depends on that value. The present vertex resolution for BB counters is 0.9 cm, for ZDCs - 2.0 cm.

Charged particle multiplicity is a continuous function used to determine the collision centrality. Applying minimum biased trigger we can associate full range of multiplicity distribution with total Au+Au interaction cross section. To set the centrality of the collision we use the correlation that if the more central collision happens the higher value of event multiplicity is observed. In BRAHMS setup the centrality estimation is based on the Multiplicity Array measurements averaging the registered hits from the silicon and scintillator pads [76]. From correctly calibrated measurements we should get the symmetric distribution which, additionally, can be compared with the GEANT simulations to exclude the possible misleading information. The GEANT calculations are also applied to conclude the correspondence between the centrality selection and real impact parameter of the collision. The charged multiplicity, defined using BB counters, is essential in the centrality determination for wide range of pseudorapidity. Because the acceptance of the BB counters is much better, even for wide range interval of vertex, for the most forward rapidities the centrality is determined using Cherenkov detectors. Applying the charged particle multiplicity distribution the centrality intervals are delimited.

The multiplicity of an event used for the vertex and centrality determination is evaluated from the Multiplicity Array and BB counters. By registering the energy loss of charged particle passing through the detector elements we can establish the multiplicity distribution by summing the multiplicity from each element. The counted event multiplicity distribution are corrected for acceptance which depends on vertex location - the details of the multiplicity analysis can be found in

[76].

Local tracking

The local tracking is done using the official BRAHMS "offline" algorithms for particle tracking. The software is used to convert raw data into hits. The Forward Spectrometer algorithms are made for T1, T2, T3, T4 and T5 chambers. Plausibly, hits deliver details about a position in the coordinate system throughout the amplitude and drift time information. In case of TPCs we can get the 3-dimensional information about hit position. In turn, we mix readout information from the three detection planes in the drift chambers to get the full 3-dimensional point position. Before the local tracking algorithms are applied, the calibration must be done. The calibration process includes: specification which of the pads in TPCs (cells in DCs) worked improperly, correcting the non-linearities of time measurements, excluding the drift velocity fluctuations with time.

The local tracking procedure takes following steps:

- the raw data arranged firstly in the sequences which next are assembled into clusters
- it might happen that the newly resultant clusters can overlap, so at first the deconvolution of these clusters is done; therefore the deconvolution of clusters into hits is applied getting well-defined space position, its variance and cluster ADC sum (or energy loss)
- the hits are grouped and fitted to get 3-dimensional line.

In the tracking procedure the background particles must be taken into account. To ensure that the tracks come from "true" events the tracks in the neighboring detectors are extrapolated to the chamber and next projecting in the particular detector. Around the projected track a small tube is created that allows to avoid left-right ambiguity of the hits. Note that this projected tracks is not necessary consistent with the real particle track. The algorithm used to assign the tracks is based on choosing the hits in the tube estimating distances between the projected tracks and the hits. The distances are counted in x and y direction as well in the x- and y-slope of the track. The hits are accepted with 3σ range. Additionally, the following requirements must be fulfilled to approve the event: the amount of approved hits which is equivalent to the number of accepted hits in the tube, number

of views with the hit, the amount of approved hits per view. All steps of the procedure guarantee the accuracy of the reconstructed track.

Global tracking

In global tracking procedure the local tracks should be matched through the dipole magnets. The track curvature inside the magnet attend to determine the momentum using the formula:

$$p = \frac{Bl}{(\sin\phi_b - \sin\phi_f)\sqrt{1-\alpha_y^2}} \tag{4.1}$$

where:
B - magnitude of vertical magnetic field, l - magnet length, ϕ_b - the angle between the tangent line of the curvature and z axis measured in front of the magnet,ϕ_f - the angle between the tangent line of the curvature and z axis measured in back of the magnet, α_y - the averaged vertical slope of the tracks.

At the very beginning we register hits which are detected in the chambers and from which the lines of the tracks in the detector are restored. Afterwards, matching the local tracks allows us to reconstruct the full tracks of the particles that run across the forward arm (global tracking). The tracks reconstructed in the chambers constitute of the front and back tracks of the dipole magnets through which the matching procedure is applied. In the matching algorithm three parameters are used: the difference of the angles related to the ϕ_b and ϕ_f, the vertical slope α_y, the quantity of the intersection of front and back tracks with the matching plane Δy. Without the imperfections of the experimental setup and reconstructing procedure the parameters should be equal 0. During matching, at first step the Gauss fit is used, therefore the elliptic cuts. In the FS the tracks are grouped into Back-Forward-Spectrometer (BFS) and Front-Forward-Spectrometer (FFS) tracks to avoid "ghost" tracking. The first group contains tracks reconstructed using matching between D3 and D4 (T2/T3-D3-T4 and T4-D4-T5 combination). To estimate the FS tracks the second one is required to match with reconstructed BFS tracks. It is done in two ways: using geometrical matching algorithm (in case of T3-D3-T4 combination) or matched tracks between T1 and T2 detector (for T2-D3-T4). Eventually, the full FS tracks are reconstructed with the minimizing of false combination.

Additionally, in the spectrometer, the tracks are extrapolated to the vertex area and matched to its position determined by the BB counters. It is worth

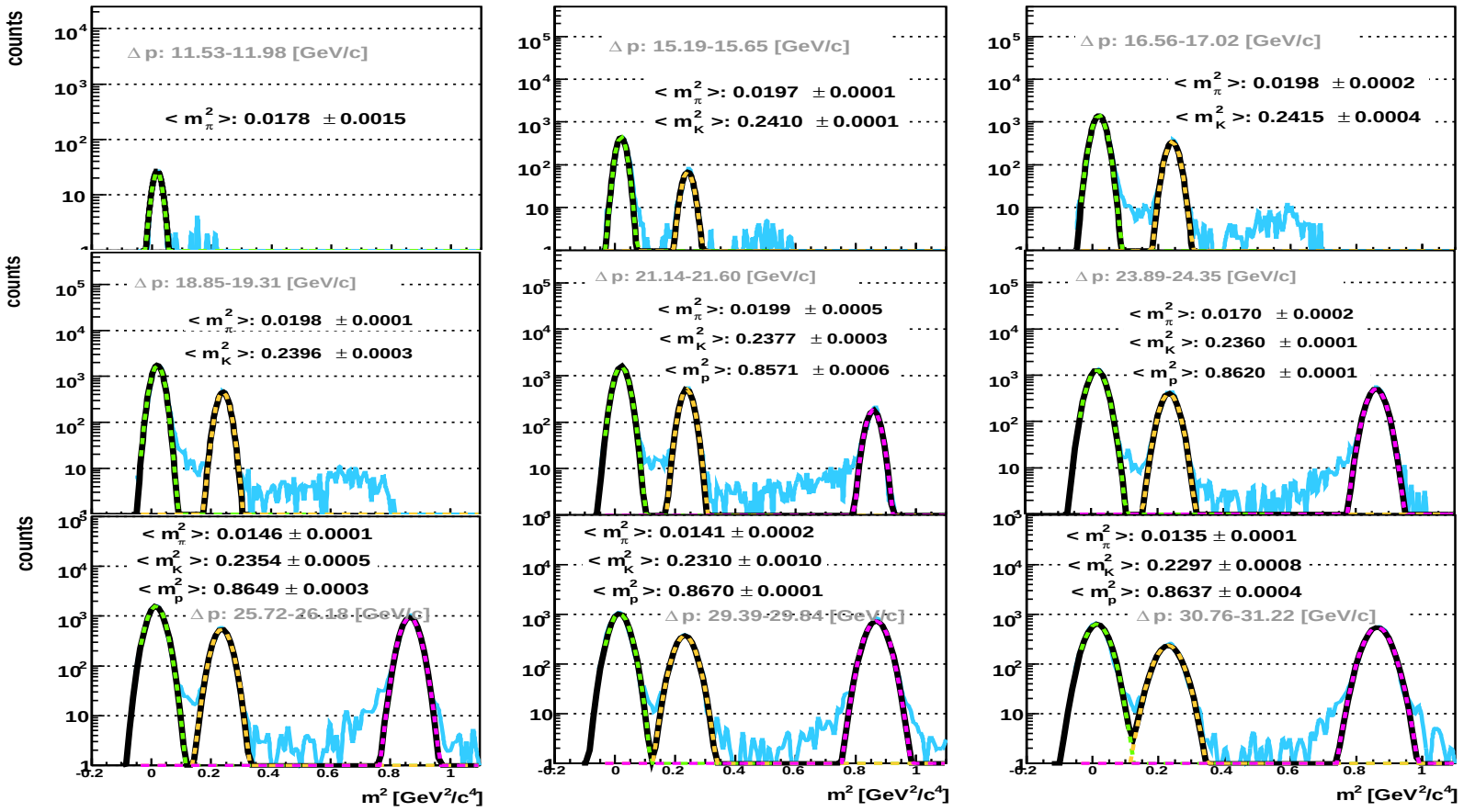

Figure 4.2: The PID procedure is based on fitting of multi-Gaussian distribution to separate the particular specie of particles ($e^{-/+}$, $\mu^{-/+}$, $\pi^{-/+}$, $K^{-/+}$, $p/\bar{p}$). Here, the series of histograms including lines representing fits with multi-Gaussian function (black solid line) are displayed for Au+Au reactions at $\sqrt{s_{NN}}$ = 200 GeV, setting: 4B2442. The Gaussian function for pions is marked with dashed green line, for kaons - dashed orange line, for protons - dashed pink line. The blue line represents experimental data. The mean of squared invariant masses, $<m_X^2>$ (X = e, μ, π, K, p), are displayed for indicated momentum ranges (Δp).

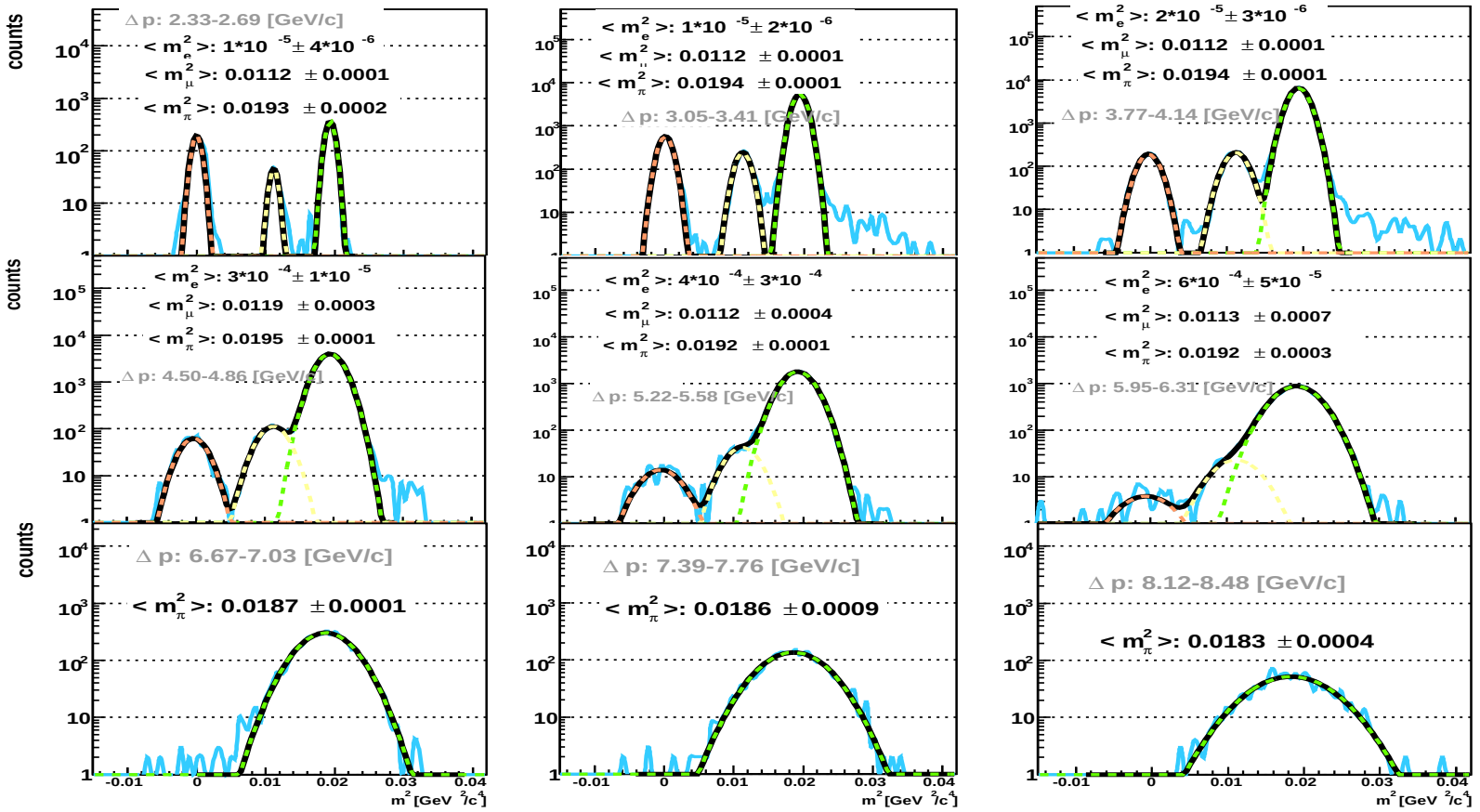

Figure 4.3: The same as Fig. 4.2, but obtained for the p+p collisions at $\sqrt{s} = 62.4$ GeV, setting: 4A608. The Gaussian function for electrons is depicted with dashed red line, for muons - dashed yellow line, for pions - dashed green line. The overlapping of muons and pions for $p > 4$ GeV/c is clearly visible.

pointing out that this method let us not only control the vertex parameters, but also check if the track originates from the nucleus-nucleus reactions or from other sources. The $x-y$ vertex distribution achieved from the extrapolated tracks positions is displayed in the Fig. 4.1 on the right-top panel. Moreover, on the right-bottom plot the difference between BB counters and track vertex determination is shown.

Further steps of analysis

Obviously, to ensure the appropriate tracks reconstruction and cohesion of the particle tracking the additional requirements are applied in the Forward Spectrometer analysis:

1. The fiducial cut on D1 in x dimension is checked for every track.
2. Because of the Time of Flight measurements (for Au+Au collisions defined as "Trigger 2") the hits in left and right tubes of BB counters are required for every track in the analysis. Additional restrictions determining the triggers condition are listed in the **Appendix 2**.
3. The cut on χ^2 evaluated from the GEANT simulations is imposed on each track. The value of cut is calculated from the equation $\chi^2_{cut} = A + \frac{B}{p}$ (p - momentum of the particle).
4. The following collision vertex range is taken into account:
   (a) Au + Au at $\sqrt{s_{NN}}$ = 200 GeV $\rightarrow z \in$ (-40 cm - 40 cm)
   (b) Au + Au at $\sqrt{s_{NN}}$ = 62.4 GeV $\rightarrow z \in$ (-60 cm - 40 cm)
   (c) p + p at $\sqrt{s}$ = 200 GeV $\rightarrow z \in$ (-50 cm - 50 cm)
   (d) p + p at $\sqrt{s}$ = 62.4 GeV $\rightarrow z \in$ (-50 cm - 50 cm).

The restriction which is additionally introduced to ensure the appropriate H2 and RICH efficiencies in particle identification is defined by the imposed fiducial cuts in x and y direction in RICH detector: $x \in$ (-21 cm - 21 cm) and $y \in$ (-15 cm - 16 cm).

4.2 Particle identification

Particle identification in the Forward Spectrometer depends on the data taken using the H2 Time of Flight detector and the Ring Imaging Cherenkov

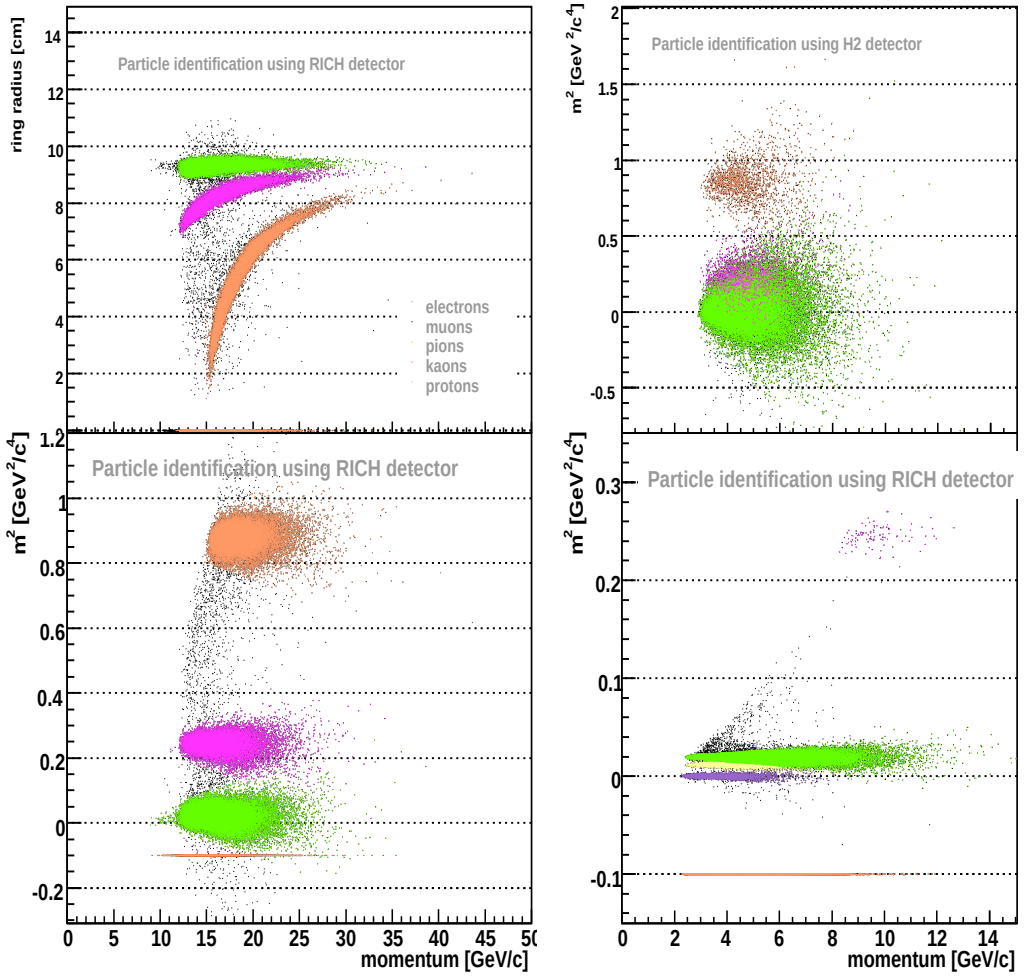

Figure 4.4: The results of PID analysis in case of using H2 and RICH detector for low (608 [A]) and high (2442 [A]) magnetic field in the D1 magnet of Forward Spectrometer. Electrons are highlighted with the violet points, muons - yellow points, pions - green points, kaons - pink points and protons - orange points. In the left column the results for Au+Au collisions at $\sqrt{s_{NN}}$ = 200 GeV are depicted (setting: 4B2442). The left-top figure shows the identified species momentum dependent cuts applied on ring radius vs. particle momentum map. The left-bottom picture displays the identified pions, kaons and protons applying the squared invariant mass, m^2, vs. particle momentum map. In the right column the figures present the outcome of PID procedure (H2 PID - top panel, RICH PID - bottom panel) for low magnetic field (setting: 4A608) for elementary collisions at $\sqrt{s}$ = 62.4 GeV. In the bottom row the veto antiprotons are marked with the orange points at m^2 = - 0.1 GeV^2/c^4.

detector. The H2 data are used to identify particles with lower momenta: $p < 9$ GeV/c (see right-top plot in Fig. 4.4). For higher momenta hadrons the RICH detector is used.

Generally, in both cases - H2 and RICH detector measurements - the PID procedure is done for small momentum bins by fitting multi-Gaussian function into the squared invariant mass m^2 distribution and applying the $\pm\ 3\sigma_{m^2}$ cuts to select a given particle type. In case of H2 PID, below kaon Cherenkov threshold , $p < 9$ GeV/c, a veto is imposed on RICH detector to separate kaons - in the range of m^2 where they overlap with pions ($p > 3.5$ GeV/c). Thus, we receive a pion sample with a slight contamination of kaons which have miss-identified rings associated in Cherenkov detector. The example of the results of pions (green points) and kaons (pink points) separation is displayed in the right-top plot on Fig. 4.4.

The RICH identification procedure is used for muons, pions, kaons and "clear" sample of protons above proton Cherenkov momentum threshold, $p > 15$ GeV/c. In most cases, the particles are enough energetic to create Cherenkov radiation in the detector. The ring is registered in the detector which allows to recognize the specie of particle according to the recorded ring radius. In the range, 9 GeV/c $< p <$ 15 GeV/c, the additional proton identification must be applied. Sometimes it might happen that the tracks are registered, but the rings are not formed. This criterion is fulfilled by protons and kaons (in a lesser degree) and, customarily, they are called veto particles. In the RICH PID procedure, RICH inefficiency correction is estimated to correct the veto proton yield. The RICH inefficiency correction procedure is described in the next section.

Eventually, the results of fit with the multi-Gaussian function used in the PID procedure is shown in the Fig. 4.2 (Au+Au at $\sqrt{s_{NN}} = 200$ GeV) and 4.3 (p+p at $\sqrt{s} = 62.4$ GeV). The averaged values of squared invariant mass, $<m_X^2>$, are depicted for particular momentum bins. As one can see the pions, kaons and protons can be clearly separated. In Fig. 4.3 the PID processing of e^-, μ^-, π^- are presented for different momentum gaps. The e^- can be well separated from μ^- and π^-. The overlapping of muons and pions can be noticed. In general, in the region where the m^2 distributions overlap, the PID is associated according to the probability distribution determined by the Gaussian fit. In case of muons and pions at $p \geq 4$ GeV/c majority of muons comes from π decays, so the muons are associated with pion yield. In Fig. 4.5 the outcome of the particle identification procedure is displayed for heavy ions collisions in left column and on right for p+p reactions.

4.3 Corrections

4.3.1 RICH efficiency

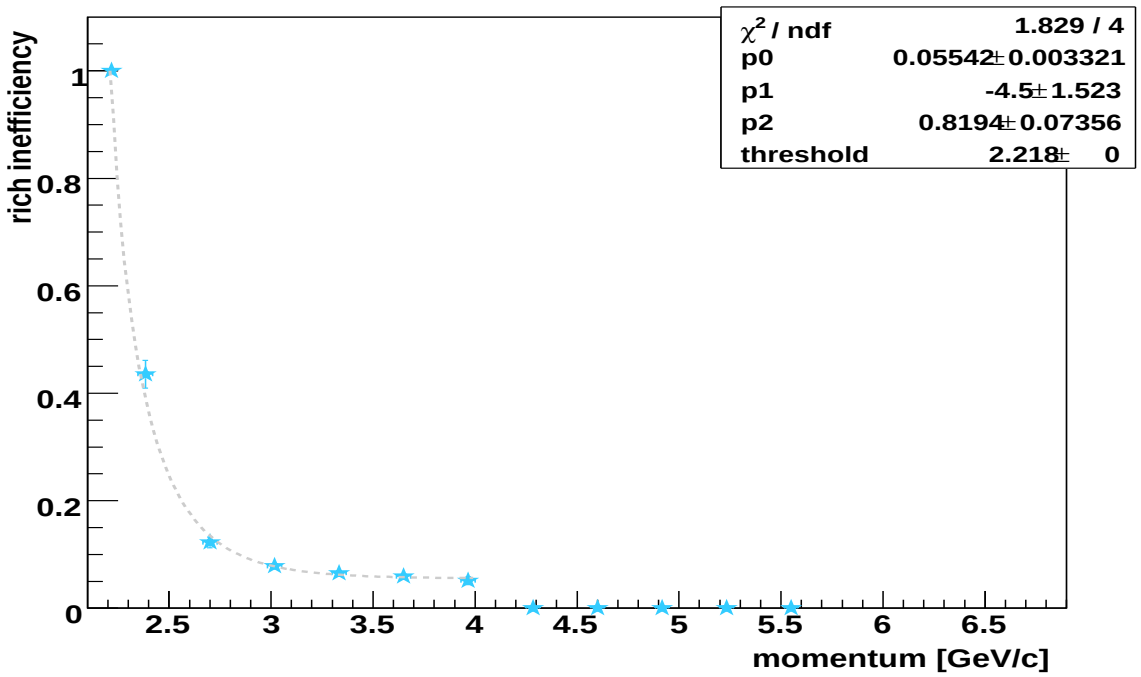

Figure 4.5: The RICH inefficiency correction as a function of momentum and ring radius for Au+Au collisions at $\sqrt{s_{NN}} = 200$ GeV. The function and obtained fitting parameters displayed in the right-hand inset are received in accordance with the equation 4.3.

The idea of evaluating the RICH detector efficiency is mainly based on studying particles contamination in H2 hodoscope. We assume that produced Cherenkov radiation depends only on particle γ factor. The inefficiency of Cherenkov detector (1 - T) is defined as the ratio of pions measured in Time of Flight detector, but without signals in RICH detector that would allow to reconstruct rings (veto pions), to all pions recorded in H2. The RICH efficiency concept is exposed:

$$\frac{\text{pions registered in H2, having no ring in RICH}}{\text{all registered pions in H2}} = 1 - T \qquad (4.2)$$

where:

T - RICH efficiency.

In Fig. 4.5 one can see the dependence of pion inefficiency as a function of momentum for low magnetic field for Au+Au collisions at $\sqrt{s_{NN}} = 200$ GeV. The pion Cherenkov momentum threshold, p_{π}^{th}, is equal 2.22 GeV/c. We describe the value of RICH inefficiency for pions in the given momentum range using function:

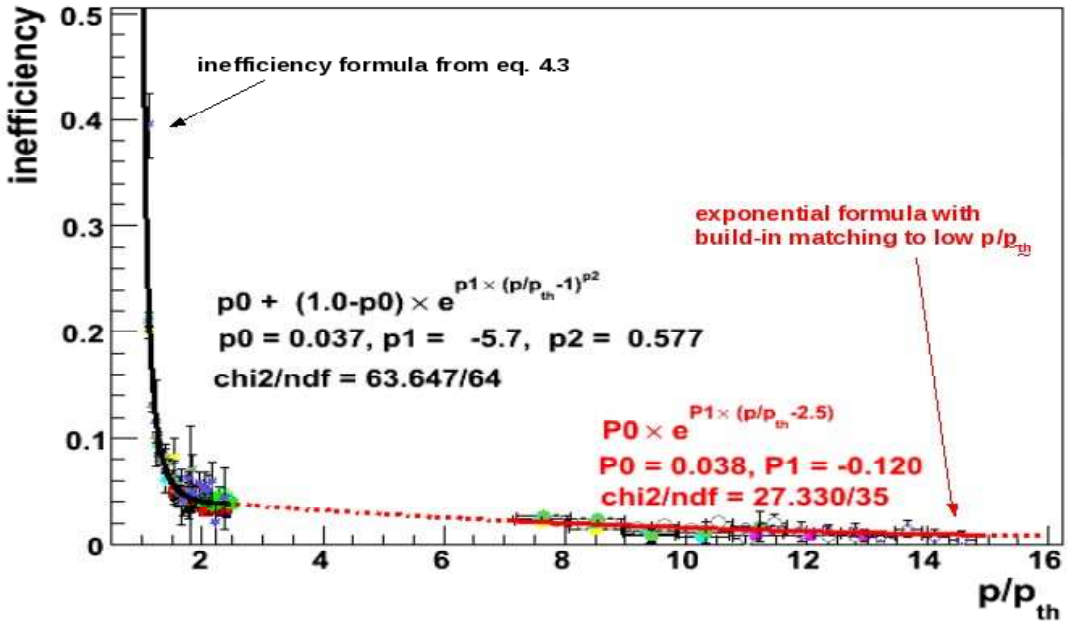

Figure 4.6: The RICH inefficiency correction as a function of p/p_{th} for Au+Au collisions at $\sqrt{s_{NN}} = 200$ GeV for low (black line) and high (red line) magnetic field settings. The picture presents the consistency of applied procedure of RICH inefficiency correction - the points for $p < 3$ GeV/c stands for pions from low magnetic field data and protons from high magnetic field data, the points for $p > 7$ GeV/c - pions from high magnetic field data.

$$\bar{T}(p) \equiv 1 - T(p) = p_0 + (1 - p_0)\exp[p_1(p_\pi - p_\pi^{th})^{p_2}] \tag{4.3}$$

where the momentum is defined as:

$$p = m\gamma\beta. \tag{4.4}$$

Afterwards, we extrapolate the inefficiency to the higher momentum. The relation of momentum between pions and other species (muons, kaons) having the same γ factor is:

$$p_\pi = \frac{m_\pi}{m_x} p_x \qquad \text{x} = \mu, \text{K}. \tag{4.5}$$

On the basis of the assumption that RICH response depends only on particle γ factor, the RICH inefficiency for other species, i.e. muons, kaons, is derived from (4.3) formula by replacing p_π using (4.5) expression.

The yield of veto protons is corrected for pions and kaons contamination. The yield of proton contamination is calculated as follows:

$$y_{proton\_\text{contamination}}(p) = y_\pi(p)\frac{\bar{T}_\pi(p)}{1-\bar{T}_\pi(p)} + y_K(p)\frac{\bar{T}_K(p)}{1-\bar{T}_K(p)} \tag{4.6}$$

where first and second term represent π and K contamination, respectively.

The above procedure can be applied for settings with lower magnetic field where the good pion and kaon separation in H2 detector is achieved ($p < 4$ GeV/c). At pion momentum threshold, $p_\pi^{th} \approx = 2.22$ GeV/c, the inefficiency of RICH detector is $\sim 100\%$ and decreases with larger momentum (see Fig. 4.5). However, the RICH inefficiency does not scale with particle momentum in the whole covered p range - the clear dependence on setting is seen. For settings with the lowest value of magnetic field (430 [A]) the Cherenkov threshold proximity dominates. For higher magnetic field settings the geometrical effects are introduced. It implicates that the best choice of parameter regarding inefficiency dependence is x-slope of track in T5 detector. It is closely related to the geometry of the tracking stations and RICH detector.

In the analysis, it was found that for the high magnetic field settings it is enough to concern only geometrical effect because the particles momenta are much higher than the proton threshold. In this range of p ($p > 18$ GeV/c) we can estimate the inefficiency correction defined as follows:

$$\frac{\text{particles having no ring in RICH}}{\text{all registered particles in RICH}} = 1 - T. \tag{4.7}$$

Moreover, as it was mentioned in the previous chapter, in T5 drift chamber the tracks multiplicity is very low. It allows us to study how the inefficiency changes with the multiplicity of registered tracks in FS (track resolution effect). Fig. 4.6 shows the RICH inefficiency obtained for low and high magnetic field runs. To avoid dependency of particle species the inefficiency is plotted vs. p/p_{th}.

Additional issue is the dependence of value of inefficiency correction on polarity of magnetic field. So, it depends if we measure π^-, K^-, $\bar{p}$ or π^+, K^+, p. It occurs due to lower statistics of the data for negatively charged particles.

Let me summarize how the correction is evaluated. Generally, the three effects are taken into account: particle γ factor, geometrical effect revealed as the T5 track x-slope dependence and two track resolution effect. So, if the partial inefficiencies are small, the RICH inefficiency can be defined as follows:

$$\bar{T} \approx 1 - (1-\bar{T}_\gamma)\text{x}(1-\bar{T}_{\text{T5}\_x-\text{slope}})\text{x}(1-\bar{T}_{\text{track}\_\text{resolution}}) \tag{4.8}$$

where:

$\bar{T}_\gamma$ - the γ factor component, $\bar{T}_{\text{T5}\_x-\text{slope}}$ - the geometrical effect contribution with

the T5 track x-slope dependence, $\bar{T}_{\text{track\_resolution}}$ - two track resolution effect component.

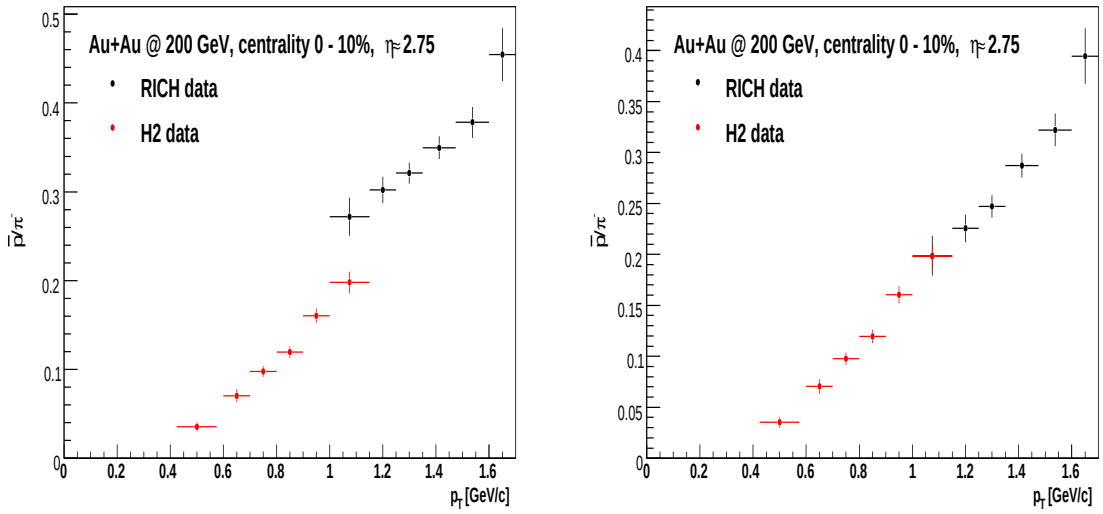

Figure 4.7: The $\bar{p}/\pi^-$ ratio vs. transverse momentum for the most central (0 - 10%) Au+Au collisions at $\sqrt{s_{NN}} = 200$ GeV without (left-hand) and with (right-hand) applied RICH inefficiency correction.

In the analysis it is assumed that all three effects are independent therefore the inefficiency correction is counted as a sum of three components. The inefficiency of RICH detector in case of measuring positive particles is less than 5%, for negative hadrons - $\bar{T} < 3\%$.

The Fig. 4.7 presents the $\bar{p}/\pi^-$ ratio without and with applying RICH efficiency correction.

4.3.2 Absorption and in-flight decays corrections

In the analysis, where the corrections connected with the particle specie are included, implementing the contribution concerning the multiple scattering and in-flight decays is significant. In the Fig. 4.7 the value of $correction^{-1}$ is presented as a function of momentum. The depreciation contribution is observed with increasing p. Moreover, the most significant correction is applied in case of the kaon yield, the smallest one - for pions. Here, the feeddown correction for Λ and $\bar{\Lambda}$ weak decays are not included. The polar angle of produced emitted particles plays an important role of evaluating correction value.

This kind of correction is generated using GEANT package [75]. The GEANT correction studies are based on geometry of BRAHMS experimental setup

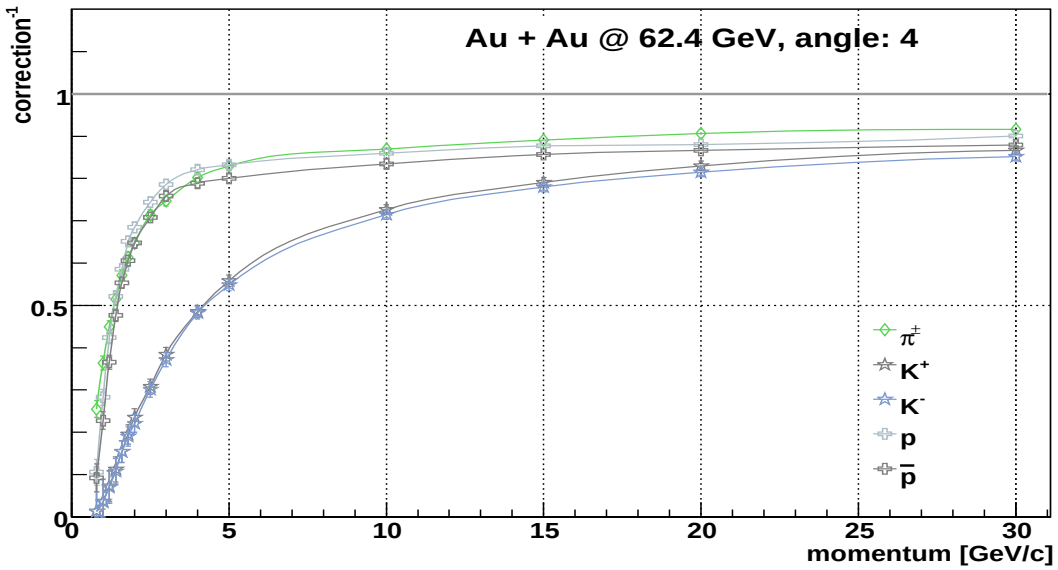

Figure 4.8: Absorption and weak-decays corrections for pions, kaons and protons as a function of momentum obtained by GEANT simulations.

and tracking capabilities. The interactions with detectors or beampipe materials are taken into account. The simulated data are reconstructed in the same manner as real recorded data, i.e. the cut on χ^2. The χ^2 cut comes from the global fit to the tracks in $x-y$ plane for all tracking chambers. Using the dependence of momentum we apply the cut on χ^2. Mostly, the tracks, which are rejected, originate from multiple scattering or decays for pions. Both absorption and in-flight decays corrections are expected to be different for $\mathrm{p}/\bar{\mathrm{p}}$ and $\pi^{+/-}$, thus are relevant in proton-to-pion ratios analysis.

Chapter 5

Results

5.1 P/π ratio in Au+Au collisions at $\sqrt{s_{NN}} = 200$ GeV

In the previous chapter the detailed description of analysis together with applied corrections were presented. The described steps are taken for every setting of Au+Au and p+p system at $\sqrt{s_{NN}} = 62.4$ GeV and 200 GeV. Finally, we obtain the proton-to-pion ratio starting from the $\eta - p_T$ maps of identified hadrons depicted in Fig. 5.1. These are two dimensional plots which show particle yields versus transverse momentum and versus pseudorapidity. In Fig. 5.1 the particular settings are marked with various colours. Subsequently, the $p/\pi(p_T)$ ratios are obtained for narrow pseudorapidity intervals - defined by limits imposed on the attainable pseudorapidity range. At this stage the proton yield is divided by pion yield. We take that corrections for geometrical acceptance and tracking efficiency cancel out in the ratio.

Let me start from calling the published $p/\pi^+(p_T)$ ratio obtained at midrapidity for Au+Au at $\sqrt{s_{NN}} = 200$ GeV ($\mu_B = 26$ MeV) [9] compared with theoretical predictions based on parton recombination model [52] and hydrodynamical description [12] - Fig. 5.2. The characteristic growth at intermediate p_T region, predicted by models, seems to be more consistent with the depiction of recombination model. The hydrodynamic scenario, proposed in [12], describes properly only low transverse momentum data associated for $p_T < 1.8$ (pions) and 3.5 (protons) GeV/c. These results might suggest that at low value of baryo chemical potential the hadronization process is well captured by the coalescence model.

This thesis concentrates on proton and pion production for particles emitting in the forward direction. Using the BRAHMS experiment unique opportunity

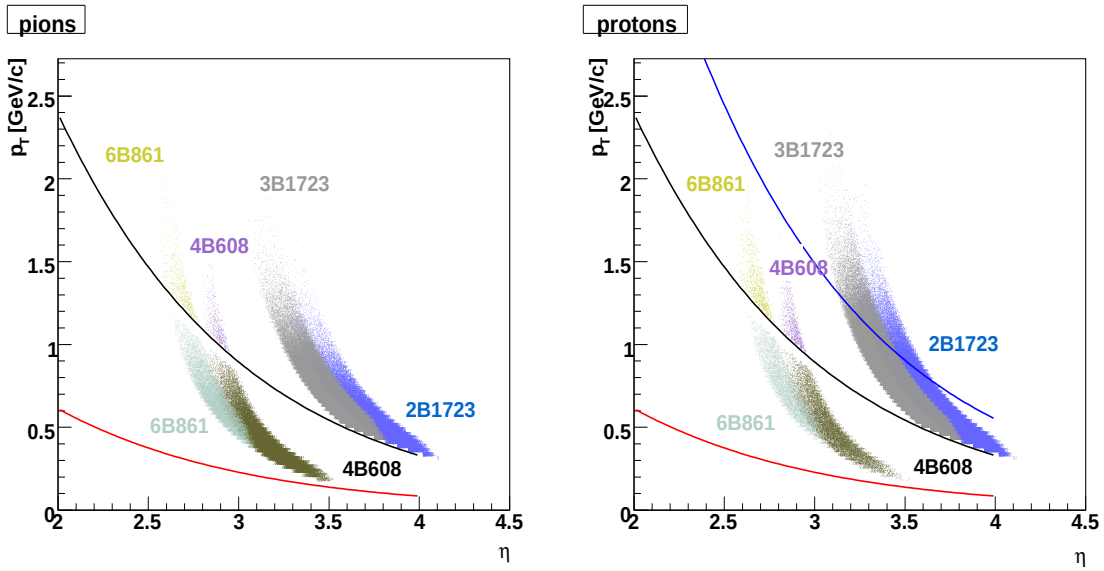

Figure 5.1: $\eta - p_T$ maps for pions (left-hand picture) and protons (right-hand picture) for p+p collisions at $\sqrt{s} = 62.4$ GeV. The plots show the coverage of pseudorapidity and transverse momentum of experimental data. The transverse momentum can be expressed as a function of η: $p_T = p \sin[2 \operatorname{arctgh}[\exp(-\eta)]]$. In the picture the lines represent this function with constant value of momentum: $p = 2.3$, 9 and 15 GeV/c which correspond with the initial value of momentum for ToF (red line), RICH (black line) and veto-RICH PID (blue line) procedure.

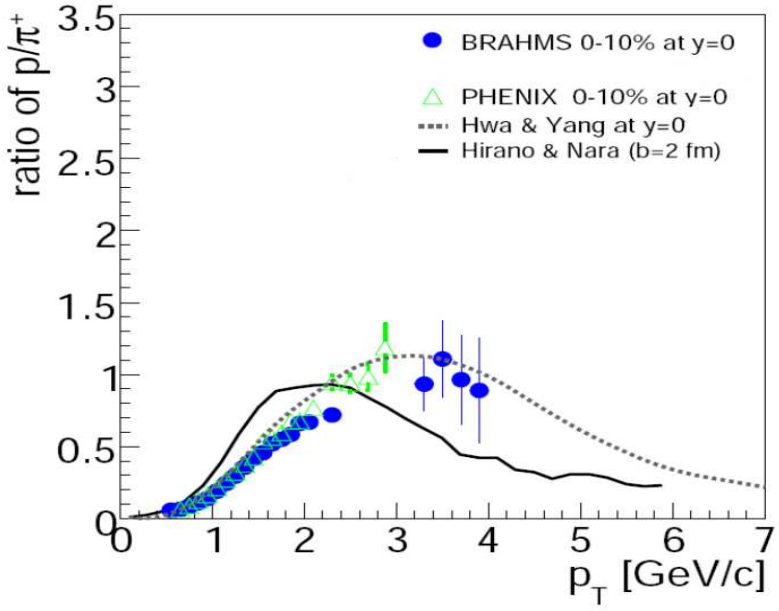

Figure 5.2: Proton-to-pion ratio as a function of p_T for Au+Au reactions at $\sqrt{s_{NN}}$ = 200 GeV for midrapidity regime. The figure is taken from [9]. The PHENIX experiment results are shown in [77]. The recombination model predictions are presented in [53]. The hydrodynamical calculations are included in [78].

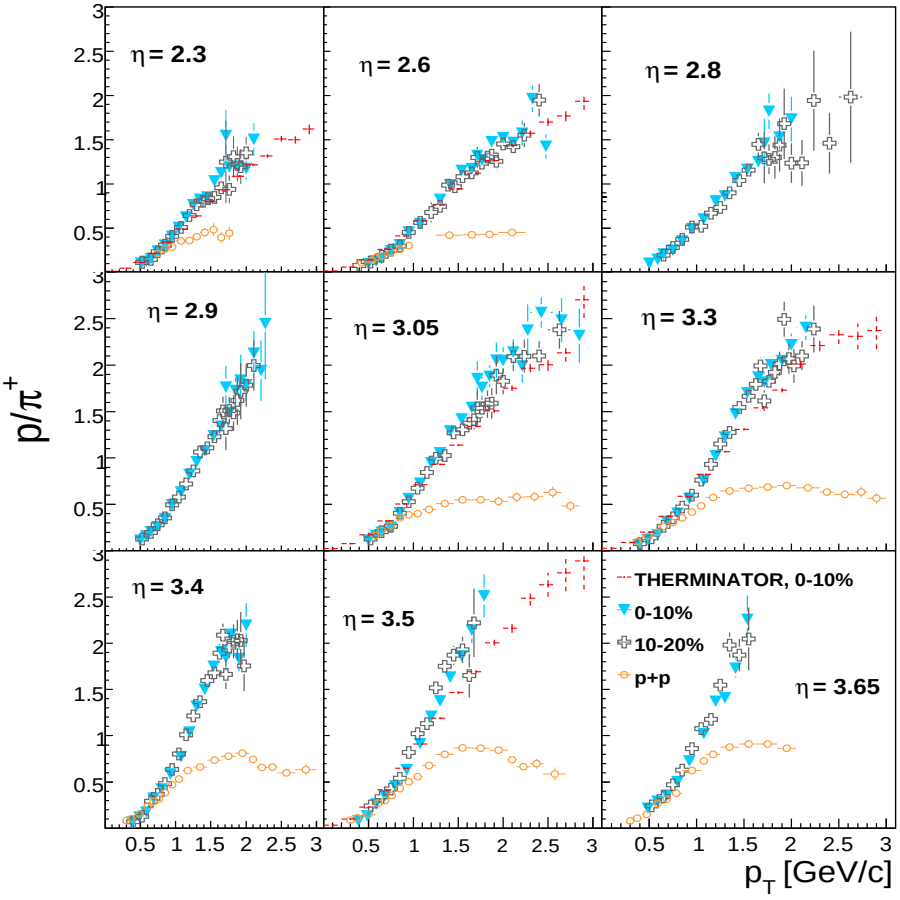

Figure 5.3: The $p/\pi^+(p_T)$ for Au+Au collisions $\sqrt{s_{NN}} = 200$ GeV for different values of pseudorapidity for two intervals of centrality: 0-10% (blue triangles) and 10-20 % (dark grey open crosses). The proton-to-pion ratios for p+p reactions $\sqrt{s} = 200$ GeV are shown (orange open circles). The data for the most central heavy ion reactions are compared with single-freezeout model calculations [66] (red crosses).

to measure particles produced in heavy ions and elementary collisions for pseudorapidity interval: $2 \leq \eta \leq 4$, we can follow the behaviour of p/π ratio with increasing baryo chemical potential, μ_B.

It has been already shown that the p/π^+ ratios at the intermediate p_T range can vary very strongly depending on both charge and pseudorapidity of indicated species, as well as on energy and size of colliding system. In Figs. 5.3, 5.4 and 5.5 the $p/\pi^+(p_T)$ ratio is displayed for Au+Au collisions at $\sqrt{s_{NN}} = 200$ GeV for 0-10% and 10-20%, 20-40%, 40-80% centrality, respectively, for different values of pseudorapidity indicated on the plots. Additionally, the proton-to-pion ratios for elementary reactions at the same colliding energy are presented (with exception for $\eta = 2.8$ and $\eta = 2.9$ due to lack of experimental data). For all centrality intervals, the striking observed property is consistency of heavy ions results with the outcome

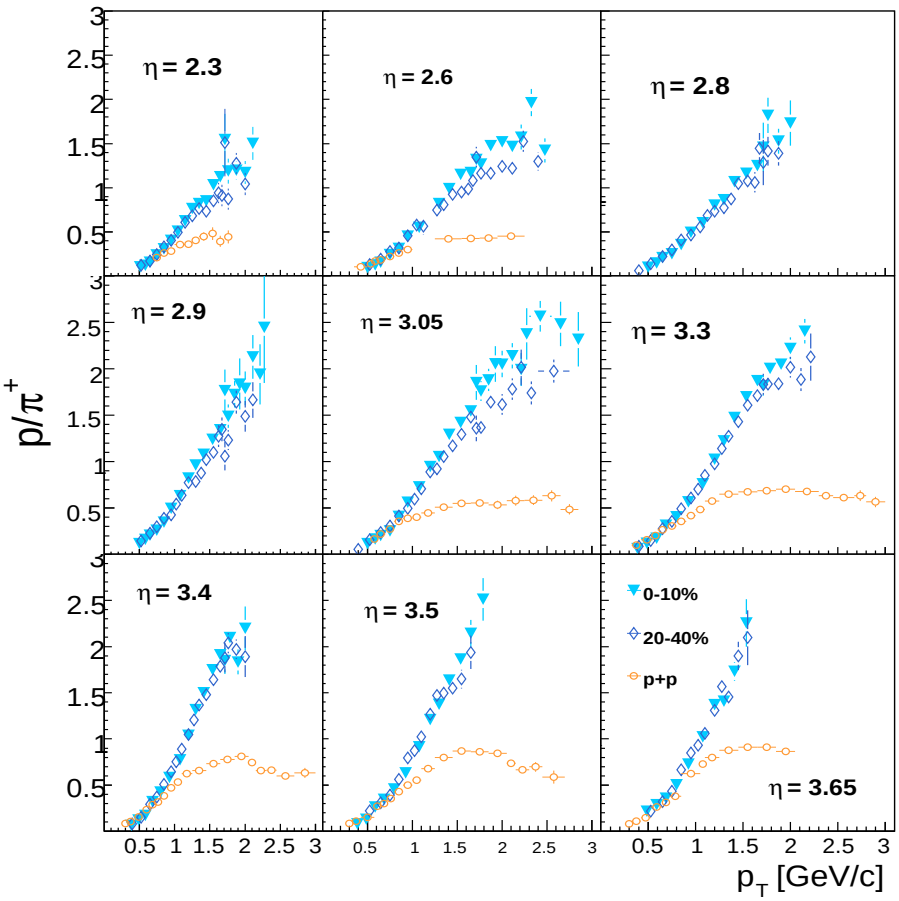

Figure 5.4: The same as Fig. 5.3, but for centrality intervals: 0-10% (blue triangles) and 20-40% (dark blue rhombuses).

for p+p system below $p_T < 1$ GeV/c. In the whole range of pseudorapidity, at low $p_T < 1$ GeV/c the ratios for both systems rise successively. At $p_T > 1$ GeV/c the results for p+p collisions starts noticeably to deviate from results for Au+Au reactions. Additionally, above $p_T \geq 1.3$ GeV/c the centrality dependence begins for Au+Au system. For heavy ions reactions the maximum of the ratio is equal ≈ 2.5 for the 0-10% centrality and for semi-peripheral collisions it is ≤ 2. The enhancement of p/π^+ ratio for central Au+Au reactions in respect to p+p indicates that the properties of the produced matter in Au+Au collisions are completely dissimilar than of that produced in p+p. The shift of the p/π^+ ratio peak to larger p_T as well as overall increase of ratio at intermediate p_T by factor of 4 in central Au+Au collisions as compared to p+p reactions give an evidence of existence of hot and dense medium created in heavy ions collisions [12, 53].

The Figs. 5.6, 5.7, 5.8 present the proton-to-pion ratios for different values of pseudorapidity for negatively charged particles. In general the $\bar{p}/\pi^-$ ratios

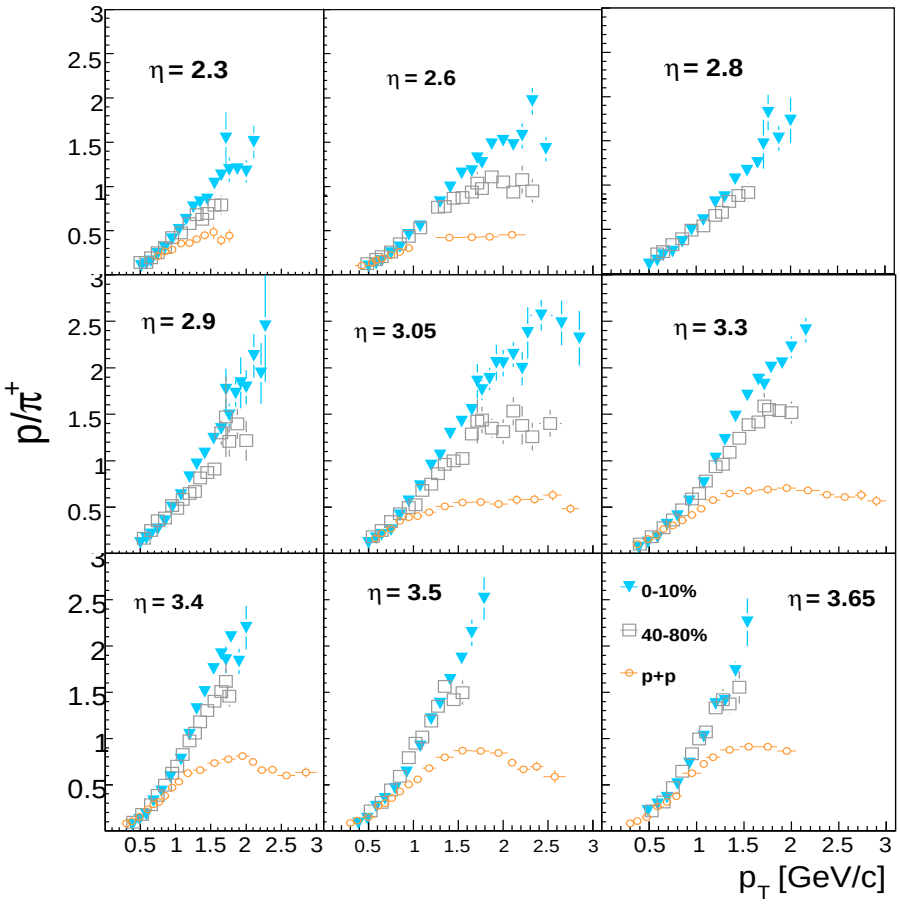

Figure 5.5: The same as Fig. 5.3, but for centrality intervals: 0-10% (blue triangles) and 40-80% (open green squares).

represent quite opposite trend than the ratios for positive hadrons. For Au+Au system for the most central reactions the highest value of $\bar{p}/\pi^-$ is equal 0.5 for $\eta = 2.3$ and $p_T \approx 1.7$ GeV/c and decreases towards more forward rapidities. However, the shape of the ratio and position of the peak is the same for all pseudorapidity bins. That tendency is also followed by semi-peripheral collisions, but the value of the ratios is a bit lower, especially for the 40-80% centrality interval. For Au+Au reactions the dependence on centrality collision begins at $p_T \approx 0.9$ GeV/c. Above that value a weak dependence of centrality is observed.

Fig. 5.9 shows the p/π^+ ratios as a function of p_T in the pseudorapidity range $2.6 \leq \eta \leq 3.8$ extracted from p+p reactions at $\sqrt{s} = 200$ GeV. The behaviour of $p/\pi^+(p_T)$ ratio for p+p system reveals the characteristic tendency, namely the increase of peak value with increasing pseudorapidity. A very clear difference is found as the pseudorapidity changes from $\eta = 2.6$ to $\eta = 3.8$. The value of ratio grows systematically with rising η from 0.4 at $\eta = 2.3$ reaching almost 1 at the

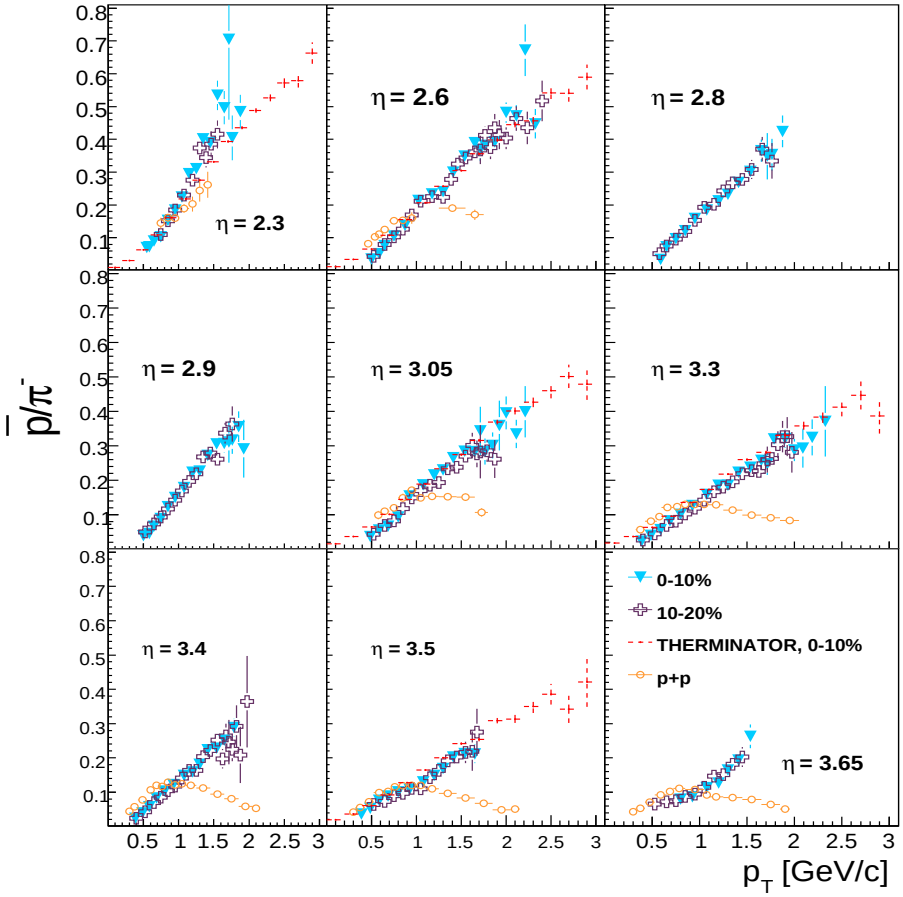

Figure 5.6: The $\bar{p}/\pi^-(p_T)$ for Au+Au collisions $\sqrt{s_{NN}} = 200$ GeV for different values of pseudorapidity for two intervals of centrality: 0-10% (blue triangles) and 10-20 % (dark grey open crosses). The proton-to-pion ratios for p+p reactions $\sqrt{s} = 200$ GeV are presented (orange open circles). The single-freezeout model predictions are shown for Au+Au system for 0-10 % centrality interval (red crosses).

most forward pseudorapidity interval, $\eta \approx 3.8$. That high value of p/π^+ ratio is indispensable related to the large proton yield at high p_T. If we look carefully, especially for $\eta = 2.6$, 3.1, 3.3 the proton-to-pion ratio at highest covered p_T seems to have a common value of 0.4 which is consistent with perturbative QCD predictions [12].

For negatively charged hadrons, the value of proton-to-pion ratio for elementary reactions in the measured pseudorapidity interval reaches maximum value of ~ 0.15 - Fig. 5.10. The p/π^+ ratio exceeds the $\bar{p}/\pi^-$ ratio by a factor of 5. The peak value is less than 0.3 for $\eta = 2.3$ and dropping to < 0.1 for $\eta = 3.8$. Moreover, the maximum of $\bar{p}/\pi^-$ ratio is shifted to the lower transverse momentum ($p_T \approx 1$ GeV/c) compared with the positive particles.

An interesting feature of $\bar{p}/\pi^-$ ratios is also revealed at low p_T. On the

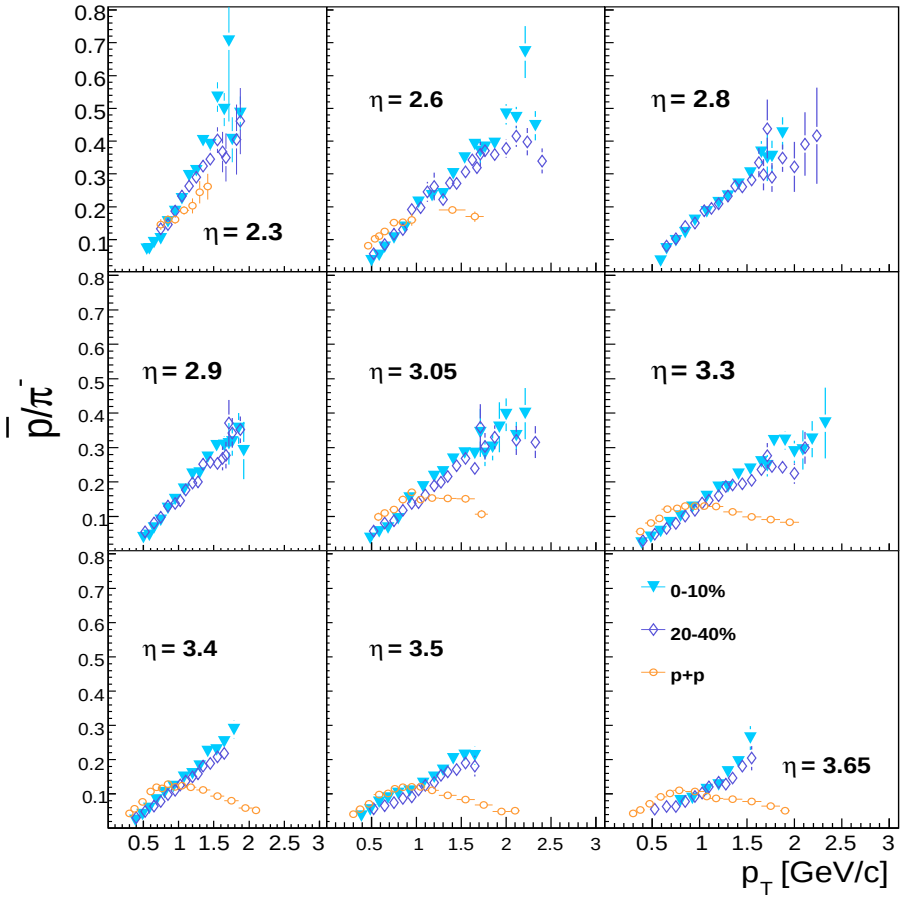

Figure 5.7: The same as Fig. 5.6, but for centrality intervals: 0-10% (blue triangles) and 20-40% (dark blue rhombuses).

right in Fig. 5.10 the comparison of $\bar{p}/\pi^-$ ratio in Au+Au and in p+p at $\sqrt{s_{NN}}$ = 200 GeV is shown. The data at the covered pseudorapidity interval, $2.6 \leq \eta \leq 3.8$, expose the same feature and the value of $\eta \approx 3.3$ has been selected for showing centrality dependence of the ratios. The $\bar{p}/\pi^-$ ratios increase with p_T for central and peripheral Au+Au collisions, while the ratio maximizes at ~ 0.9 GeV/c for p+p collisions. The ratios for Au+Au for different centrality classes and for p+p system cross each other at approximately $p_T \approx 0.9$ GeV/c. The higher value of $\bar{p}/\pi^-$ for p+p than for Au+Au collisions at the soft p_T region might be due to medium effects in heavy ions collisions at relativistic energies. The high level of challenge combined with the sensitivity of the models are associated with the proper description of data [12, 49, 50]. The theoretical basis is needed indicating the components which bring out the properties of particle production at low p_T.

The results presented in Figs. 5.3 and 5.6 for 0-10% central Au+Au collisions at $\sqrt{s_{NN}}$ = 200 GeV are compared with the non-boost-invariant single-

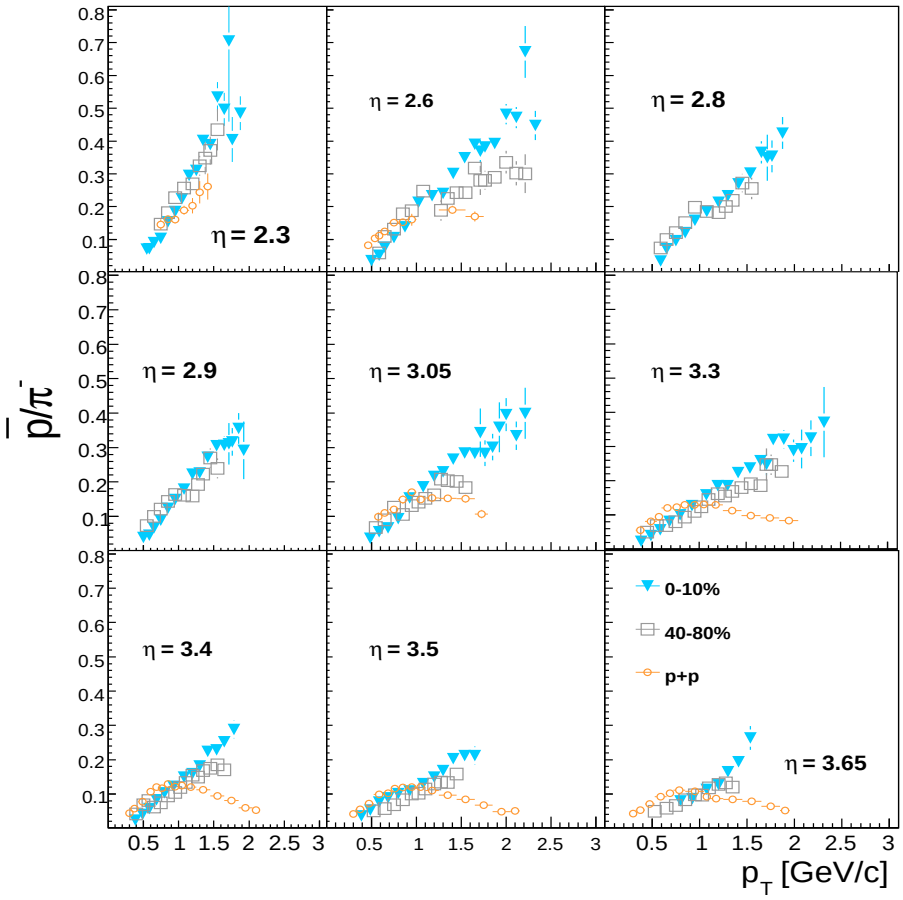

Figure 5.8: The same as Fig. 5.6, but for centrality intervals: 0-10% (blue triangles) and 40-80% (open green squares).

freezeout-model (with events generated with THERMINATOR) [50]. The model does not include the production of jet, so the calculations [66] are depicted up to $p_T = 3$ GeV/c. The single-freezeout model includes the hydrodynamical flow of produced particles together with the excited states. The statistical particle production contains the rapidity dependence. The model describes the experimental data surprisingly well in the whole range of pseudorapidity at transverse momentum $<$ 2 GeV/c for both charges of hadrons. For larger momenta theoretical predictions seems to deviate slightly from the BRAHMS data, particularly, for positive charged particles for $\eta > 3$. It is supposed to be due to the lack of jet production in the model. It seems that the data are in good agreement with the picture of evaporation of particles from the hypersurface of fireball, with the common local collective velocity field.

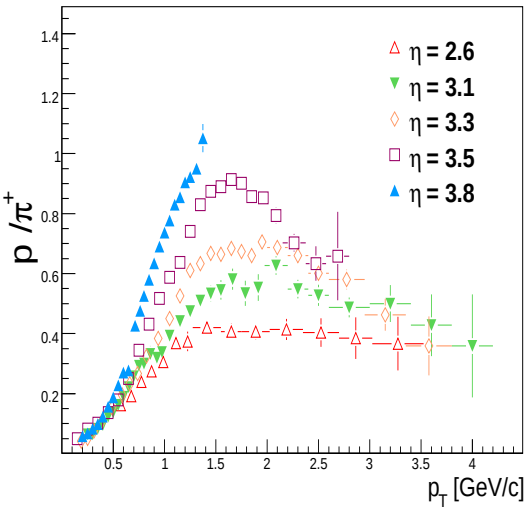

Figure 5.9: The proton-to-pion ratio for set of η bins in the range $2.6 \leq \eta \leq 3.8$ for p+p reactions at $\sqrt{s} = 200$ GeV.

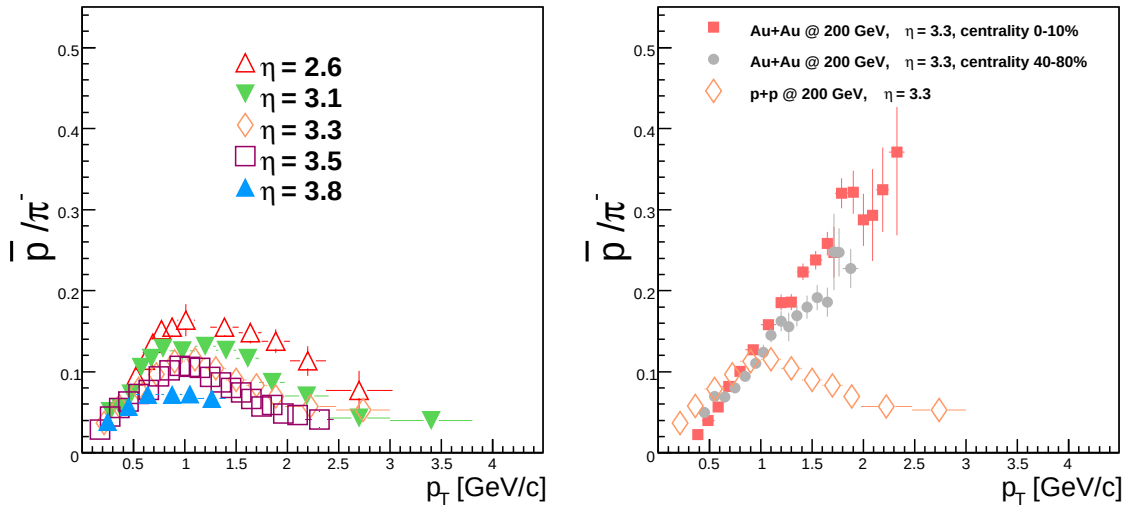

Figure 5.10: The $\bar{p}/\pi^-$ ratio vs. transverse momentum for $2.6 \leq \eta \leq 3.8$ for p+p collisions at $\sqrt{s} = 200$ GeV (left). On the right the results of ratio for p+p reactions are compared with the one for 0-10% and 40-80% central Au+Au collisions at $\sqrt{s_{NN}}$ = 200 GeV at the same value of pseudorapidity, $\eta = 3.3$.

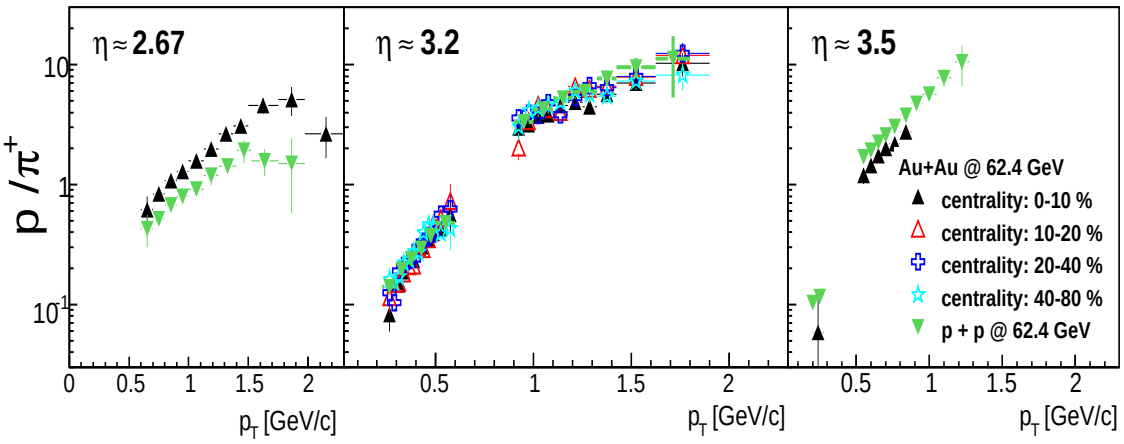

Figure 5.11: The p/π^+ ratio vs. transverse momentum for Au+Au and p+p collisions at $\sqrt{s_{NN}}$ = 62.4 GeV for $\eta \approx 2.67$, $\eta \approx 3.2$ and $\eta \approx 3.5$.

5.2 P/π^+ ratio in Au+Au collisions at $\sqrt{s_{NN}}$ = 62.4 GeV

The p/π^+ ratio for Au+Au collisions at $\sqrt{s_{NN}}$ = 62.4 GeV for $\eta \approx$ 2.67, 3.2, 3.5 is depicted in Fig. 5.11 (at $\eta \approx 3.2$ for Au+Au collisions at $\sqrt{s_{NN}}$ = 62.4 GeV $\mu_B \approx 250$ MeV, [79]). Additionally, the p+p results at the same energy and η bins are shown. At all pseudorapidities unexpected high value of 10 at p_T = 1.5 GeV/c of proton-to-pion ratio is observed [56]. There is remarkably little difference in the p/π^+ ratios for a very wide range of systems. This is in contrast to the trends at midrapidity and forward rapidity regimes for Au+Au at $\sqrt{s_{NN}}$ = 200 GeV where significant medium effect reflected in dependence of p/π^+ ratios on system size is observed [80]. However, the observed consistency between the results of p+p reactions and Au+Au system for all centrality bins for $\eta \approx 3.2$ is reckoned as the crossing point in pseudorapidity. These results indicate that the nuclear modification factor for protons and pions are equal in the observed p_T range at the same centrality bin, as shown in Eq. 5.1 (see the definition of R_{AA} in section: **1.2.2**):

$$\frac{R_{AA}^{\text{protons}}}{R_{AA}^{\text{pions}}} = \frac{\frac{d^2N^{A+A}_{\text{protons}}/dp_T dy}{d^2N^{p+p}_{\text{protons}}/dp_T dy}}{\frac{d^2N^{A+A}_{\text{pions}}/dp_T dy}{d^2N^{p+p}_{\text{pions}}/dp_T dy}} = \frac{\frac{d^2N^{A+A}_{\text{protons}}/dp_T dy}{d^2N^{A+A}_{\text{pions}}/dp_T dy}}{\frac{d^2N^{p+p}_{\text{protons}}/dp_T dy}{d^2N^{p+p}_{\text{pions}}/dp_T dy}} = 1. \tag{5.1}$$

The energy available from the rapidity loss of the beam dissipates and contributes through coalescence mechanism to increased proton yield at intermediate p_T. At very forward rapidities one can expect less power of nuclear stopping which might

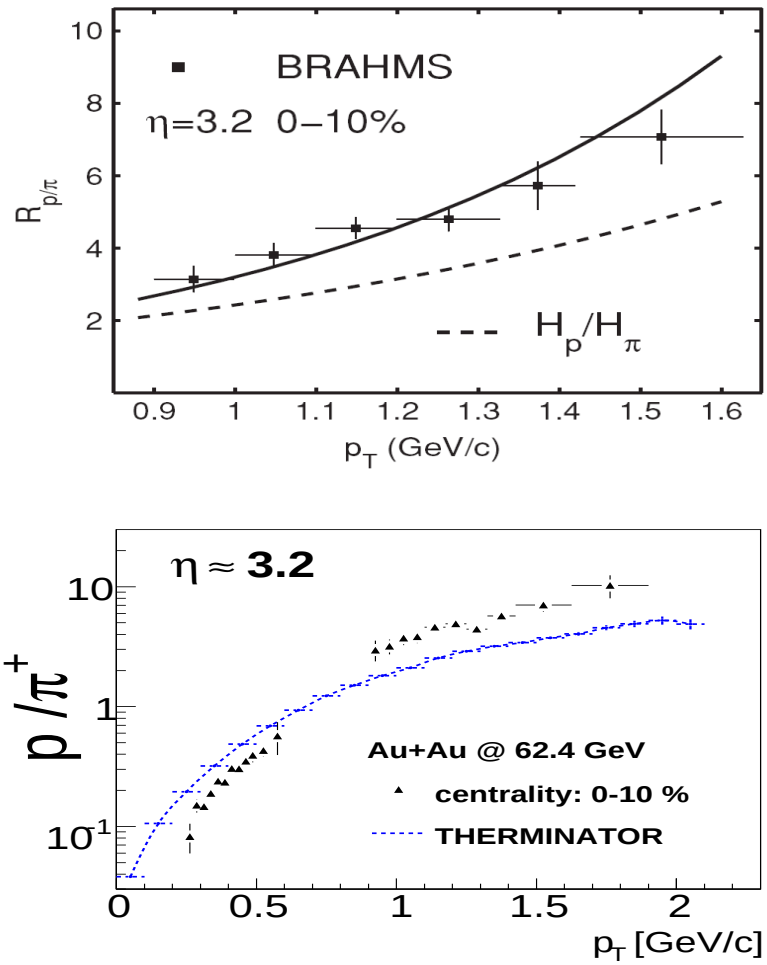

Figure 5.12: The results of recombination (upper plot) and single-freezeout (bottom plot) model calculations compared with BRAHMS results for the most central Au+Au collisions at $\sqrt{s_{NN}}$ = 62.4 GeV for $\eta \approx 3.2$. The upper picture has been taken from [49].

be observed as a result of enhancement of proton production to pion production that, particularly, is seen for elementary reaction. The higher value of p/π^+ for $\eta \approx 3.5$ for p+p collisions might acknowledge this argumentation. The crossing point was predicted by UrQMD [81], HIJING [82] and AMPT [17] calculations, but almost lower one unit of rapidity as experimental data indicate. It is a part of hadronization jigsaw implementing additional constraints on baryon number transport.

The p/π^+ results for Au+Au collisions at $\sqrt{s_{NN}}$ = 62.4 GeV has been tried to sort out by R. Hwa within recombination model [49]. In top panel of Fig. 5.12 the comparison of experimental results and theoretical approach are displayed. The BRAHMS data are quite well described. It might be worth introducing that BRAHMS outcome was firstly referred to the predictions included in [56]. That considerations indicate that the $p/\pi^+(p_T)$ should be below 4 with assumption that $\bar{p}/p$

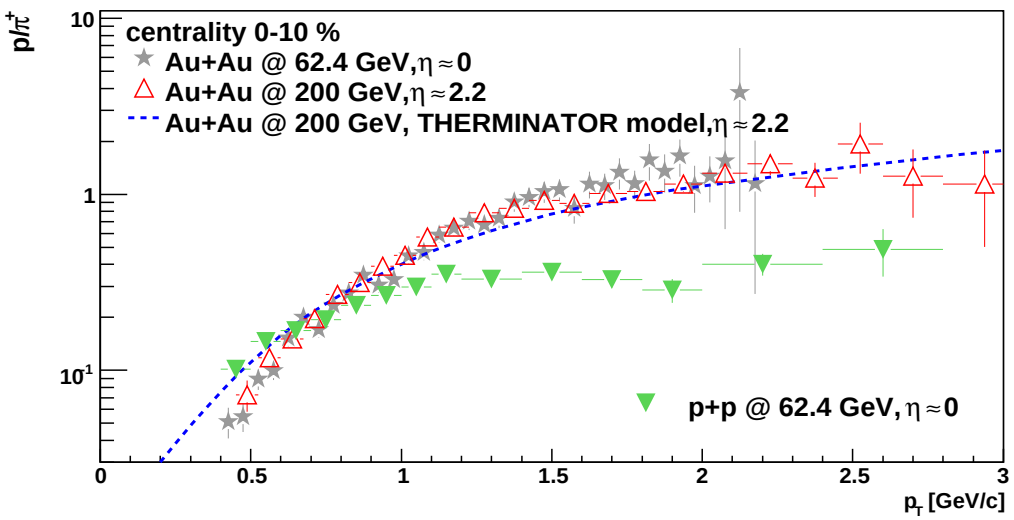

Figure 5.13: The p/π^+ ratio vs. transverse momentum for p+p and central (0-10%) Au+Au collisions at $\sqrt{s_{NN}} = 62.4$ GeV and 200 GeV for midrapidity and $\eta \approx 2.2$, respectively. The calculations of single-freezeout model for Au+Au reactions at $\sqrt{s_{NN}} = 200$ GeV and $\eta \approx 2.2$ are also shown.

ratio is equal 0.031. The most recent value of $\bar{p}/p$ ratio at $\eta = 3.2$ at $\sqrt{s_{NN}} = 62.4$ GeV is 0.023 [79]. To describe the data, in [49] it has been proposed the additional contribution that incorporates modification of parton distribution function in colliding nucleons. This modification is related to momentum degradation and quark regeneration which are argued to be significant for description of forward production of hadrons. On the other hand, this retrospect suggests that forward production of hadrons in heavy ions collisions at ultra-relativistic energies is not fully understood. R. Hwa has made an attempt to describe BRAHMS experimental data in the wide range of pseudorapidity within the recombination model. Capturing all important ingredients of R. Hwa's model the overall testing ground of recombination developments might be centrality dependent description of $p/\pi^+(p_T)$ ratio for Au+Au reactions at $\sqrt{s_{NN}} = 62.4$ GeV.

In Fig. 5.12 the data has been also compared with the computations of single-freezeout model. The single-freezeout model with well-defined collective expansion and successive evaporation of hadrons from the hypersurface of the fireball [50] describes the BRAHMS results only qualitatively in the whole covered range of transverse momentum.

5.3 Comparison of p/π^+ ratio in Au+Au collisions at $\sqrt{s_{NN}} = 62.4$ and 200 GeV

In Fig. 5.13 the results for Au+Au collisions for $\eta = 0.0$ at $\sqrt{s_{NN}} =$ 62.4 GeV and for Au+Au reactions for $\eta = 2.2$ at $\sqrt{s_{NN}} = 200$ GeV are displayed. The selection of pseudorapidity intervals, namely $\eta = 0.0$ for Au+Au @ 62.4 GeV and $\eta = 2.2$ for Au+Au @ 200 GeV allow to obtain overlap in $\bar{\text{p}}$/p, thus μ_B, for the observed systems at various energies. The value of $\bar{\text{p}}$/p is 0.45. It is indicated in Fig. 2.2 in section: **2.1** that such selection imposes that the data are measured at $\mu_B^{Au+Au@200GeV} = \mu_B^{Au+Au@62.4GeV} = 62$ MeV. Considerably lower value depicted by green triangles displays the p/π^+ ratio for p+p system at $\sqrt{s} = 200$ GeV. The p/π^+ ratios for heavy ion collisions are remarkably similar. The great overlap of proton-to-pion ratios for collate heavy ions collisions evidences that the baryon and meson production at the covered p_T interval is dominated by chemical properties. The strong medium effects are also seen throughout the observed enhancement of $p/\pi^+(p_T)$ for nucleus-nucleus systems with reference to the results for elementary interactions. The data infer possible scaling of baryon-to-meson ratio with baryo chemical potential for dense systems. In addition, the experimental results for $\eta \approx$ 2.2 are compared with the calculations of single-freezeout model. The good agreement of data with the theoretical description reflects that, at forward region, one can expect that the particle production follows rather scenario with collective expansion based on the Hubble-type flow.

Chapter 6

Conclusions

The main goal of this work was to obtain the experimental data on proton-to-pion ratio in Au+Au and p+p collisions at $\sqrt{s_{NN}} = 62.4$ GeV and $\sqrt{s_{NN}} = 200$ GeV as a function of transverse momentum in the wide range of pseudorapidity. The presented results are based on the data collected by BRAHMS experiment during 2004, 2005 and 2006 campaigns.

This thesis was primarily concerned with the analysis of particle production in forward regime utilizing BRAHMS experimental setup. The analysis consisted of local and global tracking algorithms as well as global detection procedures. The Data Summary Tape processing contained the track reconstruction, the global storage and detailed information of collision geometry. In addition, in the analysis the indispensable restrictions were applied e.g. fiducial cuts on dipole magnets, the triggers requirements, χ^2 cut. The determination of the collision vertex position, centrality and total charged particle multiplicity were obtained using global detectors (Multiplicity Array, Beam-Beam counters, Zero-Degree Calorimeters) measurements.

The BRAHMS particle identification (PID) was exploited to distinguish electrons, muons, pions, kaons and protons in the broad range of momentum: $0 < p < 40$ GeV/c. The procedure was followed separately for Time of Flight (H2) and Ring Imaging Cherenkov detector. The PID was performed by fitting the multi-Gaussian function into the squared invariant mass (m^2) distribution in small momentum bins. The $\pm$ 3 σ_{m^2} cuts were applied to separate particle species. The direct PID by RICH detector was obtained above pion, kaon and proton Cherenkov threshold $p \approx 2.2$, 9, 15 GeV/c, respectively. In the momentum range from 3.5-9 Gev/c, where the pion and kaon overlap in m^2 distribution, RICH detector veto signal was used to select kaons with momenta $p < 9$ GeV/c. Additionally, above the kaon threshold the proton identification was possible in this momentum range by association tracks

with veto signal in RICH detector. The RICH provided pion and proton separation up to $p \approx 40$ GeV/c.

The p/π ratio was performed by dividing proton and pion yields obtained separately at each η and p_T bins. Because the yields were procured from the real time measurements, the factors related to trigger normalization, tracking efficiency, centrality selection and acceptance canceled out in the ratio. Thus, the remaining corrections were the ones related to the particle-type, namely RICH PID correction, decays-in-flight and interactions with material budget correction.

The RICH efficiency was derived by comparing pion tracks registered in H2 detector having no associated rings in RICH detector with all tracks identified as pions in ToF detector. It was found that the pion efficiency equals 0 at the pion Cherenkov threshold ($p \approx 2.2$ GeV/c) and rapidly increases at larger momenta reaching 97% at $p \approx 4.0$ GeV/c. The RICH efficiency was estimated for pions assuming that the Cherenkov radiation depended on γ factor. The detailed analysis showed that the RICH efficiency depended on three effects: particle γ factor, geometrical effect, multiplicity of tracks reconstructed in T5 detector. The efficiency was used to correct veto proton yield for the pion and kaon contamination.

The correction for absorption and in-flight decays was determined by simulations of single pion and proton particles that were fed up as an input to a realistic GEANT model description of the BRAHMS experimental setup. In the analysis the correction was determined by momentum dependence.

Our results indicated the experimental observable, namely p/π ratio that would be sensitive to the hadronization mechanism and collectivity of the bulk medium created in the relativistic heavy ion reactions. I presented the data for p/π ratio in the wide pseudorapidity range as function of transverse momentum, collision centrality and beam rapidity. I reported the p/π^+ and $\bar{p}/\pi^-$ ratio as a function of p_T for the Au+Au and p+p systems at $\sqrt{s_{NN}} = 62.4$ GeV and 200 GeV. These data could be important for constraints on different model scenarios for baryon and meson production at low and intermediate p_T, in particular at forward rapidities.

For positively charged hadrons at the top RHIC energy of colliding nuclei, the proton and pion production seemed to be comparable at midrapidity at 2.5 GeV/c $< p_T <$ 4 GeV/c. It was shown that with increasing η at low p_T the ratios measured in Au+Au collisions at $\sqrt{s_{NN}} = 200$ GeV exhibited a rising trend for both charges of hadrons. The maximum of the p/π^+ ratio reached 3 in the forward regime for the most central collisions. The ratio of $\bar{p}/\pi^-$ equaled 0.5 for 0-10% Au+Au system at the same colliding energy. The centrality dependence of p/π^+ ratio suggested that the p/π^+ ratios at intermediate transverse momenta scaled with

the size of the created medium. For p/π^+ and $\bar{p}/\pi^-$ ratios for heavy ion reactions at $\sqrt{s_{NN}} = 200$ GeV the dependence of collision centrality was noticeable at larger transverse momenta, $p_T > 1$ GeV/c. For $p_T \leq 1$ GeV/c the overlap of data for all centrality intervals was conspicuous.

In the covered pseudorapidity interval, $2.3 < \eta < 3.65$, the value of p/π^+ ratio slightly increased going to more forward rapidities and a little shift of the peak value to larger transverse momenta was noted. For negative particles the inverse behaviour of the $\bar{p}/\pi^-$ ratio was observed - at $\eta \approx 2.3$ the $\bar{p}/\pi^-$ was 0.5 and dropping to 0.2 at the largest pseudorapidity bin, $\eta \approx 3.65$.

For elementary collisions at $\sqrt{s} = 200$ GeV the p/π^+ ratio increased with increasing pseudorapidity at intermediate transverse momenta. For larger p_T the value of ratios reached a common value of 0.4 that was in accordance with pQCD predictions. Compared to positive charged hadrons the shift of the peak of $\bar{p}/\pi^-$ ratio to the lower p_T was noticeable, as well as the fact that the maximum of the ratio was smaller by a factor of 5. Moreover, the inverse tendency prevailed - the value of $\bar{p}/\pi^-$ ratio was < 0.2 and decreased for larger pseudorapidity.

The striking property of $\bar{p}/\pi^-$ in p+p collisions at $\sqrt{s} = 200$ GeV was the difference in the shape of the ratio compared to heavy ion results. What was exceptional a larger value of the ratios for elementary reactions at the same energy at low transverse momentum, $p < 0.9$ GeV/c, was observed. That behaviour of experimental data clearly suggested the existence of medium effects in heavy ions interactions.

The comparison of central (0-10%) Au+Au collisions at $\sqrt{s_{NN}} = 62.4$ GeV at midrapidity and at $\sqrt{s_{NN}} = 200$ GeV for $\eta \approx 2.2$ showed remarkable consistency of the ratios. It implied that the chemical bulk medium properties had tangible influence on the particle production. The trend was quite different for results in nucleon-nucleon reactions (p+p) at $\sqrt{s_{NN}} = 62.4$ GeV at $\eta \approx 0$ where the maximum value of the ratio equaled 0.4 and it was much lower than for nucleus-nucleus collisions.

For Au+Au and p+p reactions at $\sqrt{s_{NN}} = 62.4$ GeV at forward pseudorapidity region, the large value of $p/\pi^+(p_T)$ ratio was noted. At this energy and pseudorapidity interval the weak centrality dependence of p/π^+ ratio was observed. Furthermore, the proton-to-pion ratio of nucleus-nucleus data was consistent with results obtained for elementary p+p reactions. The latest calculations of R. Hwa's model indicated that the recombination of the quarks was a possible scenario to explain the Au+Au collisions at $\eta \approx 3.2$ at $\sqrt{s_{NN}} = 62.4$ GeV. The consistency with the results for elementary reactions indicated that we observed the crossing

point of ratio in pseudorapidity. The lack of centrality dependence of the ratios in nucleus-nucleus collisions at $\eta \approx 3.2$ implied the equal nuclear modification factor for protons and pions (R_{AA}) at the covered p_T interval if compared at the same centrality bin. This indication was closely related to the baryon transport process and energy dissipation in nuclear reaction. The location of the crossing point would provide strong constraints on the theoretical descriptions of baryon number transport and associate energy dissipation in relativistic nuclear reactions.

Chapter 7

Appendix 1

It is indispensable to introduce a set of variables used to describe particles produced in relativistic nucleus-nucleus reactions.

1. **Rapidity**

   (a) particle rapidity is defined:

   $$y \equiv \frac{1}{2}\ln\frac{E_0 + p_z}{E_0 - p_z} \tag{7.1}$$

   where:
   E_0 - particle energy, p_z - particle momentum in the longitudinal direction

   invariant mass of a free particle: $E_0^2 - \vec{p}^2 = m^2$

   transverse mass of a free particle: $m_\perp^2 = m^2 + p_\perp^2$

   Feynman's variable:

   $$x = \frac{p_z}{p_z^{max}} \approx \frac{E_0 + p_z}{(E_0 + p_z)_{max}} \approx \frac{2p_z}{\sqrt{s}} \tag{7.2}$$

   (b) Lorentz transformation:

   $$y' = y - \tanh\beta \tag{7.3}$$

   (c) relations:

   $$y = \ln\frac{E_0 + p_z}{m_\perp} \tag{7.4}$$

$$E_0 = m_\perp \mathrm{cosh} y; \quad p_z = m_\perp \mathrm{sinh} y \tag{7.5}$$

$$y_{max} = \ln \frac{\sqrt{s}}{m} \tag{7.6}$$

$$x \approx \frac{2 m_\perp \mathrm{sh} y}{\sqrt{s}}. \tag{7.7}$$

2. **Pseudorapidity**

   (a) particle pseudorapidity is defined:

$$\eta \equiv -\ln \mathrm{tan} \frac{\theta}{2} \tag{7.8}$$

   where:

   θ - angle between momentum of particle, $\vec{p}$, and the beam direction

   (b) relations:

   when $p \gg m$ and $\theta \gg \frac{1}{\gamma}$:

$$y = \frac{1}{2} \ln \frac{E_0 + p_z}{E_0 - p_z} \approx \frac{1}{2} \ln \frac{\cos^2 \frac{\theta}{2} + \frac{m^2}{4p^2}}{\sin^2 \frac{\theta}{2} + \frac{m^2}{4p^2}} \approx -\ln \mathrm{tan} \frac{\theta}{2} \equiv \eta. \tag{7.9}$$

3. **Cross section**

   (a) inclusive cross section:

$$\frac{d^3\sigma}{dp^3} = \frac{1}{\pi} \frac{d^3\sigma}{dp_\perp^2 dp_z} = \frac{2}{\sqrt{s}\pi} \frac{d^3\sigma}{dp_\perp^2 dx} = \frac{1}{\pi E_0} \frac{d^3\sigma}{dp_\perp^2 dy} \tag{7.10}$$

   (b) invariant inclusive cross section:

$$E \frac{d^3\sigma}{dp^3} = \frac{2E}{\pi\sqrt{s}} \frac{d^3\sigma}{dp_\perp^2 dx} = \frac{1}{\pi} \frac{d^3\sigma}{dp_\perp^2 dy} \tag{7.11}$$

$$E \frac{d^3N}{dp^3} = \int f(x,p,t) d\sigma = \frac{d}{2\pi^3} \int \frac{p d\sigma(x)}{exp[(pu(x) - \mu(x))/T(x)] \pm 1} \tag{7.12}$$

4. **Particle identification procedure - counting the m^2 parameter**

The successive steps of estimating m^2 value using in $m^2 - p$ maps:

(a) Time of Flight measurements

m^2 can be calculated from momentum, p, and ToF(β) measurements. The resolution, $\sigma(m^2)$, depends on particle momentum. Particle identification is performed applying momentum dependent cuts on m^2 - p maps.

$$p = \gamma\beta m \;\rightarrow\; p^2 = \gamma^2\beta^2 m^2 \rightarrow\; p^2 = \left(\frac{1}{\sqrt{1-\beta^2}}\right)^2 \beta^2 m^2 \tag{7.13}$$

$$m^2 = p^2\left(\frac{1}{\beta^2} - 1\right) \tag{7.14}$$

(b) Ring Imaging Cherenkov detector measurements

In case of RICH we measure the particle momentum, p, and ring radius, R. As for H2 data the resolution depends on the momentum. PID is performed in the same way.

$$\cos\theta = \frac{1}{n\beta} \tag{7.15}$$

$$m^2 = p^2\left(n^2\cos^2\theta - 1\right) \tag{7.16}$$

$$\theta = \text{arctg}\left(\frac{R}{L}\right) \tag{7.17}$$

where:
$\beta = \frac{v}{c}$ - the speed of the particle refering to the speed of the light, θ - the angle of emission Cherenkov radiation, R - ring radius, $L = 150$ cm - the focal length of the RICH detector mirror, n - refraction index.

Chapter 8

Appendix 2

The lists of settings with itemized runs for particular species and energies of the colliding systems are introduced in details:

period: **run 04**	**setting: 2A1723**
specie: **Au + Au**	**runs:** 10209, 10210, 10211, 10212, 10213, 10216
energy: $\sqrt{s_{NN}}$ = **200 GeV**	**setting: 2B1723**
	runs: 10201, 10202, 10206
	setting: 2A2442
	runs: 10220, 10221, 10222, 10234, 10235
	setting: 2B2442
	runs: 10192, 10193, 10198, 10200
	setting: 2A3450
	runs: 10240, 10244, 10245, 10249, 10250
	setting: 2B3450
	runs: 10190, 10191
	setting: 3A1723
	runs: 10496, 10497, 10498, 10501, 10524, 10525, 10535, 10536, 10537, 10538, 10549
	setting: 3B1723
	runs: 10493, 10494

period: **run 04** *specie:* **Au + Au** *energy:* $\sqrt{s_{NN}}$ **= 200 GeV**	**setting: 3A3450**
	runs: 10036, 10037, 10038, 10039, 10040
	setting: 3B3450
	runs: 10047, 10049, 10050, 10051, 10060
	setting: 4A861
	runs: 10438, 10443, 10444, 10445
	setting: 4B861
	runs: 10302, 10305
	setting: 4A1219
	runs: 11206, 11207, 11212, 11213, 11214
	setting: 4B1219
	runs: 11193, 11201, 11204, 11205
	setting: 4A1723
	runs: 10275, 10276, 10277, 10281, 10282, 10283, 10284, 10285, 10425, 10426, 10427, 10428, 10434, 10435, 10436, 10437
	setting: 4B1723
	runs: 10289, 10294, 10295, 10296, 10299, 10300, 10301, 10350, 10351, 10352, 10358, 10484, 10485, 10486, 10487, 10488
	setting: 4B2442
	runs: 10310, 10311, 10312, 10313, 10314, 10315
	setting: 4A3450
	runs: 10254, 10255, 10256, 10257, 10260, 10262, 10263, 10264, 10273, 10359, 10360, 10361, 10362, 10366, 10367, 10368, 10369, 10372, 10374, 10375, 10376, 10377, 10378, 10379, 10382, 10383, 10384, 10385, 10386, 10392, 10394, 10395, 10396, 10398, 10400, 10405, 10406, 10407, 10414, 10415, 10416, 10421, 10422, 10423, 10424
	setting: 4B3450
	runs: 10316, 10318, 10319, 10320, 10321, 10326, 10327, 10328, 10329, 10330, 10331, 10332, 10336, 10337, 10338, 10339, 10342, 10343, 10344, 10345, 10346, 10347, 10446, 10447, 10448, 10449, 10453, 10454, 10455, 10456, 10457, 10458, 10459, 10460, 10464, 10465, 10469, 10470, 10471, 10472, 10476, 10477, 10478, 10479, 10483

period: **run 04** *specie:* **Au + Au** *energy:* $\sqrt{s_{NN}}$ = **200 GeV**	**setting: 6A1219**
	runs: 10003, 10004, 10005, 10011, 10012, 10014, 10017
	setting: 6B1219
	runs: 9981, 9982, 9988
	setting: 6A1723
	runs: 10018, 10019, 10022, 10023, 10024
	setting: 6B1723
	runs: 9961, 9975, 9976, 9977, 9978, 9979
	setting: 6A861
	runs: 9996, 9997, 9998, 9999, 10002
	setting: 6B861
	runs: 9989, 9990, 9995
	setting: 8A608
	runs: 9890, 9891, 9892, 9893, 9894, 9895, 9898
	setting: 8B608
	runs: 9929, 9930, 9931, 9934, 9935
	setting: 8B861
	runs: 9936, 9940, 9941, 9944, 9945
	setting: 8A1219
	runs: 9918, 9921, 9922, 9923, 9927, 9928
	setting: 8B1219
	runs: 9946, 9947, 9948, 9949, 9952, 9953 9954
	setting: 8A1723
	runs: 10573, 10577, 10578, 10579, 10580, 10581, 10584, 10585, 10586, 10587, 10588, 10591, 10592, 10593, 10594, 10596, 10597, 10598, 10599, 10600, 10603, 10604, 10605, 10606, 10613, 10614, 10615, 10616, 10620, 10621, 10622, 10623, 10626, 10627, 10628, 10632, 10633, 10634, 10635, 10636, 10640, 10645, 10646, 10647, 10648, 10652, 10653, 10654
	setting: 8B1723
	runs: 10167, 10168, 10169, 10170, 10183, 10184, 10190, 10191, 10192, 10193, 10198, 10199, 10200, 10201, 10202, 10205, 10206, 10209, 10210, 10211, 10212, 10213, 10216, 10219, 10220, 10221, 10222, 10234, 10235, 10236, 10240, 10241, 10242, 10243, 10244, 10245, 10249, 10250, 10251, 10254, 10255,

period: **run 04** *specie:* **Au + Au** *energy:* $\sqrt{s_{NN}}$ **= 200 GeV**	**setting: 8B1723**
	runs: 10256, 10257, 10260, 10262, 10263, 10264
	setting: 8A3450
	runs: 10816, 10817, 10818, 10819, 10822, 10823, 10824, 10832, 10834, 10835, 10841, 10842, 10843, 10844, 10845, 10846, 10850, 10854, 10855, 10856, 10857, 10870, 10871, 10874, 10875, 10876, 10877, 10896, 10897, 10898, 10899, 10903, 10904, 11002, 11003, 11004, 11007, 11008, 11015, 11016, 11021, 11022, 11023, 11028, 11029, 11030, 11035, 11036, 11037, 11039, 11058, 11059, 11061, 11062, 11064, 11065, 11066, 11072, 11077, 11078, 11079, 11081, 11083, 11087, 11088, 11089, 11090, 11095, 11096, 11103, 11104, 11105, 11107, 11115, 11116, 11117, 11129, 11130
	setting: 8B3450
	runs: 10726, 10727, 10728, 10729, 10731, 10732, 10742, 10743, 10744, 10745, 10746, 10749, 10750, 10751, 10753, 10754, 10755, 10756, 10757, 10758, 10759, 10760, 10765, 10766, 10780, 10781, 10782, 10784, 10785, 10787, 10788, 10794, 10795, 10796, 10797, 10799, 10800, 10801, 10802, 10807, 10808, 10809, 10812, 10813, 10814, 10815, 11138, 11139, 11140, 11147, 11153, 11154, 11222, 11223, 11224, 11225, 11226, 11227, 11232, 11233, 11234, 11236, 11237, 11238, 11244, 11248, 11251, 11257, 11265, 11268, 11269, 11282, 11283, 11288, 11290, 11291
	setting: 10A430
	runs: 9762, 9763, 9768, 9769, 9771, 9772, 10962
	setting: 10B430
	runs: 9822, 9825, 9826, 9829, 9830, 9857, 9858, 9860
	setting: 10A608
	runs: 9773, 9774, 9778, 10940, 10941
	setting: 10B608
	runs: 9831, 9832, 9833, 9836, 9837, 9838, 9839
	setting: 10A861
	runs: 9780, 9781, 9782, 9783, 9784, 10911,

period: **run 04** *specie:* **Au + Au** *energy:* $\sqrt{s_{NN}}$ **= 200 GeV**	**setting: 10A861**
	runs: 10912, 10913, 10916, 10928, 10929, 10930,
	10933, 10935, 10936
	setting: 10B861
	runs: 9840, 9841, 9842, 9844, 9845, 9846
	setting: 10A1219
	runs: 9790, 9813, 9814, 9815, 9816, 9817, 9818,
	9820, 9821
	setting: 10B1219
	runs: 9847, 9850, 9851, 9852, 9853
	setting: 12A430
	runs: 9751, 9754, 9755, 9757, 9758, 9759, 9760,
	9761
	setting: 12B430
	runs: 9751, 9754, 9755, 9757, 9758, 9759, 9760,
	9761
	setting: 12A861
	runs: 9735, 9736, 9737, 9738, 9739, 9742, 9743,
	9744, 9745, 9746, 9747, 9748
	setting: 12B861
	runs: 9709, 9712, 9716, 9717, 9718, 9719, 9720,
	9721, 9725, 9732

period: **run 04** *specie:* **Au + Au** *energy:* $\sqrt{s_{NN}}$ **= 62.4 GeV**	**setting: 3A1723**
	runs: 11311, 11312, 11323, 11324, 11325, 11326, 11327, 11329, 11330, 11331, 11332, 11333, 11337
	setting: 3B1723
	runs: 11338, 11344, 11345, 11346, 11349, 11351, 11352, 11353, 11354, 11355, 11359, 11360, 11361, 11365, 11367, 11369
	setting: 4A608
	runs: 11476, 11480, 11485, 11490, 11491, 11492, 11501
	setting: 4B608
	runs: 11450, 11455, 11459, 11460, 11466, 11467, 11473, 11474
	setting: 6A861
	runs: 11375, 11376, 11377, 11378, 11379, 11383, 11386, 11387, 11388, 11389, 11390, 11396, 11397, 11399, 11410, 11411, 11414, 11415, 11419, 11420
	setting: 6B861
	runs: 11422, 11423, 11424, 11426, 11434, 11437, 11438, 11439, 11441, 11442, 11443, 11447, 11449
	setting: 8A861
	runs: 11547, 11549, 11554, 11565, 11566, 11567, 11568, 11570, 11575
	setting: 8B861
	runs: 11299, 11300, 11301, 11302, 11303, 11305
	setting: 8A1219
	runs: 11509, 11510, 11511, 11513, 11520, 11521 11523, 11532, 11540, 11541
	setting: 8B1219
	runs: 11544, 11545, 11546

period: **run 05** *specie:* **p + p** *energy:* $\sqrt{s_{NN}}$ **= 200 GeV**	**setting: 4A1723**
	runs: 14071, 14074, 14075, 14076, 14077, 14078, 14110, 14114, 14115, 14116
	setting: 4B1723
	runs: 14179, 14181, 14182, 14186, 14187, 14188, 14189, 14190
	setting: 4A3450
	runs: 14889, 14890, 14891, 14892, 14893, 14894, 14895, 14896, 14897, 14898, 14901, 14902, 14903, 14904, 14905, 14906, 14907, 14908, 14909, 14910, 14911, 14917, 14918, 14919, 14920, 14921, 14922, 14923, 14924, 14925, 14926, 14927, 14928, 14929, 14930, 14931, 14932, 14933, 14934, 14935, 14939, 14944, 14945, 14946, 14948, 14950, 14954, 14955, 14956, 14957, 14958, 14960, 14961, 14962, 14963, 14971, 14972, 14975, 14976, 14977, 14978, 14979, 14980, 14981, 14990, 14991, 14992, 14993, 14994, 14995, 14996, 14997, 14998, 15004, 15005, 15006, 15007, 15008, 15009, 15012, 15013, 15014, 15015, 15016, 15020, 15021, 15022, 15023, 15026, 15027, 15030, 15031, 15032, 15033, 15034, 15036, 15037, 15038, 15039, 15040, 15043, 15044, 15045, 15046, 15047, 15048, 15051, 15052, 15053, 15054, 15055, 15056, 15057, 15060, 15061, 15062, 15063, 15064, 15065, 15066, 15067, 15068, 15069, 15111, 15112, 15116, 15117, 15118, 15119, 15120, 15121, 15122, 15123, 15124
	setting: 4B3450
	runs: 15545, 15546, 15547, 15548, 15549, 15550, 15551, 15552, 15553, 15554, 15555, 15556, 15557, 15558, 15559, 15560, 15561, 15565, 15566, 15567, 15568, 15569, 15570, 15571, 15572, 15573, 15575, 15576, 15579, 15580, 15581, 15582, 15583, 15584, 15585, 15586, 15587, 15588, 15589, 15590, 15591, 15592, 15593, 15594, 15595, 15596, 15597, 15598, 15599, 15600, 15601
	setting: 4A430
	runs: 14199

period: **run 05** *specie:* **p + p** *energy:* $\sqrt{s_{NN}}$ **= 200 GeV**	**setting: 4B430**
	runs: 14195, 14196
	setting: 4A861
	runs: 14118, 14120, 14123
	setting: 4B861
	runs: 14152, 14153, 14154, 14155, 14158, 14159, 14160
	setting: 4A1219
	runs: 14200, 14201, 14202 13245
	setting: 4B1219
	runs: 14162, 14163, 14167, 14168, 14175, 14176
	setting: 4A2442
	runs: 15145, 15146, 15147, 15148, 15149, 15150, 15151, 15152, 15153, 15154, 15155, 15156, 15157
	setting: 4B2442
	runs: 15170, 15171, 15172, 15174, 15175
	setting: 2A3450
	runs: 15699, 15700, 15701, 15702, 15703, 15704, 15705, 15706, 15707, 15713, 15714, 15715, 15717, 15718, 15719, 15720, 15721, 15722, 15723, 15729, 15731, 15734, 15735, 15736, 15737, 15738, 15739, 15740, 15741, 15742, 15743, 15744, 15745, 15746, 15748, 15749, 15750, 15751, 15752, 15753, 15760, 15761, 15762, 15763, 15764, 15765, 15767, 15768, 15769, 15770, 15773, 15774, 15775, 15776, 15777, 15778, 15779, 15780, 15781, 15783, 15784, 15785, 15786, 15794, 15797, 15798, 15800, 15801
	setting: 2B3450
	runs: 14555, 14556, 14558, 14559, 14560, 14561, 14562, 14563, 14564, 14565, 14566, 14567, 14568, 14569, 14570, 14571, 14604, 14605, 14606, 14607, 14608, 14609, 14610, 14611, 14612, 14613, 14614, 14615, 14616, 14617, 14618, 14619, 14620, 14621, 14622, 14623, 14624, 14625, 14669, 14670, 14671, 14672, 14678, 14679, 14680, 14681, 14682, 14683, 14684, 14685, 14686, 14687, 14688, 14689, 14690,

period: **run 05** *specie:* **p + p** *energy:* $\sqrt{s_{NN}}$ **= 200 GeV**	**setting: 2B3450**
	runs: 14691, 14692, 14693, 14695, 14698, 14699, 14700, 14701, 14702, 14703, 14704, 14705, 14706, 14707, 14708, 14709, 14710, 14711, 14712, 14713, 14714, 14715, 14716, 14717, 14718, 14719, 14720, 14721, 14722, 14723, 14725, 14726, 14727, 14728, 14729, 14731, 14732, 14733, 14734, 14737, 14738, 14739, 14743, 14744, 14745, 14750, 14752, 14754, 14755, 14756, 14757, 14758, 14759, 14762, 14763, 14764, 14765, 14766, 14767, 14768, 14769, 14770, 14774, 14775, 14776, 14777, 14778, 14779, 14780
	setting: 2A861
	runs: 15220, 15221, 15222, 15223, 15224, 15225, 15226, 15227, 15228, 15231, 15235
	setting: 2B861
	runs: 15200, 15201, 15204, 15205, 15206, 15207, 15208, 15209, 15210, 15211, 15212, 15213, 15214, 15215, 15216
	setting: 2A1723
	runs: 15240, 15241, 15242, 15243, 15244, 15245, 15246, 15247, 15248
	setting: 2B1723
	runs: 15179, 15180, 15181, 15185, 15188, 15189, 15190
	setting: 8A608
	runs: 14208, 14209, 14212, 14213, 14214, 14215
	setting: 8B608
	runs: 14342, 14344, 14345, 14346, 14347, 14348
	setting: 8A1219
	runs: 14216, 14224, 14228, 14229, 14233
	setting: 8B1219
	runs: 14351, 14353, 14354
	setting: 8A1723
	runs: 14330, 14331, 14332, 14335, 14336, 14337, 14338
	setting: 8B1723
	runs: 14355, 14359, 14364, 14365, 14368

period: **run 05**	**setting: 8A2442**
specie: **p + p**	**runs:** 14303, 14306, 14307, 14328
energy: $\sqrt{s_{NN}}$ **= 200 GeV**	**setting: 8B2442**
	runs: 14373, 14379, 14384, 14386, 14389, 14390

period: **run 06** *specie:* **p + p** *energy:* $\sqrt{s_{NN}}$ **= 62.4 GeV**	**setting: 2A1723**
	runs: 16213, 16214, 16215, 16216, 16217, 16218, 16219, 16220, 16221, 16222, 16229, 16231, 16232, 16233, 16234, 16235, 16236, 16237, 16238, 16239, 16240, 16241, 16242, 16243, 16244, 16245, 16246, 16247, 16248, 16261, 16262, 16263, 16264, 16265, 16266, 16267, 16268, 16269, 16271, 16272, 16273, 16274, 16277, 16278, 16279, 16280, 16281, 16282, 16283
	setting: 2B1723
	runs: 16249, 16250, 16251, 16252, 16255, 16256, 16257, 16258, 16259, 16260
	setting: 3A1723
	runs: 16048, 16050, 16051, 16052, 16053, 16054, 16055, 16056, 16057, 16058, 16059, 16062, 16064, 16065, 16066, 16067, 16068, 16069, 16070, 16071, 16072, 16073, 16074, 16075, 16076, 16078, 16079, 16080, 16081, 16082, 16084, 16085, 16086, 16087, 16090, 16091, 16092, 16093, 16094, 16097, 16098, 16100, 16101
	setting: 3B7123
	runs: 16109, 16111, 16112, 16113, 16114, 16115, 16116, 16118, 16119, 16124, 16125, 16126, 16127, 16128, 16129, 16130, 16131, 16132, 16133, 16134, 16135, 16138, 16139, 16140, 16141, 16142, 16143, 16144, 16145, 16146, 16147, 16148, 16149, 16150, 16151
	setting: 4A608
	runs: 16030, 16031, 16034, 16035, 16036, 16037, 16040, 16041, 16042, 16043 13245
	setting: 4B608
	runs: 15988, 15989, 15990, 15991, 16006, 16007, 16008, 16009, 16017, 16018, 16019, 16020, 16021, 16022, 16025, 16026, 16027

period: **run 06** *specie:* **p + p** *energy:* $\sqrt{s_{NN}}$ = **62.4 GeV**	**setting: 6A861**
	runs: 16185, 16186, 16187, 16192, 16193, 16195, 16196, 16197, 16198, 16199, 16200, 16201, 16202, 16203, 16204, 16205, 16206, 16207, 16208, 16209, 16210, 16211, 16212
	setting: 6B861
	16166, 16167, 16168, 16169, 16170, 16171, 16175, 16176, 16177, 16178, 16179, 16180, 16181, 16182

The specification of used triggers during all measurements is listed below:

period: **run 04** *specie:* **Au + Au** *energy:* $\sqrt{s_{NN}}$ = **200 GeV**	**Trigger**	**Description**
	1	Beam-Beam Counters
	2	(left and right array hit ≥ 2) Forward Spectrometer trigger: ZDC, TRFS, H1 and H2 hodoscopes
	3	Midrapidity Spectrometer trigger: ZDC, TRMRS, Time of Flight Wall
	4	ZDC: RHIC clock
	5	ZDC vertex: RHIC clock
	6	Front Forward Spectrometer: ZDC, TRFS, H1 hodoscope

period: **run 04** *specie:* **Au + Au** *energy:* $\sqrt{s_{NN}}$ = **62.4 GeV**	**Trigger**	**Description**
	1	Beam-Beam Counters
	2	(left and right array hit ≥ 1) Front Forward Spectrometer trigger: TRFS, BB counters, H1 hodoscope, RHIC clock
	3	Midrapidity Spectrometer trigger: ZDC, TRMRS, Time of Flight Wall
	4	ZDC: RHIC clock
	5	ZDC vertex: RHIC clock
	6	Front Forward Spectrometer: ZDC, TRFS, H1 hodoscope, RHIC clock

period: **run 05** *specie:* **p + p** *energy:* $\sqrt{s_{NN}}$ **= 200 GeV**	**Trigger**	**Description**
	1	Beam-Beam Counters
	2	(overlapping signals in left and right tubes) Forward Spectrometer trigger: TRFS, RHIC clock, H1 and H2 hodoscopes
	3	Midrapidity Spectrometer trigger: TRMRS, RHIC clock, Time of Flight Wall
	4	CC: RHIC clock
	5	ZDC vertex: RHIC clock
	6	Front Forward Spectrometer: ZDC, TRFS, H1 hodoscope

period: **run 06** *specie:* **p + p** *energy:* $\sqrt{s_{NN}}$ **= 62.4 GeV**	**Trigger**	**Description**
	1	Beam-Beam Counters
	2	(overlapping signals in left and right tubes) Forward Spectrometer trigger: RHIC clock, TRFS, H1 and H2 hodoscopes
	3	Midrapidity Spectrometer trigger: TRMRS, RHIC clock, Time of Flight Wall
	4	CC: RHIC clock
	5	ZDC vertex: RHIC clock
	6	Front Forward Spectrometer: ZDC, TRFS, H1 hodoscope

References

[1] E.V. Shuryak, Phys. Lett. B **78**, 150 (1978).
E.V. Shuryak, Phys. Rep. **61**, 71 (1980).

[2] B. A. Freedman, L. D. McLerran, Phys. Rev. D **16**, 1196 (1977).
J. Kapusta, Nucl. Phys. B **148**, 461 (1979).

[3] STAR Collab., Nucl. Phys. A **757**, 102 (2005).

[4] PHENIX Collab., Nucl. Phys. A **757**, 184-283 (2005).

[5] PHOBOS Collab., Nucl. Phys. A **757**, 28 (2005).

[6] BRAHMS Collab., Nucl. Phys. A **757**, 1-27 (2005).

[7] M. Gyulassy, L. McLerran, Nucl. Phys. A **750**, 30-63 (2005).

[8] R. A. Lacey, A. Taranenko, The 2nd Edition of International Workshop - Correlations and Fluctuations in Relativistic Nuclear Collisions, Galileo Galilei Institute, Florence, Italy, July 7-9, 2006.

[9] E. J. Kim (BRAHMS Collab.), Nucl. Phys. A **774**, 493-496 (2006).

[10] S. Voloshin, Y. Zhang, Z. Phys. C **70**, 665 (1996).

[11] M. Gyulassy, T. Matsui, Phys. Rev. D **29**, 3, (1984).

[12] T. Hirano, Y. Nara, Nucl. Phys. A **743**, 305 (2004). T. Hirano, Y. Nara, Phys. Rev. C **69**, 034908 (2004).

[13] STAR Collab., Phys. Rev. Lett. **99**, 112301 (2007).

[14] PHOBOS Collab., Phys. Rev. C **72**, 051901, (2005).

[15] X.-N. Wang, Phys. Lett. B **579**, 299-308, (2004).

[16] S. Sanders (BRAHMS Collab.), Hadron Physics and Properties of High Baryon Density Matter, Xi'an, China, November 22-25, 2006.

[17] Z. W. Lin, C. M. Ko, S. Pal, Phys. Rev. Lett. **89**, 152301 (2002).

[18] BRAHMS Collab., Phys. Rev. Lett. **93**, 242303 (2004).

[19] BRAHMS Collab., Phys. Lett. B **677**, 267-271 (2009).

[20] BRAHMS Collab., Phys. Rev. Lett. **93**, 102301 (2004).

[21] F. Videbæk, O. Hansen, Phys. Rev. C **52**, 2684 (1995).
C. Blume (NA49 Collab.), J. Phys. G **34**, 951-954 (2007).

[22] J. D. Bjorken, Phys. Rev. D **27**, 140-151 (1983).

[23] BRAHMS Collab., Phys. Rev. Lett. **91**, 072305 (2003).

[24] BRAHMS Collab., Phys. Lett. B **650**, 219 (2007).
R. Karabowicz, Quark Matter 2005, Budapest, Hungary, August 4-9, 2005, BRAHMS parallel talk.

[25] V. Greco, C.M. Ko, P. Levai, Phys. Rev. Lett. **90** 022302 (2003).

[26] J. W. Cronin, H. J. Frisch, M. J. Shochet, Phys. Rev. D **19**, 764 (1979).

[27] L. McLerran, J. Phys. Conf. Ser. **5**, 127-147 (2005) and references therein.

[28] D. Kharzeev, Y. Kovchegov, K. Tuchin, Phys. Rev. D **68**, 094013 (2003).

[29] A. Capella, E. G. Ferreiro, A. B. Kaidalov, D. Sousa, arXiv:hep-ph/0403081.

[30] STAR Collab., Phys. Lett. B **637**, 161 (2008).

[31] BRAHMS Collab., Phys. Rev. Lett. **101**, 042001 (2008).

[32] BRAHMS Collab., Phys. Rev. Lett. **98**, 252001 (2007).

[33] S. Albino, B. A. Kniehl, G. Kramer, Nucl. Phys. B **803**, 42-104 (2008).

[34] J. Benecke, T. T. Chou, C. N. Yang, E. Yen, Phys. Rev. **188**, 2159 (1969).

[35] N. Katryńska (BRAHMS Collab.), Diffraction 2008 AIP Conference Proceedings **1105**, (2009).

[36] NA49 Collab., Phys. Rev. Lett. **82**, 2471 (1999).

[37] Z. Fodor, S. Katz, J. High Energy Phys., 050, (2004) and references therein.

[38] M. A. Halasz, A. D. Jackson, R. E. Shrock, M. A. Stephanov, J. J. M. Verbaarschot, Phys. Rev. D **58**, 096007 (1998).

[39] J. Kapusta, "Finite-temperature field theory", (1993).

[40] M. Bellac, "Thermal Field Theory", (2000).

[41] J. Cleymans, H. Satz, Z. Phys. C **57**, 135 (1993).

[42] D. Rischke, arXiv:nucl-th/0305030.

[43] http://www.bnl.gov/rhic, June 2009.

[44] D. Kharzeev, M. Nardi, Phys. Lett. B **507**, 121 (2001).

[45] R. Debbe, Quark Matter 2008, Jaipur, India, February 3-10, 2008, BRAHMS plenary talk.

[46] J. Cleymans, H. Oeschler, K. Redlich, S. Wheaton, Phys. Rev. C **73**, 034905 (2006).

[47] P. Braun-Munzinger, Nucl. Phys. A **681**, 119c-123c (2001).

[48] J. Cleymans, K. Redlich, Phys. Rev. Lett. **81**, 5284 (1998).

[49] R. Hwa, Li-Lin Zhu, Phys. Rev. C **78**, 024907 (2008).

[50] W. Broniowski, B. Biedroń, Phys. Rev. C **75**, 054905 (2007).

[51] R. Hwa, C. B. Yang, Phys. Rev. C **67**, 034902 (2003).

[52] R. Hwa, C. B. Yang, Phys. Rev. C **70**, 024904 (2004).

[53] R. Hwa, C. B. Yang, Phys. Rev. C **70**, 024905 (2004).

[54] R. Hwa, C. B. Yang, Phys. Rev. C **73**, 044913 (2006).

[55] R. Hwa, C. B. Yang, Phys. Rev. C **73**, 064904 (2006).

[56] R. Hwa, C. B. Yang, Phys. Rev. C **76**, 014901 (2007).

[57] R. Hwa, J. Phys. G: Nucl. Part. Phys. **35**, 104017 (2008).

[58] N. Katryńska, P. Staszel (BRAHMS Collab.), poster presentation at Quark Matter 2008, Jaipur, India, 4-10 February 2008, arXiv:nucl-ex/0806.1162.

[59] A. Białas, M. Bleszyński, W. Czyż, Nucl. Phys. B **111**, 461-476, (1976).

[60] T. Hirano, arXiv:nucl-th/0601006.

[61] Sollfrank, et al., Phys. Rev. C **55**, 392 (1997) and references therein.

[62] D. Srivastava, et al., Phys. Rev. C **56**, 1064 (1997) and references therein.

[63] F. Cooper, G. Frye, Phys. Rev. D **10**, 186 (1974).

[64] J. Cleymans, K. Redlich, Phys. Rev. C **60**, 054908 (1999).

[65] W. Broniowski, B. Biedroń, Phys. Rev. Lett. **87**, 272302 (2001).

[66] A. Marcinek, Master's thesis, Jagiellonian University, (2009).

[67] P. Braun-Munzinger, D. Magestro, K. Redlich, J. Stachel, Phys. Lett. B **518**, 41 (2001).
F. Beccatini, M. Gaździcki, A. Keranen, J. Manninen, R. Stock, Phys. Rev. C **69**, 024905 (2004).

[68] E. Schnedermann, J. Sollfrank, U. Heinz, Phys.Rev. C **48**, 2462 (1993).
U. Heinz, Nucl. Phys. A **661**, 140 (1999).

[69] BRAHMS Collab., Nucl. Instr. Meth. A **499**, 437 (2003).

[70] BRAHMS analysis note: Track Reconstruction Efficiency in FS Tracking Detectors, http://www4.rcf.bnl.gov/brahms/WWW/, November 2001.

[71] BRAHMS analysis note: Efficiency Correction for Forward Spectrometer Tracks, http://www4.rcf.bnl.gov/brahms/WWW/, October 2009.

[72] R. Debbe, C. E. Jorgensen, J. Olness, Z. Yin, Nucl. Instr. Meth. A **570**, 216-222 (2007).

[73] C. Adler, A. Denisov, E. Garcia, M. Murray, H. Strobele, S. White, Nucl. Instr. Meth. A **499**, 433 (2002).

[74] P. Staszel, postdoctoral thesis, in preparation.

[75] http://wwwasd.web.cern.ch/wwwasd/geant, June 2009.

[76] BRAHMS Collab., Phys. Rev. C **72**, 014908 (2005) and references therein.

[77] PHENIX Collab., Phys. Rev. Lett. **91**, 172301 (2003).

[78] T. Hirano, Y. Nara, Phys. Rev C **69**, 034908 (2004).

[79] I. Arsene, (BRAHMS Collab.), oral presentation at Quark Matter 2008, Jaipur, India, 4-10 February 2008.

[80] BRAHMS Collab, submitted Phys. Lett. B, arXiv:nucl-ex/09112586.

[81] http://th.physik.uni-frankfurt.de/ũrqmd, July 2009.

[82] http://www-nsdth.lbl.gov/x̃nwang/hijing, July 2009.